THE TCS PROGRAM

Translation, Confinement, & Sustainment of FRCs

FINAL REPORT
(7/00 – 1/03)

Redmond Plasma Physics Laboratory
Aerospace & Energetics Research Program
University of Washington
Seattle, Washington 98195

May, 2003

THE TCS PROGRAM
(Translation, Confinement, & Sustainment of FRCs)

FINAL REPORT
(7/00 – 1/03)

Contract No. DE-FG03-96ER54376

By
Redmond Plasma Physics Laboratory
Aerospace & Energetics Research Program
University of Washington
Seattle, Washington 98195

Principal Investigator: Alan L. Hoffman

May, 2003

TABLE OF CONTENTS

I. INTRODUCTION

The TCS (Translation, Confinement, & Sustainment) program was begun on 7 August, 1996 to renew basic studies of the Field Reversed Configuration (FRC). Original funding of $4,018,000 was provided for 4 years until 6 July, 2000. The program made use of the old LSX (Large s Experiment) device[1], which was constructed at STI during the period from 1986 to 1990, but only operated for one year due to a DOE decision at the time to focus exclusively on the tokamak configuration. LSX was transferred to the university of Washington in 1992 and modified (LSX/mod) to perform Tokamak Refueling by Accelerated Plasmoids (TRAP) experiments.[2] The TRAP program was funded from 7 August, 1992 until 6 August, 1996, but utilized for an additional year while TCS was being constructed.

During the first funding period TCS was completed and initial experiments were begun. A large multi-megawatt power supply was built by Los Alamos National Laboratory (LANL) for use with a Rotating Magnetic Field (RMF) system, and LANL has been a participant in our experimental program. A smaller prototype facility, called the Star Thrust Experiment (STX) was also built and operated in this period, partly with NASA funding, before TCS came on-line. A final report for this first funding period was submitted in September of 2000.

The 2-½ year funding period covered in this report began on July 7, 2000 and ended on January 6, 2003. A total of $4,029,000 was provided. This provided for a staffing level of 1.5 FTE faculty, 3.0 FTE scientists, 1.3 FTE engineer, and 3.0 FTE technicians, along with approximately 6 graduate research assistants, two of whom have received their PhDs and are now working with us as Post Docs. A great deal of progress was made in understanding the use of RMF to both form and sustain FRCs. FRCs can now be considered steady-state, mainly closed field line configurations, which was a long-time, but never accomplished, goal of the Reversed Field Mirror program, and has important implications for eventual reactor applications. The principal result of the experimental program was the formation of quasi steady-state (as long as RMF power was available) FRCs with densities in the $1\text{-}3\text{x}10^{19}$ m^{-3} range. However, the plasma temperature was limited to sub-100 eV, except transitorily during start-up, by the rapid accumulation of impurities. This is not surprising since TSC was only designed to initially demonstrate RMF flux build-up and was not provided with either fueling capabilities or modern vacuum conditioning technology. The machine employed a multi-section quartz vacuum vessel with greased "O"-ring seals. Extrapolations to higher temperatures are very promising if radiation levels can be lowered, and a proposal to completely modify TCS with wall conditioning and high vacuum technology was accepted for continued operation.

The FRC confinement geometry is extremely attractive for a fusion reactor since the plasma contains little or no toroidal field, is extremely high beta, and is supported by simple solenoidal magnets.[3] Although it is a type of Compact Toroid with no structure threading its center, its physics is markedly different from that of the other class of CT (with a toroidal field), the spheromak.[4] Once small FRCs were formed in the laboratory

and observed to be grossly stable, the principal concern became the continued stability as the FRCs became larger and less kinetic in nature. This kinetic nature was characterized by the parameter s, equal to the number of ion gyro-radii between the field null and the separatrix. Before LSX most experiments had been limited to $s \leq 2$, the value above which some theoretical calculations predicted stabilizing kinetic effects to lose their effectiveness. LSX was built to explore FRC confinement at larger s values and, in its one year of operation, pushed the observed stability boundary up to about $s = 4$. This was accomplished by making LSX the largest FRC facility in existence, with a quartz plasma tube diameter of 80-cm and length of 6.25-m (5 sections of 1.25-m long 80-cm diameter quartz tubes joined by plastic rings containing 'O-rings').

It is extremely difficult to produce high beta toroidal plasmas since the plasma pressure must be increased at the same rate as the magnetic field pressure. This requires prodigious input powers, especially at high densities where impurity barriers can prevent rapid temperature increases. FRCs have thus been formed in Field Reversed Theta Pinch (FRTP) machines where a rapid reversal of the axial field produces plasma breakdown and trapping of some fraction of the initial reverse bias flux. Connection of this flux with some of the forward external flux produces the FRC. Rapid heating is provided by a radial implosion, some ohmic dissipation, and an axial implosion. However, this axial implosion must be extremely uniform and symmetric to result in successful formation. LSX was built with all the formation controls found necessary in the previous TRX program[5] (a 20-cm diameter device) to operate at high bias field levels. It was found on TRX that flux trapping could be effective even at low applied azimuthal electric fields, which were utilized on LSX to keep the total voltages (and thus costs) manageable. However, the lack of radial implosion heating exacerbated the axial implosion uniformity requirements. Nevertheless, formation techniques were developed in the one year of operation to permit the above mentioned $s = 4$ FRCs to be produced.

The original LSX design (5-m long by 90-cm diameter axial field coils) was changed to perform the TRAP experiments. All formation sizes were scaled down by a factor of two, resulting in a 2.5-m long by 40-cm tube diameter FRTP formation section plus a 0.5-m long upstream section with puff-fill valves. Another 2-m was used for an inductive accelerator consisting of a 27-cm diameter plasma tube and four 50-cm long three-turn pulsed coils which were fired as the FRC passed through them, thus providing a higher field in the rear and accelerating the FRC. This new design is called LSX/mod. Additional transport and interaction chambers were constructed for the TRAP experiments, but have since been discarded.

When DOE policy changed to once again sponsor alternate confinement concepts, the TCS program was proposed. Rather than reconstitute the original LSX, it was decided to adopt a different technique to try and extend FRC physics. LSX could form FRCs with about 10 mWb of poloidal flux. This could probably have been doubled with extreme effort, but would still fall short by two orders of magnitude of the several Wb needed for a reactor. Since the s value only scales as the two-thirds power of the flux (at a given temperature), the FRTP technique is extremely limited even for advancing the present base of physics knowledge with respect to stability. It has been a feature of FRC

theoretical efforts that the theoretical s stability boundary has risen in conjunction with the newest experimental results, and thus alternate flux build-up techniques with longer range capabilities are desirable. In addition, the extremely violent FRTP formation technique was a very poor method for testing stability of a quiescent FRC.

In order to develop a technique that would not be technologically limited in achievable flux level, we decided to utilize the Rotating Magnetic Field (RMF) current drive methodology which has been pioneered by Ian Jones at Flinders University.[6] Not only can an RMF build up an FRC, but it can sustain it in steady state, providing the added incentive of steady state operation for both eventual reactor applications and better stability investigations. However, the requirement of providing initial high formation power levels has not changed, and it was decided to use LSX/mod to form normal high density ($n \sim 10^{21}$ m^{-3}), high field ($B_e \sim 0.5$ T) FRCs, and then translate and expand them into a larger, lower field confinement region (utilizing the old 80-cm diameter LSX plasma tube sections with quasi steady-state coils). The resultant sub 10^{20} m^{-3} densities are both more suitable for RMF current drive and are in a more steady-state reactor relevant regime. RMF drive could then be used to both increase the flux and sustain it. However, no provision was made in the original design for refueling and maintaining the FRC particle inventory since flux build-up and sustainment was felt to be a challenging enough goal for the initial experiments. As it turned out, the RMF acts similar to the induced electric field from a transformer, and radial particle diffusion is reversed, resulting in long particle confinement times. The initial s values are much less than in LSX, but with the possibility that they could be greatly increased if the flux build-up technique proved highly successful.

The reversing of outward particle diffusion is a key feature of RMF physics. In contrast to tokamaks where current drive occurs along toroidal field lines, current drive in FRCs must occur across poloidal field lines. In the absence of an azimuthal electric field (necessary for steady-state with constant poloidal flux) the radial diffusion velocity is given by $v_r = -(\eta_\perp j_\theta + F_\theta/ne)/B_z$. j_θ is negative and if the RMF drive force F_θ is strong enough to counter the ohmic dissipation, it also stops radial diffusion. Of course, since the cross-field resistivity is anomalous, higher drive forces are required than for parallel current drive, but the ohmic power which can be supplied to the plasma may also be sufficient for reaching ignition conditions without any additional auxiliary heating.

The rotating magnetic field is produced by using two pairs of Helmholtz-like coils to generate horizontal and vertical fields transverse to the FRC axis. These coils are energized by RF power supplies phased 90° apart, which produce a rotating transverse field. The two-legged power supply been built for this project by Los Alamos National Laboratory uses 6 large Machlet triodes for each leg.[7] These nominally 45 kV (we limit them to 30 kV), 250 Amp tubes were originally procured for the SYLLAC circular theta-pinch project and would be prohibitively expensive to procure new. They can be reconditioned if necessary at a cost of $10,000 each. The tube based power supplies can each supply ~1 kA pulses at 30 kV (about 10 MW taking into account 40% on-times) for several msec. The RMF antennas are used as part of a parallel tank circuit, so that up to

10 kA sinusoidal antenna currents are achievable under no-load conditions. This results in over 5 mT rotating fields, which was the original specification for the system.

TCS was initially operated without any RMF drive to investigate the formation, translation, and capture of hot, low density FRC. These experiments were successful, which is testament to the ruggedness of the FRC (at least at low s), but the densities were still too high for RMF drive to be effective, and impurity generation from contact of the super-Alfvénic FRC with the TCS confinement chamber resulted in quartz ablation. The new modifications currently underway are being designed to also alleviate this problem. Due to the high resultant impurity levels in the translated FRCs, no significant attempts were made during the time covered by this report to sustain these FRCs with RMF.

An analytic and numerical effort was also continued to model the unique features of RMF current drive as it applies to a standard elongated FRC inside a flux conserver. The combination of our experimental measurements and code calculations has greatly increased our understanding of the RMF current drive process. The RMF will only penetrate far enough into the plasma (seldom much beyond the field null) to drive the current necessary to reverse the external field. Current on the inner field lines is sustained by an overall inward flow set up by the reversal of the normally outward diffusive flow on the external field lines, resulting in low measured and calculated separatrix densities. Particle conservation requires an overall swirling flow from inner back to outer flux lines, or the influx and ionization of neutrals, which are key features of the process. For efficient current drive the FRM frequency must be chosen appropriate to the expected conditions. The RMF drive process appears to work as theoretically predicted, and its utility will depend on the magnitude of cross field resistivity and overall energy confinement. If the anomalous resistivity is too high, the amount of RMF power required to maintain the FRC current or flux will be prohibitive. The present experimental results have shed some light on the plasma resistivity scaling, and methods to improve it. Energy confinement is presently limited by radiation, so we do not yet have data relating to the basic transport related thermal confinement. This will be a focus of operation with the redone vacuum chamber.

Papers describing the basic theory of RMF current drive as applied to prolate FRCs inside a flux conserver were first published in 2000. The first was analytic[8] and the second numerical[9]. The basic design of the TCS facility and initial operational results were published in a Fusion Technology paper dedicated to the device description.[10]. An initial paper on some details of the RMF flux build up was then published in 2002.[11] Several other papers are currently being submitted for publication based on results contained in this final report.

A TCS Web site exists for viewing information about operating sessions, particular pulses, diagnostics, etc. An annotated page from this Web-site is attached at the end of this section. This page is from the Web-site 'Summary' section, with times and typical shot ranges indicated. Clicking on each summary topic opens up a more detailed description of that topic, along with typical shot numbers to view. Information for all individual shots are contained in the 'Pulse List'.

This final report is organized into a analysis of RMF current drive (Section 2), a facility description (Section 3), a description of the RMF start-up experiments with improved operation, diagnostics, and analysis over what was reported in Ref. 11 (Section 4), and some interesting results from the translation and capture of LSX/mod formed FRCs, without RMF attempted flux build-up (Section 5). The final section outlines our plans and design for extensive modifications to TCS to provide clean, bankable vacuum chamber commensurate with steady state operation (section 6). Detailed descriptions of the diagnostics employed are given in Appendix A.

This page is intended to provide: a brief summary of what has currently been done on TCS and a list of some interesting pulses.

- Pulse list for experiments with doubled flux rings IV: 258kHz (Dec 02 – 9719-9762)

II. ANALYSIS OF RMF CURRENT DRIVE

2.1 Basic Scaling

In its simplest manifestation an RMF has the single mode representation in vacuum of

$$\mathbf{B} = B_\omega \cos(\omega t - \theta)\mathbf{e}_r + B_\omega \sin(\omega t - \theta)\mathbf{e}_\theta = (B_\omega \mathbf{e}_r - iB_\omega \mathbf{e}_\theta)e^{i(\omega t - \theta)}. \qquad [2.1]$$

Actual antennas will produce more than a single mode, as will the presence of plasma, but this simple vacuum description is adequate when the antennas are sufficiently removed from the plasma column. The second complex form is useful for analysis, including both amplitude and phase information.

RMF current drive works by driving electrons into near synchronous rotation with the rotating field, much in the same manner as for an induction motor. This requires that the RMF frequency lie between the ion cyclotron frequency $\omega_{ci} = eB_\omega/m_i$ and the electron cyclotron frequency $\omega_{ce} = eB_\omega/m_e$ with respect to the RMF magnitude. This can be expressed as $\omega_{ci} < \omega << \omega_{ce}$. When ω approaches ω_{ci} the ions will also be driven, but this lower limit on ω can be relaxed somewhat since it is actually only the B_r component that contributes to current drive, and for cases with partial RMF penetration $|B_r| << B_\omega$. In any case, the RMF force on the electrons is transferred to the bulk fluid through electron-ion collisions, and some external means must be available to stop the ions from eventually spinning up and canceling the current drive. In all our experiments the ion spin-up was limited to $\omega_i < 10^5$ s^{-1}, probably due to viscosity or electric field shorting, and we will ignore it in this analysis. (An effective RMF frequency of ω-ω_i would be more appropriate in scaling calculations, but ω_i is not routinely measured.) For electron drive to be effective the electron-ion effective collision frequency $\nu_\perp$ must be much less than ω_{ce}, and a characteristic ratio $\gamma = \omega_{ce}/\nu_\perp$ has been widely used in the literature. A second ratio which is often used is the ratio of radius to simple skin depth, $\lambda = r_s/\delta$ where $\delta = (2\eta_{//}/\mu_o\omega)^{1/2}$ and we assume plasma resistivity $\eta_{//} = \eta_\perp = m_e\nu_\perp/n_e e^2$.

All our analytical and numerical work so far has been done assuming a uniform resistivity $\eta_\perp$ across the plasma column of infinite axial extent. This is sufficient to understand the basic features of RMF current drive, such as applied torque and absorbed power, but it cannot reproduce certain details of the RMF penetration profiles. There is experimental evidence, especially for low ζ (defined in Eq. 2.2 below) that the resistivity is much higher at the plasma edge where current drive is taking place, then in the bulk of the FRC. This might be expected since the electron drift velocity is highest there, and the density lowest, which has always led to high anomalous resistivities in FRCs and theta pinches. We are working on models to include such effects, but all the work covered in this report is based on the uniform resistivity model. Only the simplest estimates, not included in this section, have been made to try and account for finite antenna and FRC lengths.

RMF penetration is made possible by the Hall effect preventing large axial screening currents from being generated within the small depth δ, but can also be expressed as an effective skin depth being $\delta^* = (2\eta_\perp/\mu_o\varpi)^{1/2}$, where $\varpi = \omega - \omega_e$. It is essential that the average electron rotational speed $\langle\omega_e\rangle$ be less than ω or the RMF force will produce drive in the wrong direction. A basic quantity for RMF current drive is the ratio of diamagnetic toroidal line current naturally present to reverse the external field, $I'_{rev} = 0.5\langle n_e\rangle e\langle\omega_e\rangle r_s^2 = 2B_e/\mu_o$ to the maximum possible synchronous line current $I'_{sync} = 0.5\langle n_e\rangle e\omega r_s^2$. This ratio has been given the name ζ,

$$\zeta = \frac{\langle\omega_e\rangle}{\omega} = \frac{I'_{rev}}{I'_{sync}} = \frac{2B_e/\mu_o}{0.5\langle n_e\rangle e\omega r_s^2} = \frac{2x10^{-4}B_e(mT)}{\langle n_e(10^{20}m^{-3})\rangle\,\omega(10^6 s^{-1})\,r_s^2(m)} \quad . \qquad [2.2]$$

As long as ζ is less than unity, and the RMF drive is strong enough to overcome electron-ion friction, the RMF will penetrate just far enough to maintain I'_{rev}. Current drive will be most effective when ζ is in the range 0.3-0.7.

The azimuthal force produced by the RMF on the electrons is given by $F_{RMF} = n_e e\langle -v_{ez}B_r\rangle$. For the $\zeta < 1$ partial penetration case this force is only present near the outer edge. In equilibrium with E_θ everywhere zero, radial flows will automatically be set up so that the total azimuthal force $F_\theta = n_e e(\langle -v_{ez}B_r\rangle + v_{er}B_z)$ exactly equals the frictional force $F_\eta = n_e m_e \nu_\perp(v_{e\theta} - v_{i\theta})$ at all radii. It is thus most useful to analyze the equilibrium requirements in terms of torques.[8] For the partially penetrated case a simple rigid rotor analytic expression for F_{RMF} is $(2B_\omega^2/\mu_o)(r_s/r)^2\exp\{-2(r_s-r)/\delta^*\}$, which can be integrated to yield an RMF torque per unit length of

$$T'_{RMF} = \frac{2\pi r_s^2 B_\omega^2}{\mu_o}\left(\frac{\Delta r}{r_s}\right) \quad . \qquad [2.3]$$

Δr is used here as an effective penetration since in actual numerical calculations it is governed by both ζ and λ, especially when λ is not too large. In equilibrium this drive torque will equal the resistive torque,

$$T'_\eta = \frac{\pi}{2} m_e\langle n_e\nu_\perp\omega_e\rangle r_s^4 = \frac{\pi}{2}\eta_\perp\langle n_e^2\omega_e\rangle e^2 r_s^4 \quad . \qquad [2.4]$$

Otherwise poloidal flux will change according to the approximate relationship

$$\frac{d\phi_p}{dt} = 2\pi R E_{\theta R} = \frac{2}{n_e e R^2}\left(T'_{RMF} - T'_\eta\right) \qquad [2.5]$$

where $R = r_s/\sqrt{2}$ is the radius of the field null.

The relationship for the rate of flux change is derived from integrating $\int E_\theta 2\pi r^2 dr$ from 0 to r_s, using the relationship $E_\theta = (F_\theta - m_e n_e \nu_\perp v_{e\theta})/en_e$, and expressing E_θ as $E_{\theta R}(2-(r/R)^2)$ for $r > R$ and as $E_{\theta R}(r/R)^2$ for $r < R$. This expression for rate of flux change is double that given in Ref. 8, where a less appropriate profile for E_θ was used. In numerical terms

$$\frac{d\phi_p}{dt} = 1.25\frac{B_\omega^2(mT)}{n_e\left(10^{20}m^{-3}\right)}\left(\frac{\Delta r}{r_s}\right)\left(1-\frac{T'_\eta}{T'_{RMF}}\right)\ \text{Wb/s}\ . \qquad [2.6]$$

If the RMF torque exceeds the frictional torque, the FRC will expand radially (and compress axially depending on fueling and energetics), compressing the external flux and raising the density until the torques are balanced. Unlike low beta devices where the density can be influenced by fueling and other factors, an RMF driven prolate FRC's density is set by the RMF drive parameters and plasma resistivity, with heating and fueling only affecting the FRC length. For typical values of B_ω = 5 mT, an average n_e of $0.1\text{x}10^{20}$ m^{-3} and $\Delta r/r_s \sim 0.1$, the rate of flux rise when T'_η/T'_{RMF} is small will be about 30 mWb/msec, and it should thus take about 0.1 msec to reach typical flux levels of 2 mWb. This is consistent with the measured rates of field rise.

If one calls $\langle n_e^2\omega_e\rangle = (\langle\beta\rangle n_{em})^2\langle\omega_e\rangle = (\langle\beta\rangle n_{em})^2\zeta\omega$ in Eq. (2.4) and equates Eq. (2.4) with Eq. (2.2), one arrives at a relationship for peak electron density

$$n_{em} = \frac{\sqrt{2}B_\omega}{e\left(\mu_o\eta_\perp\omega r_s^2\right)^{1/2}}\sqrt{\frac{2\Delta r/r_s}{\zeta\langle\beta\rangle^2}} = \frac{0.079B_\omega(\text{mT})\sqrt{2\Delta r/r_s\zeta\langle\beta\rangle^2}}{\left(\eta_\perp(\mu\Omega\text{–m})\,\omega\left(10^6\,\text{s}^{-1}\right)r_s^2(\text{m})\right)^{1/2}}\ \text{x}10^{20}\,\text{m}^{-3}\ . \qquad [2.7]$$

Since we do not know, without conducting detailed numerical calculations, the detailed relationship between the somewhat artificial $\Delta r/r_s$ and ζ ($\Delta r/r_s \approx 0.5\langle\beta\rangle\zeta$ has been used in the past), it is useful to state the density scaling in terms of a required value of the non-dimensional ratio

$$\frac{\gamma}{\lambda} = \frac{\sqrt{2}B_\omega}{en_{em}\left(\mu_o\eta_\perp\omega r_s^2\right)^{1/2}} = \frac{0.79B_\omega(mT)}{n_{em}\left(10^{20}m^{-3}\right)\left(\eta_\perp\omega r_s^2\right)^{1/2}} = \frac{1}{2}\langle\beta\rangle\lambda\zeta\left(\frac{B_\omega}{B_e}\right)\ . \qquad [2.8]$$

The last form for expressing γ/λ in Eq. (2.8) is often useful. We will always use $\eta_\perp$ in units of $\mu\Omega$-m and the characteristic quantity ωr_s^2 in units of $10^6\text{s}^{-1}\text{m}^2$ from now on. We will also always use γ/λ based on $\nu_\perp = n_{em}e^2\eta_\perp/m_e$, with $\eta_\perp$ specified.

Utilizing Eq. (2.8) we can now write the achievable peak electron density as

$$n_{em} = \frac{\sqrt{2}B_\omega}{e\left(\mu_o\eta_\perp\omega r_s^2\right)^{1/2}(\gamma/\lambda)_{req}} = \frac{0.079B_\omega(\text{mT})x10^{20}\,\text{m}^{-3}}{\left(\eta_\perp\omega\, r_s^2\right)^{1/2}(\gamma/\lambda)_{req}} \qquad [2.9]$$

Eq. (2.9) is thus equivalent to having an effective $(\Delta r/r_s) = 0.5(\langle\beta\rangle/(\gamma/\lambda)_{req})^2\zeta$. $(\gamma/\lambda)_{req} = 1/\sqrt{2}$ has also been used previously for estimating the effective plasma resistivity, but that is too simplistic for illuminating detailed scaling dependencies.

The Eq. (2.9) relationship is only dependent on the plasma temperature inasmuch as it affects the resistivity, and to some extent $(\gamma/\lambda)_{req}$. The plasma temperature depends on the RMF only through its energy input. The external field reached is thus not solely determined by the RMF, but is given by

$$B_e = \sqrt{2\mu_o n_{em}kT_t} = \sqrt{40\,n_{em}\left(10^{20}\,\text{m}^{-3}\right)T_t(\text{eV})}\ \text{mT}\ . \qquad [2.10]$$

Using this pressure balance the parameter ζ can be expressed in terms of the total temperature as

$$\zeta \;=\; 0.00126\,\frac{\left(T_t(\mathrm{eV})\;/\;n_{em}\left(10^{20}m^{-3}\right)\right)^{1/2}}{\langle\beta\rangle\omega r_s^2}\;. \qquad [2.11]$$

It is also useful to write the ratio of B_e to B_ω as

$$\left(\frac{B_e}{B_\omega}\right) \;=\; \frac{\langle\beta\rangle\lambda\zeta}{2(\gamma/\lambda)_{req}}\;. \qquad [2.12]$$

In our latest analysis we use the resistivity, as measured from the absorbed power, to compare achieved densities and external magnetic fields with those predicted by modeling. We also use numerical calculations to derive $(\gamma/\lambda)_{req}$ rather than simply setting it to a constant value. Since the basic non-dimensional parameters for RMF drive are γ, λ, and ζ, with the latter two determining the required γ, we develop scaling dependencies in terms of λ and ζ. For large λ we would expect $(\gamma/\lambda)_{req}$, based on a sharp boundary analysis, to approach a fixed value close to 1.25, and $(\Delta r/r_s)$ to depend only on ζ (linearly), but for small λ, where most of our experiments were conducted, the high relative diffusivity will cause the $(\Delta r/r_s)$ dependence on ζ to be weaker and there to be an inverse dependence on λ. (It should be noted that λ is based on the full separatrix radius r_s, but the RMF penetration should really be related to the smaller distance $r_s - R = 0.29r_s$, so that a value of 0.29λ is more indicative of the current drive regime.) For simplicity we assume that $(\Delta r/r_s)$ scales as ζ^y/λ^x. Using the relationship for ζ in Eq. (2.2), the resistive torque can be written to scale as $T_\eta \propto \eta_\perp B_e^2/\omega\zeta$. This form is used to get a relationship in terms of B_ω and B_e, which are the two most accurately measurable quantities: $(B_e/B_\omega) \propto (\omega r_s^2/\eta_\perp)^{0.5-x/4}\zeta^{(1+y)/2}$.

Numerical calculations were performed for TCS conditions with $\omega = 0.55\text{x}10^6$ s^{-1} and $B_\omega = 6$ mT. $\eta_\perp$ was varied from 63 to 315 $\mu\Omega$-m and T_t from 20 to 125 eV in order to cover a range of λ from 12 to 28 and a range of ζ from 0.25 to 0.9. Other calculations, directly aimed at high frequency operation, were run with $\omega = 1.6\text{x}10^6$ s^{-1}, $T_t = 35$ eV, and $\eta_\perp$ varying between 63 and 250 $\mu\Omega$-m. λ varied between 47 and 22, and ζ between 0.32 and 0.44 in those simulations. All calculations fit well to a $B_e/B_\omega = 24.8\zeta^{0.6}/\eta_\perp^{0.35}$ (x = 0.6, y = 0.2) relationship which, since r_s always reached about 0.35 m, yields a scaling of approximately

$$\left(\frac{B_e}{B_\omega}\right)_s \;=\; 63\left(\frac{\omega r_s^2}{\eta_\perp}\right)^{0.35}\zeta^{0.6} \;=\; 0.59\lambda^{0.7}\zeta^{0.6}\;. \qquad [2.13]$$

The parameter $\lambda = 794(\omega r_s^2/\eta_\perp)^{1/2}$ is used in the second relationship to facilitate comparison with previous work. Using Eq. (2.12), this yields a scaled value of

$$\left(\frac{\gamma}{\lambda}\right)_{reqs} \;=\; 0.85\langle\beta\rangle\lambda^{0.3}\zeta^{0.4}\;. \qquad [2.14]$$

Equations (2.13) and (2.14) are used for comparisons with measured values in our analysis. The relationships are only applicable up to values of about $\lambda = 50$ for which the numerical calculations were made, but this covers all present experimental results. For λ greater than about 50, analytical and numerical calculations show a value of $(\gamma/\lambda)_{req}$ approaching approximately 1.25. At fairly low λ, $(\gamma/\lambda)_{req}$ is about $1/\sqrt{2}$ as has been used previously.

The numerical results can be used to arrive at a more accurate scaling for density than simply choosing a fixed value of $(\gamma/\lambda)_{req}$. Substituting Eq. (2.14) into Eq. (2.9),

$$n_{ems}\left(10^{20}\,\mathrm{m}^{-3}\right) = \frac{0.093 B_{\omega}(\mathrm{mT})}{\left(\eta_{\perp}\omega r_s^2\right)^{0.5}\langle\beta\rangle\zeta^{0.4}\lambda^{0.3}} \ . \qquad [2.15]$$

One further piece of analysis which is needed is a method of evaluating the effective plasma resistivity from absorbed power measurements. This requires some knowledge of the current profiles. A typical measured $B_z(r)$ profile is shown in Fig. 2-1, and compared with a rigid rotor (RR) profile, $B_z = B_e tanhK((r/R)^2\text{-}1)$, and a numerically calculated profile. A range of excursion for the measured $B_z(r)$ is shown to represent the fluctuations in the measurements. The calculation was run at the same ω, B_ω, and T_t as measured experimentally. A value of $\eta_\perp = 150$ μΩ-m was used in the calculation in order to match the experimentally achieved external field. The calculated internal field is higher than the external field due to the pressure contribution of the RMF B_θ, but this is not usually seen experimentally even though the separatrix pressure is near zero. The reason is probably due to the contribution from centrifugal force, which was not included in the numerical MHD calculations where $v_{i\theta}$ was arbitrarily held to zero. Plasma rotation requires the edge magnetic field to be higher than the central magnetic plus field pressure in order to balance the centrifugal pressure. This is discussed in Sections 2.2 and 4.5.

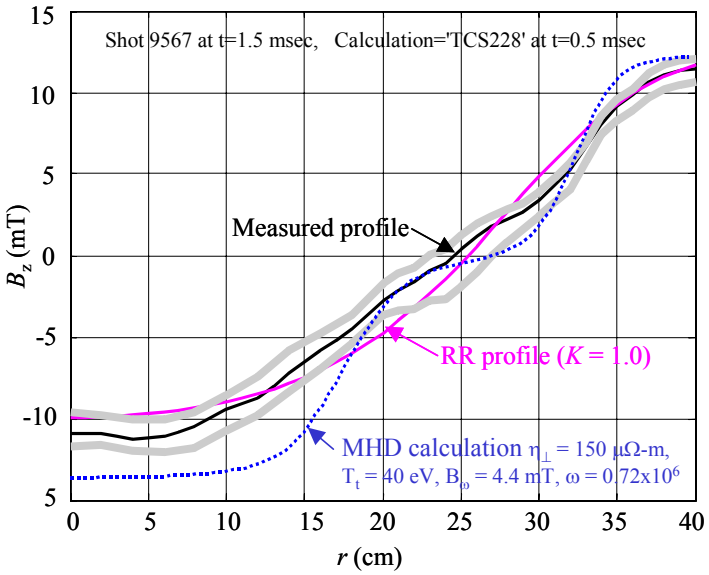

Figure 2-1. Measured and calculated magnetic field profiles. The calculation used $B_\omega = 4.4$ mT, $\omega = 0.72\text{x}10^6$ s^{-1}, and $T_t = 40$ eV. Final calculation values

The calculated $B_z(r)$ profile is also seen to exhibit considerably more flattening near the field null than is seen in the experiments. Such flattened profiles would be expected

at low ζ and high λ where the RMF penetration should be shallow. They were seen on the smaller STX device,[12] and are seen on TCS under some conditions, but strongly flattened profiles are not typical of TCS operation. There is again influence due to centrifugal force since (d/dr)(p $+B_z^2/2\mu_o$) must equal $\rho\omega_i^2/r$, but recent numerical calculations (not included here) show that the centrifugal force is mostly balanced by pressure gradient at the field null, and non-flattened $B_z(r)$ profiles tend to arise due to non-uniform resistivity. Since the RR profile agrees best with experimental data, we use it for power analysis computations.

Based on the RR profile with $n_e(r) = n_{em} sech^2 K((r/R)^2-1)$ and $j_\theta = -n_e \omega_e e r$, the absorbed power due to azimuthal currents, $P_{abs\theta} = \int \eta_\perp j_\theta^2 2\pi r dr \ell_s$, becomes

$$\begin{aligned} P_{abs\theta} &\approx \frac{2\pi}{\langle\beta\rangle}\eta_\perp\left(\frac{B_e - B_i}{\mu_o}\right)^2 f(K)\,\ell_s \\ &= \frac{4\eta_\perp(\mu\Omega - m)}{\langle\beta\rangle}\left(B_e(mT) - B_i(mT)\right)^2 f(K)\,\ell_s(\mathrm{m})\ \mathrm{W} \end{aligned} \quad . \qquad [2.16]$$

$f(K) = 1 - 0.33 tanh^2 K$ and is about 0.8 for typical values of $K \sim 1.0$, but an integration of the actual profiles, accounting for the range of fluctuations, showed that use of Eq. (2.16) is more appropriate with an $f(K)$ value of unity. Since we actually measure the total absorbed power due to both theta and axial currents, $P_{abs} = P_{abs\theta} + P_{absz}$, we need some means of assigning the relevant fraction to $P_{abs\theta}$, in order to determine $\eta_\perp$. If the axial currents are assumed to flow in the region Δr, while the theta currents are approximately rigid-rotor, the ratio of $P_{absz}/P_{abs\theta}$ should scale as $(B_\omega/B_e)^2/(\Delta r/r_s)$. The numerical calculations showed that the effective value of $\Delta r/r_s$ scaled as $\zeta^{0.2}/\lambda^{0.6}$. For our data analysis we use the numerically calculated power ratios, which can be well represented by

$$\frac{P_{abs\theta}}{P_{abs}} = \frac{1}{1 + 0.69(B_\omega/B_e)^2 \lambda^{0.6}/\zeta^{0.2}} \quad . \qquad [2.17]$$

2.2 Ion Rotation

Ion rotation can not only lower the maximum synchronous current, but it also tends to drive rotational instabilities, particularly the n = 2 rotational flute. This mode often develops in TCS when the plasma radius is compressed inwards from the wall. The mode can degrade the plasma performance by locally ablating the quartz vacuum wall, introducing silicon and oxygen impurities into the plasma. Rotational instability is often observed in conventional FRCs due to diamagnetic rotation. In previous experiments, multipole fields have been used to stabilize these modes. External flux rings reduced the tendency to develop rotational distortions in TCS, and it is hoped that internal flux rings planned for the TCS modification will be a further help. Eventually, however, some active means of counteracting the RMF torque will most likely have to be used.

It has previously been stated that, in contrast to the electrons where it is necessary that $\omega_{ce} >> \omega$, the ions should have $\omega_{ci} < \omega$ in order to not also be directly driven by the RMF. Even neglecting RMF azimuthal forces on the ions, there must be some drag term that is large compared with the electron-ion friction if the ions are not to spin up to large paramagnetic velocities. We will represent this by an effective collision frequency ν^*, which can be due to a combination of ion-neutral collisions, viscosity, or even radial electric field shorting. (Obviously, if the ions are rotating paramagnetically, there must be a strong radial electric field to confine them.) In the simple case where the RMF force on the ions is negligible, the ions will attain a steady azimuthal velocity, related to the electron azimuthal velocity, of

$$\alpha \equiv \frac{v_{i\theta}}{v_{e\theta}} = \frac{1}{1+\left(\nu^*/\nu_{ie}\right)} \qquad [2.18]$$

The condition for the RMF azimuthal force on the ions to be small compared to the azimuthal force on the electrons, can then be expressed as

$$\frac{\omega_{ci}^2}{\nu^{*2}+\omega^2} << \frac{\nu_{ie}}{\nu^*} \ . \qquad [2.19]$$

Since we need $\nu^* >> \nu_{ie}$ for α to be small, and ν^* will generally be much less than ω, this condition is even more restrictive on the ion cyclotron frequency than having $\omega_{ci} < \omega$. However, it is the amplitude of the radial component, B_r, that should be used in ω_{ci}, and $|B_r|$ tends to always be much less than B_ω when the RMF only partially penetrates the plasma column.

In order to study the forces driving the ions and electrons, and derive Eqs. (2.18) and (2.19), we will do a local analysis assuming B_r and B_θ are given. Assuming the additional drag term acts only on the ions, the equations of motion for the electrons and ions are

$$nm_e \frac{D\mathbf{v}_e}{Dt} = -ne(\mathbf{E}+\mathbf{v}_e\times\mathbf{B}) - \nabla p_e - nm_e\nu_{ei}\left(\mathbf{v}_e-\mathbf{v}_i\right) \qquad [2.20]$$

$$nm_i \frac{D\mathbf{v}_i}{Dt} = ne(\mathbf{E}+\mathbf{v}_i\times\mathbf{B}) - \nabla p_i - nm_i\nu_{ie}\left(\mathbf{v}_i-\mathbf{v}_e\right) - nm_i\nu^*\,\mathbf{v}_i \ . \qquad [2.21]$$

Since we are only capable of doing a local analysis here, we cannot solve the radial equation, and we will assume $v_r = 0$, which eliminates any dependence on B_z. From Faraday's law $E_r = \omega r B_r = \omega r B_\omega$, taking B_r as real using the notation of Eq. (2.1). We do not need B_θ if v_r is taken as zero. The oscillating quantities of importance are thus v_z and B_r, and the phase of v_z with respect to B_r is critical. The electron equations were used to derive the results of Section 2.1, and here we will address the ion equations.

$$\hat{\theta}: \quad 0 = e\left\langle v_{iz}B_r\right\rangle + m_e\nu_{ei}\left(v_{e\theta}-v_{i\theta}\right) - m_i\nu^*\,v_{i\theta} \qquad [2.23]$$

$$\hat{z}: \quad m_i i\left(\omega-\frac{v_{i\theta}}{r}\right)v_{iz} = e\left(E_z - v_{i\theta}B_r\right) + m_i\nu_{ie}\left(v_{ez}-v_{iz}\right) - m_i\nu^*\,v_{iz} \qquad [2.24]$$

It is useful to call the ion rotational speed $\omega_i = v_{i\theta}/r$ and define a relative velocity $\varpi_i = \omega - \omega_i$. For the case where electron-ion friction is small compared to the other forces, the ion axial oscillation velocity will be $v_{iz} = \{\omega_{ci}/(\varpi_i^2+\nu^{*2})\}(\nu^* - i\varpi_i)\varpi_i r$. ϖ_i will usually be greater than ν^* and this velocity will be mostly imaginary (lagging B_r and E_z by 90°), but the real component is still important. The direct RMF drive force on the ions will then be $e\langle v_{iz}B_r\rangle = m_i\{\omega_{ci}^2/(\varpi_i^2+\nu^{*2})\}\nu^*\varpi_i r$. This can be compared to the friction force due to the electrons, $m_i\nu_{ie}\varpi_i r$. For $\varpi_i \sim \omega$, comparing these two forces leads to the relationship in Eq. (2.19). Comparing the electron-ion friction to the electron drive term $e\langle v_{ez}B_r\rangle$ leads to the relationship $\varpi_e \approx 2(\nu_{ei}/\omega_{ce})^2\omega$ which has often been used for the fully penetrated case. The electrons then oscillate with a velocity $v_{ez} = (\nu_{ei}/\omega_{ce})\omega r = (\nu_{ie}/\omega_{ci})\omega r$ and the real part of the ion oscillation will exceed the electron oscillation when the RMF force on the ions becomes greater than the electron-ion frictional force.

This essentially 'fully penetrated model' is very simplistic for a real FRC but it illustrates some of the basic scaling. As long as the RMF does not exert a significant azimuthal force directly on the ions, a condition given in Eq. (2.19), then the ion rotational speed must be a balance between electron friction and drag. The ion spin-up time can be calculated by solving the simple equation

$$\frac{d\omega_i(t)}{dt} = \nu_{ie}\left(\omega_e - \omega_i(t)\right) - \nu^*\omega_i(t) \ . \qquad [2.25]$$

The solution is $\omega_i(t) = \alpha\omega_e(1-\exp(-t/\tau_{su}))$, with the spin-up time constant τ_{su} given by

$$\tau_{su} = \left(\nu_{ie} + \nu^*\right)^{-1} \ . \qquad [2.26]$$

Typical values in TCS are $\upsilon_{ie} \approx 1\text{x}10^4$ s^{-1} and $\upsilon^* \approx 4\text{x}10^4$ s^{-1}, leading to a spin-up time of only 20 μs and a steady state ion azimuthal rotation frequency $\omega_i/\omega_e = 0.2$.

As the rotating magnetic field strength is increased and the frequency is lowered, the condition in Eq. (2.19) may no longer be satisfied; that is, the RMF azimuthal force directly on the ions will be appreciable compared to electron-ion friction. Another way to view this is that the ions are becoming magnetized in the RMF. In this case, the electron and ion equations are coupled and must be solved numerically. Eqs. (2.20) and (2.21) have been solved numerically using a

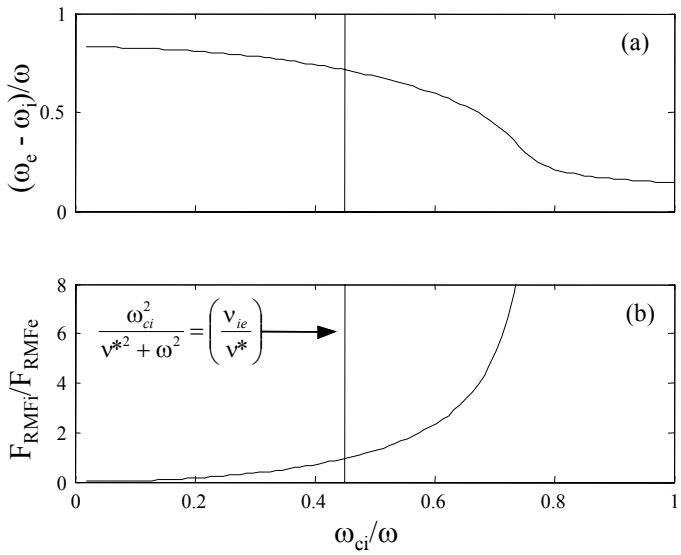

Figure 2-2. Two fluid solutions with $\omega_{ce}/\nu_{ei} = 20$ and $\nu^*/\nu_{ie} = 5$ for a) differential electron minus ion rotation frequency and b) ratio of RMF force directly

nonlinear least-squares iterative solver. The resulting differential rotation (ω_e-ω_i) at conditions typical of TCS is shown in Fig. 2-2. The rotation is plotted versus the dimensionless quantity ω_{ci}/ω. It should be noted that in a true FRC equilibrium, the plasma screens the RMF field and so the radial magnetic field is at most about a tenth of the vacuum value. Thus, the actual ratio $\left(\omega_{ci}/\omega\right)$ may be considerably lower than the vacuum value. The point where $\frac{\omega_{ci}^2}{\upsilon^{*2}+\omega^2}=\left(\frac{\upsilon_{ie}}{\upsilon^*}\right)$ is also shown. Beyond this point, as either the RMF strength is raised or the frequency is lowered, the resulting current drive diminishes as the ions are driven directly by the RMF.

2.3 MHD and Rotation Effects

Experimental data is often compared with the predictions of our MHD r-θ RMF code. An important aspect of this code is its ability to include some 3D effects by forcing pressure to be a constant on a flux surface p = p(ψ), and adjusting the axial length so that $\langle\beta\rangle = 1 - \tfrac{1}{2}x_s^2$. The condition p = p(ψ), is only valid if the ions are not rotating; a condition normally forced in the code. If the ions are rotating, the pressure on the outer field lines should exceed the pressure on the inner field lines.

In its present form, the code can include rotation effects, and even calculate the rate of spin-up due to electron-ion drag, but then the p = p(ψ) condition is not valid. Thus we normally zero the θ component of velocity. It is now thought that rotation should be included in the code, since it can affect the pressure profile, and perhaps the radial flow. To do this the p = p(ψ) condition will have to be modified. If the plasma is free to flow parallel to the magnetic field there will be no **j×B** force on the plasma. The pressure relationship is the same as the pressure ratios for a rotating fluid in the absence of magnetic fields.

In equilibrium, and assuming uniform temperature, the momentum equation $\rho(\mathbf{u}\cdot\nabla\mathbf{u}) = -\nabla p$ can be expressed as

$$\frac{\mathrm{d}p}{\mathrm{d}r} = \frac{m_i\omega^2}{kT}\,pr\,. \qquad [2.27]$$

Integrating this between inner, r_i, and outer, r_o, flux surfaces yields

$$\frac{p_o}{p_i} = \exp\left\{\frac{m_i\omega^2}{2kT}\left(r_o^2 - r_i^2\right)\right\}. \qquad [2.28]$$

Our RMF code is being modified to include this effect, and perform simulations with the approximation that the ions must rotate rigidly, rather than forcing the azimuthal component of ion motion to zero. Even without doing this, we can make some calculations of centrifugal pressure effects.

In equilibrium pressure balance can be expressed as:

$$\nabla p = \mathbf{J} \times \mathbf{B} + \rho r \omega_i^2 \qquad [2.29]$$

The radial component is $\frac{\partial p}{\partial r} = J_\theta B_z - \langle J_z B_\theta \rangle + \rho r \omega_i^2$, where $J_\theta = \frac{-1}{\mu_o}\frac{\partial B_z}{\partial r}$, and $\langle J_z B_\theta \rangle$ is the time averaged value of $J_z B_\theta$. Integrating this expression from r = 0 to r yields:

$$p + \frac{B_z^2}{2\mu_o} + \int_0^r \langle J_z B_\theta \rangle dr - \frac{1}{2}\langle \rho \rangle \omega_i^2 r^2 = p(0) + \frac{B_z^2(0)}{2\mu_o}, \qquad [2.30]$$

where $p(0)$ is the pressure at $r = 0$, and $B_z(0)$ is the axial magnetic field at r = 0. The pressure term due to the RMF B_θ will be near zero except near the FRC edge for the partially penetrated case, and for convenience we will call $\int_0^{r_s} \langle J_z B_\theta \rangle dr = B_\omega^2/\mu_o$ since the RMF B_θ component is approximately doubled near the separatrix.

It is informative to evaluate Eq. (2.30) at two points, $r = R = r_s/\sqrt{2}$ and $r = r_s$. Calling the external field pressure $P_f = (B_e^2 + 2B_\omega^2)/2\mu_o$, and assuming $p(r_s) = 0$, these become

$$p_m - \frac{1}{4}\langle \beta \rangle m_i n_{em} (\omega_i r_s)^2 = p(0) + \frac{B_z^2(0)}{2\mu_o} \quad \text{and} \quad P_f - \frac{1}{2}\langle \beta \rangle m_i n_{em} (\omega_i r_s)^2 = p(0) + \frac{B_z^2(0)}{2\mu_o}.$$

The peak pressure at the field null then becomes

$$p_m = P_f\left(1 - \frac{0.25\langle \beta \rangle m_i n_{em} (\omega_i r_s)^2}{P_f}\right) = P_f\left(1 - \frac{5220\langle \beta \rangle (\omega_i r_s)^2}{T_f(\text{eV})}\right) \qquad [2.31]$$

for deuterium. where we define $T_f = P_f/n_{em}k$. For typical parameters, $\langle \beta \rangle = .6$, $m_i = 3.35\text{x}10^{-27}$ kg, $r_s = .4$ m, $T_f = 40$ eV, and $\omega_i = 0.05\text{x}10^6$ s^{-1}, $p_m = 0.97P_f$ This reduction in central pressure is not normally large, but it increases rapidly with increasing ω_i. Experimental measurements of rotation seem to hover around a value where centrifugal force starts to become significant. Perhaps this is the point where the n=2 instability develops, leading to wall contact and a viscous drag to prevent the rotation from increasing further.

One other factor can be seen from the above calculations. The sum of magnetic plus plasma pressure at $r = 0$ is reduced by $0.5\langle \beta \rangle n_{em}(\omega_i r_s)^2$. If $p(0)$ were close to zero, one would expect $|B_z(0)|$ to be greater than B_e due to the contribution from the RMF B_θ. However, the centrifugal contribution can reverse this tendency, which is often what is seen in experiments.

III. TCS FACILITY

3.1 Design Summary

A drawing of the TCS plasma chamber is shown on Fig. 3-1. TCS is composed of two of the old LSX 80-cm diameter, 1.25-m long clear quartz plasma tubes, joined in the middle by a plastic section providing vacuum diagnostic access. The quartz tubes are connected at each end to 45° thin walled stainless steel conical sections, reinforced with fiberglass-epoxy. These, in turn, are connected to a 27-cm diameter stainless tube at the downstream end, and the previous 27-cm diameter TRAP acceleration section quartz plasma tube at the upstream end. Octopole protection straps were provided (only at the downstream cone) to try and reduce contact of translated FRCs with the chamber walls, but this was not very effective. Tanatlum protection over the downstream cone eliminated visible ablation which was observed on unprotected stainless steel.

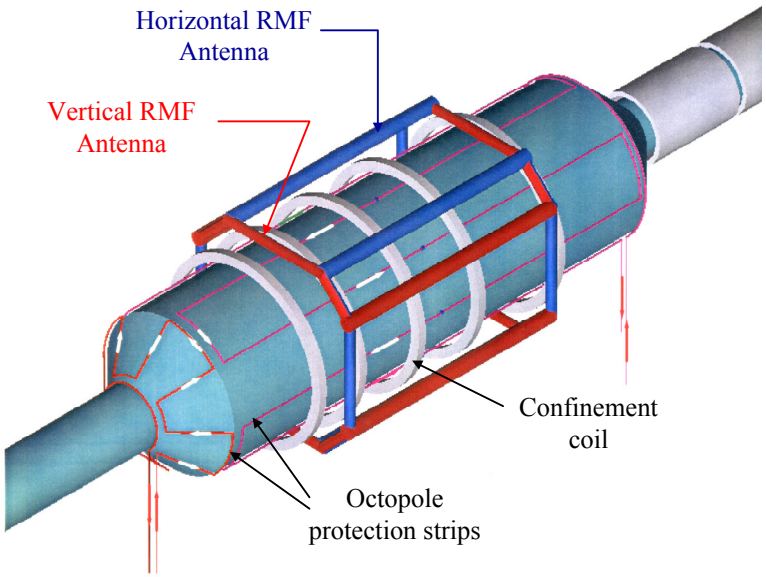

Figure 3-1. TCS confinement chamber showing the RMF

The overall design of TCS, with the LSX/mod Reversed Field Theta Pinch (RFTP) formation section, is sketched on Fig. 3-2. Three of the old TRAP 3-turn acceleration coils were left to form the transition between LSX/mod and TCS. The total length of TCS is about 3 meters. LSX/mod has a 40-cm diameter, ~3-m long quartz plasma tube and many single-turn coils to allow for programmed formation. The basic system consists of eight coils on 25-cm spacings, with the two center coils forming a single unit. Along with the next outer coils, they form a 1-m long 'compression' section. Trigger and plug coils bring the total active coil length to 2 meters. There is also a quasi-steady 0.5-m long plug coil on the upstream end to mirror the effects of the first accelerator coil. Barrier strips are provided to reduce plasma-wall contact during field reversal, and puff fill valves are located at the far upstream end. Several of the coils have ringing capacitor banks to allow for efficient preionization. The coil and attached capacitor bank parameters for all coils are listed in Table 3-1.

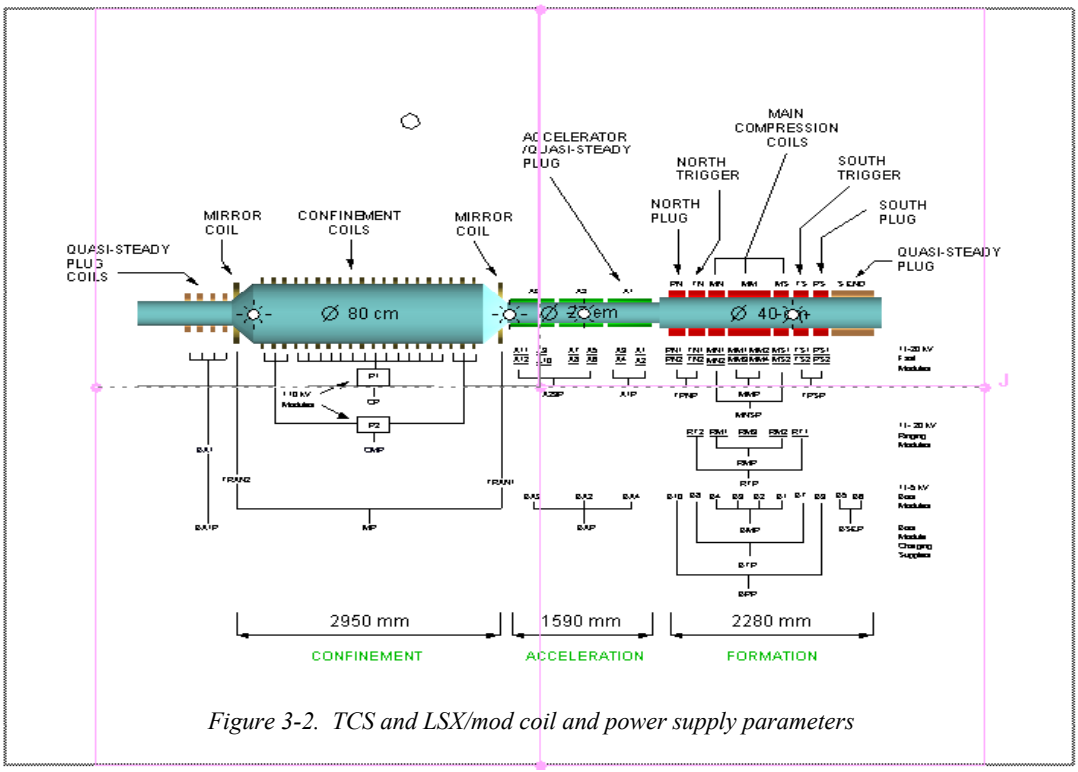

Figure 3-2. TCS and LSX/mod coil and power supply parameters

Table 3.1
TCS & LSX/mod Power Supply Parameters

Coil	Supply	C-tot (μf)	L-tot (μh)	R-st (mOhms)	t-1/4 (μs)	2L/R (μs)	I-max (kA)	Icoil/Ic (MA/m)
S.End lc=49cm rc=23cm	Bias(±5kV)	1440	1.16	18.6	64.1	124.2	211	0.42
Plug/Trig	Bias(±5kV)	720	4.9	33	93.3	296.7	89	0.4
lc=22cm	Ring(±20kV)	35	2.09	33.6	13.4	124.4	147	0.54
rc=23cm	Main(±20kV)	70	1.41	16.8	15.6	167.9	257	0.95
Main	Bias(±5kV)	1440	2.39	16.5	92.2	289.7	179	0.35
lc=51cm	Ring(±20kV)	35	1.69	33.6	12.1	100.3	162	0.26
rc=23cm	Main(±20kV)	140	0.67	8.4	15.2	158.3	527	0.86
Accel	Bias(±5kV)	720	5.23	16.5	96.4	633.3	101	0.6
lc=50cm rc=23cm	Main(±20kV)	56	1.28	8.4	13.3	304.8	253	1.17
Mirror lc=6cm rc=35cm N=121turns	Bias(±5kV)	360 (720)	20mh	260	4.2ms (6.0ms)	150ms	1.35 (1.82)	0.16 (0.22)
Confinement lc=2.6m rc=47cm N=56turns	Plug(+10kV)	8mf	0.95mh	1.7	4.3ms	230ms	28	0.6
End Plug lc=46cm	Bias(+5kV)	720	4.2mh	80	2.7	105ms	4	1.4

For RMF formation studies, all discharges are preceded by a puff of D_2 from the LSX/mod upstream puff fill valves, which filled the TCS chamber to an atom density about equal to or less than the final FRC electron density. This generally occurred 200 msec before the RMF discharge was initiated. Seven and one-half msec before RMF initiation a second short puff was introduced into LSX/mod and its coils were rung to send down a pulse of preionized gas, resulting in a measured average electron density of about $10^{18}m^{-3}$ in TCS before RMF application.

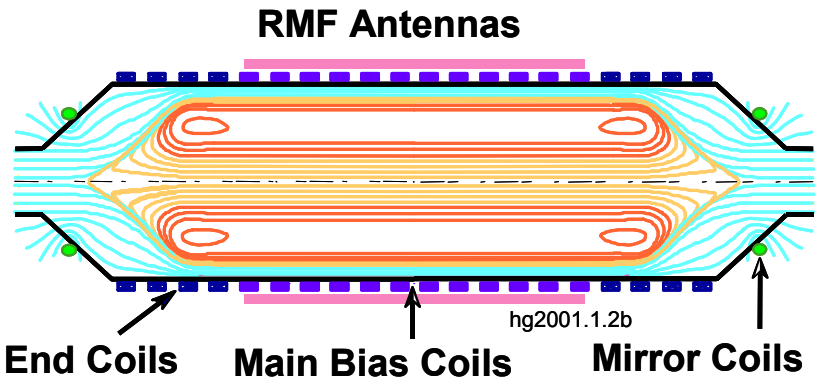

Figure 3-3. Sketch of TCS chamber

Details of the TCS chamber are shown on Fig. 3-3. Twenty 56-turn coils provide an axial confinement field. The coils are wound using 3/16" copper conductor. They have an I.D. of 35" (44.5 cm radius), an O.D. of 39.25" (49.8 cm radius) and a width of 1.62" (4.1 cm), and are spaced on a 12.5 cm interval (slightly wider at the center to allow for vacuum diagnostic access). The effective flux conserving radius has been measured as r_c = 47 cm. The center 14 coils are connected in parallel (main bias coils) and powered by one 4-mf capacitor bank charged by the CP power supply. The 3 coils on each end (end coils) are powered by a second 4-mf capacitor bank charged by CMP. CP and CMP are 10 kV supplies but were only used at several 100 volts for the RMF start-up experiments. The ignitron switches used in the capacitor banks were replaced by IGBTs for this low voltage, low current operation. Separately powered 121-turn (24.7" I.D., 29.8" O.D., 2.45" wide) mirror coils are located as shown in Fig. 3.

The RMF antennas shown on Fig. 3-1 were constructed out of 3" diameter copper pipe and placed just outside the confinement coils at a radius of r_a = 54 cm. Each antenna, horizontal and vertical, was composed of two ~1.6-m long Helmoltz-like loops at 30° angles

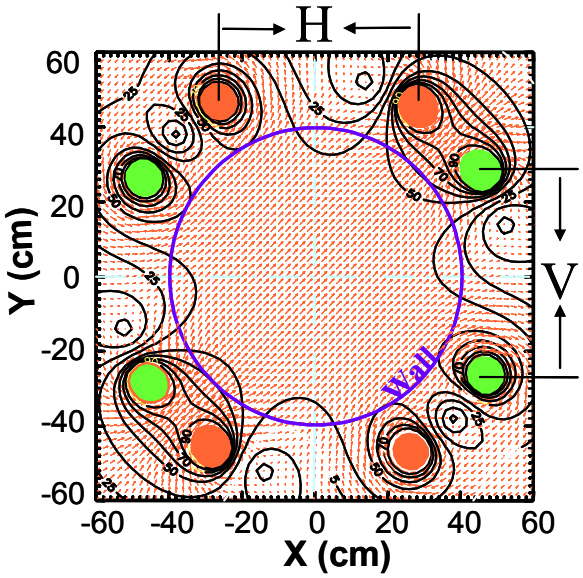

Figure 3-4 Calculated RMF vacuum fields.

to the horizontal (for the vertical field antenna) or to the vertical (for the horizontal field antenna). The RMF field can be expressed as a series of odd modes

$$\mathbf{B}_{\mathrm{RMF}} = \sum_{n=1,3,5} \mathbf{B}_n e^{i(\omega t - n\theta)} \quad . \qquad [3.1]$$

Modes higher than n=1 will rotate slower, and even in the wrong direction. The antenna rods were spaced azimuthally to minimize contributions from the n=3 mode. Calculations show that the ratio r_s/r_a should be less than 0.7 for reduction of the n=5 and higher modes to low levels which allow efficient current drive. Calculations of the RMF field for the TCS antenna arrangement are shown in Fig. 3-4. Although the field uniformity inside the plasma tube appears very good, there are still small n=5 and higher contributions. However, experiments with the antennas located at r_a = 50 cm and r_a = 60 cm did not exhibit much differences in overall performance.

An important aspect of the RMF antennas is its inductance since, for the parallel tank circuit used, the antenna current will be $I_{ant} = V_{ant}/\omega L_{ant}$. The inductance of a simple rectangular loop of length b, width a, and pipe radius δ is given by

$$L_{loop} = \frac{\mu_o}{\pi}(a+b)\left[\ln\left(\frac{2ab}{\delta(a+b)}\right) - 0.25\right] .$$

The 0.25 factor is for a hollow pipe. For our main antenna with a length b = 1.6 m and width a = 1.0 m, the inductance is given by $L_{loop} = 1.0\{\ln[(123/\delta)] - 0.25\}$ μh. The total inductance of the antenna pair is given by $L_T = (L_{loop} + M)/2$, where M is the mutual inductance between the pair of loops forming the Helmholtz-like geometry. *Grover* (p. 77)[13] gives the mutual inductance between two circular loops as M = fr where r is the radius and f = 0.0078 μh/cm for a factor $k'^2 = \{1 + 4(r/d)^2\}^{-1} = 0.110$ where d is the spacing between loops (50 cm). Taking r as $\sqrt{(ab/\pi)}$, the mutual inductance M = 0.55 μh for our antennas. Thus, most of the antenna inductance comes from the self inductance of the individual pipes, and it is useful to make the pipes of large diameter (or large width strips).

The calculated inductance for the 1.6-m long TCS antennas are shown in Table 3.2 as functions of the pipe radius. Our primary antennas used 3" diameter (3.75 cm radius) copper pipe, and had a measured inductance of 1.8 μh. When we used 3.8 cm wide copper strip, the inductance increased to 2.5 μh. Thus the strip acted equivalently to about a 1 cm radius pipe. The strip appears to have a similar self inductance to a pipe with the same circumference as both sides of the strip.

Table 3.2
Antenna Inductance Versus Pipe Radius

Radius δ(cm)	L_{loop} (μh)	L_T (μh)
0.5	5.26	2.91
1.0	4.56	2.56
2.0	3.87	2.21

We plan to use 1-m long antennas on the modification to TCS. Then $L_{loop} = 0.8\{\ln[(100/\delta)] - 0.25\}$ μh and $k'^2 = 0.166$, f = 0.0058 and M = 0.32 μh. A 2" diameter pipe (2.5 cm radius) antenna would then have an inductance of L_{loop} = 2.75 μh and L_T = 1.54 μh.

3.2 Operation of LANL RMF Pulser

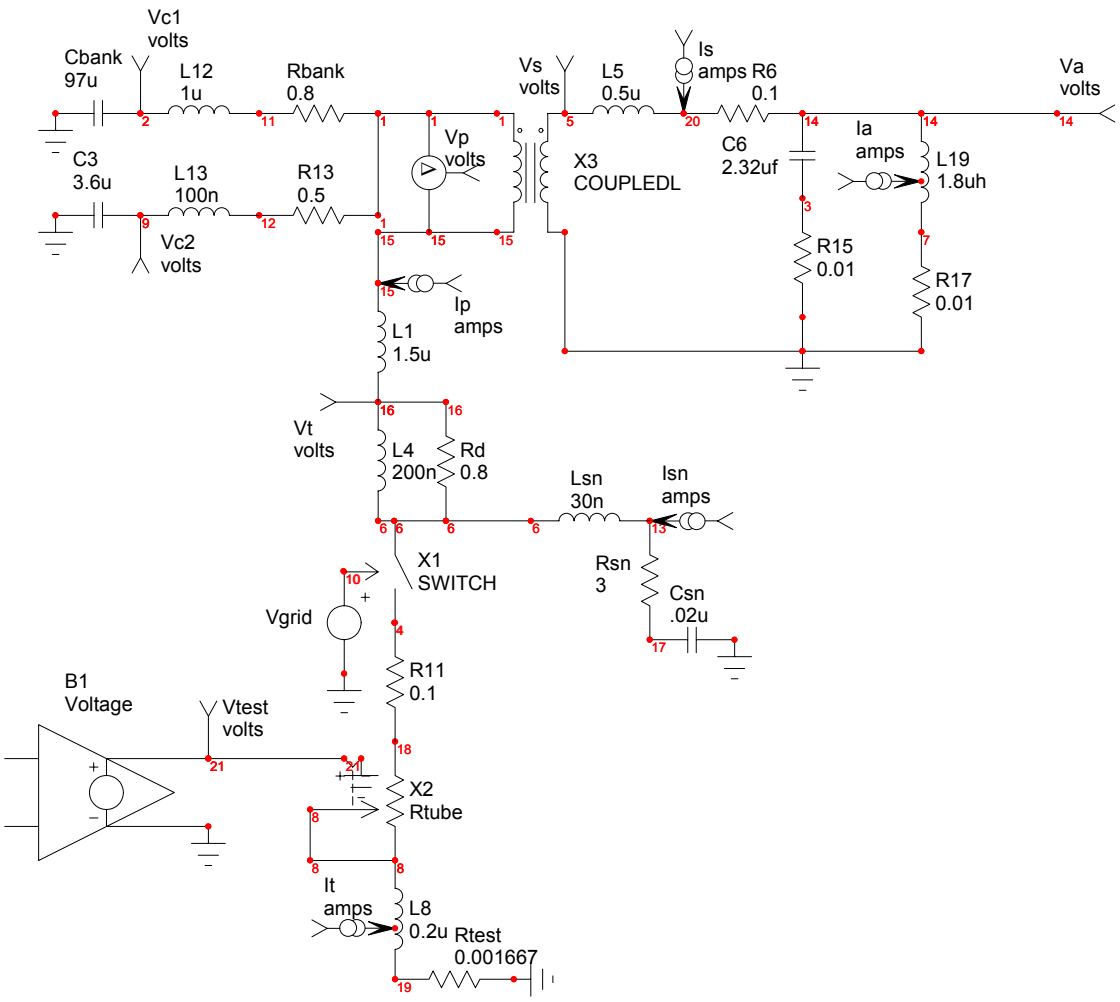

Figure 3-5. SPICE model of RMF pulser and TCS antenna.

Each of the two LANL pulsers drives an RMF antenna which is made part of a parallel resonant tank circuit in order to produce high circulating currents. A SPICE mock-up of the circuit is shown in Fig. 3-5. A near perfect 1:1 transformer, X_3, is specified with an open circuit inductance of 23 μh and a coupling coefficient of K = 0.99. R17 can be used to represent the effect of plasma loading. The tank circuit capacitor C_6 is chosen to match the specified frequency applied to the opening and closing switch X1. The six-tube plasma resistance is represented by the current dependent voltage pot R_{tube}.

For sinusoidal inputs the resonant circuit has an impedance given by

$$Z_c = \left\{ \frac{1}{R_{15} + \left(1/i\omega C_6\right)} + \frac{1}{R_{17} + i\omega L_{19}} \right\}^{-1} . \qquad [3.2]$$

Calling $L_{19} = L$, $C_6 = C$, $R_{17} = R$, ignoring R_{15} as << R, and defining the excursion from resonance as $R_t = \omega L - 1/\omega C$, the tank circuit impedance is given by

$$Z_c \approx \frac{L/C - iR/\omega C}{R + iR_t} . \qquad [3.3]$$

This is approximately equal to $L/CR = (\omega_R L)^2/R$ for the resonant frequency $\omega = \omega_R = (LC)^{-1/2}$ when $R << (\omega L)$. Increasing the inserted resistance R reduces the impedance seen by the pulser, and thus increases the current it must supply.

The maximum power the pulser can supply is determined by its intrinsic impedance. For a simple sinusoidal pulser with a resistive internal impedance R_p, it is easy to show that maximum power transfer occurs at $Z_c = R_p$. However, the LANL pulsers are far from simple. They supply current in only one direction, the pulses are square, and the resistance is not constant. This variable resistance is inserted in the SPICE circuit through the voltage controlled pot R_{tube}. The resistance and effective formula used in the SPICE model are derived from the tube voltage-current specifications for a 2 kV grid voltage, and are shown on Fig. 3-6. The Machlett ML8618 triodes are listed as allowing a peak current of 240 A each, which amounts to 1.44 kA for the six tubes. It can be seen that the tube voltage-drop and effective tube resistance rise sharply when the total tube current exceeds that value, effectively limiting the maximum pulser current to about 1.6 kA. The tubes have a specified peak plate voltage of 45 kV, but due to their advanced age they should not be subjected to more than 30 kV. Since the peak tube plate voltage increases to about double the supply voltage during pulser operation, the pulser capacitor bank charge should be limited to 15 kV. For the TCS antenna circuit, raising the voltage further would not yield greatly higher power transfer since the tubes would already be drawing their maximum possible currents at any significant loading.

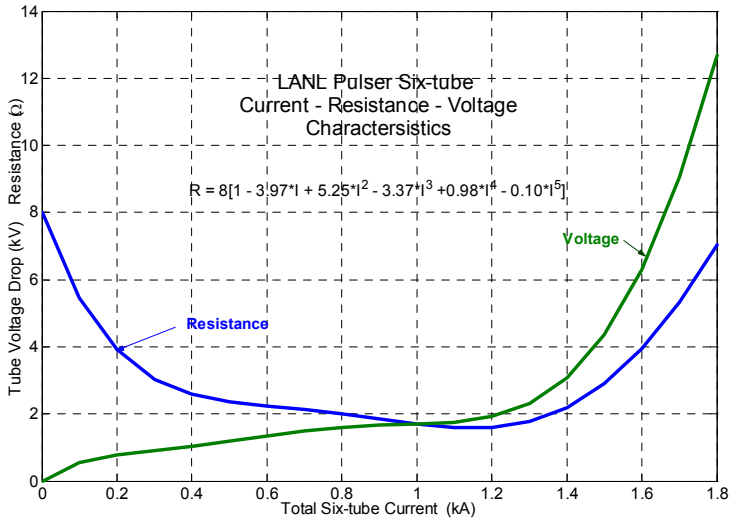

Figure 3-6. Pulser tube resistivity specified in SPICE model.

Based on the curves in Fig. 3-6 one might think that the effective pulser resistance R_p was between 2 and 4 Ohms, and peak power transfer to the load would occur near $Z_c = 3$ Ω. However, when considering how the pulser operates, the effective pulser resistance should be considered as four times this value. If the transformer secondary current (I_s in Fig. 3-5) is $\pm I_s$, the power dissipated is $0.5Z_cI_s^2$. (Since the antenna current $I_a = (\omega L/R)I_s$, this is the same as $0.5RI_a^2$.) In order to produce a peak-to-peak transformer current of $2I_s$,

the pulser must supply one-directional pulses of $2I_s$. Since this current is only present about one-half the time, the dissipated tube power will be $2R_pI_s^2$. Maximum load power should thus occur for $Z_c = 4R_p \approx 12\Omega$. A plus-minus pulser would have half the effective resistance, but the same efficiency could be accomplished by doubling the number of tubes in a one-directional pulser. One advantage of a plus-minus pulser would be to eliminate the net average current supplied to the transformer, but this will decay away on an L_s/R_s timescale where $L_s = 23$ μh is the transformer inductance and $R_s = R_6 + R_{17}$ is the circuit resistance to a dc current.

A series of SPICE calculations were run with different load resistances $R_{17} = R$ for three different pulser frequencies. The tank capacitance C_6 was adjusted to provide resonance at the pulser frequency. Results for the antenna voltages, currents, and absorbed power are shown in Fig. 3-7 at 125 μsec after pulsing begins. That allows time for the tank circuit to be charged up, and the results are approximately quasi-steady except for a gradual decay in supply voltage V_c. As can be seen, peak power transfer occurs at about $Z_c = 12$ Ω in agreement with the previous discussion. This can be seen more clearly in Fig. 3-8 where the antenna voltage and load power are plotted as functions of Z_c.

The load resistance R_{17} used in SPICE is only indicative of the effects of plasma loading. It is really Z_c that is the key parameter. Thus, a value of $R_{17} = 0.1$ Ω at an 81 kHz pulser frequency represents the same plasma loading as a value of $R_{17} = 0.4$ Ω at a 162 kHz pulser frequency. The pulser performance when scaled in this manner, however, is still somewhat poorer at the lower frequency. This is probably due to the non-sinusoidal nature of the pulser current pulses. The higher frequency components of the pulses see an impedance approximately equal to $i\omega(L_5 + (\omega_R/\omega)^2L_{19})$, which is much larger for higher ω when ω significantly exceed the resonant frequency ω_R. At lower ω, the higher frequency components will further load down the pulser.

The detailed performance of the pulser can be seen in the individual calculations of Figs. 3-9 and 3-10 for a low and high load resistance at the 81 kHz frequency. The 1.6 msec long calculations were run with a relatively small supply capacitor (100 μf total) in order to observe the total power lost by the system. For the high loading case with R = 0.2 Ω ($Z_c = 4.3$ Ω) Fig 3-9a shows the initial voltage decay dV_{c1}/dt to be about 6.2 kV/ms, so that at 125 μsec when $V_c = 11$ kV the initial power loss $C_{bank}V_{c1}dV_{c1}/dt$ is about 6.9 MW. The antenna current I_a is ±4.1 kA (on top of an average value of 0.3 kA), yielding an absorbed load power of $0.5RI_a^2 = 1.7$ MW. This is quite a bit below the maximum possible absorbed power of 2.7 MW shown on Figs. 3-7 or 3-8.

Details of the pulser operation at high loading are shown on Fig. 3-9b. The tube current is at its maximum value of 1.6 kA for the full duration of the pulse (5 μsec with 0.1 μsec rise-time and 0.3 μsec fall-time). During this pulse time the tube voltage drop V_t is about 6.5 kV, yielding a tube dissipation of 4.3 MW. The remaining 0.9 MW is dissipated in other elements, mainly the capacitor supply resistors and the snubber resistance R_{sn}.

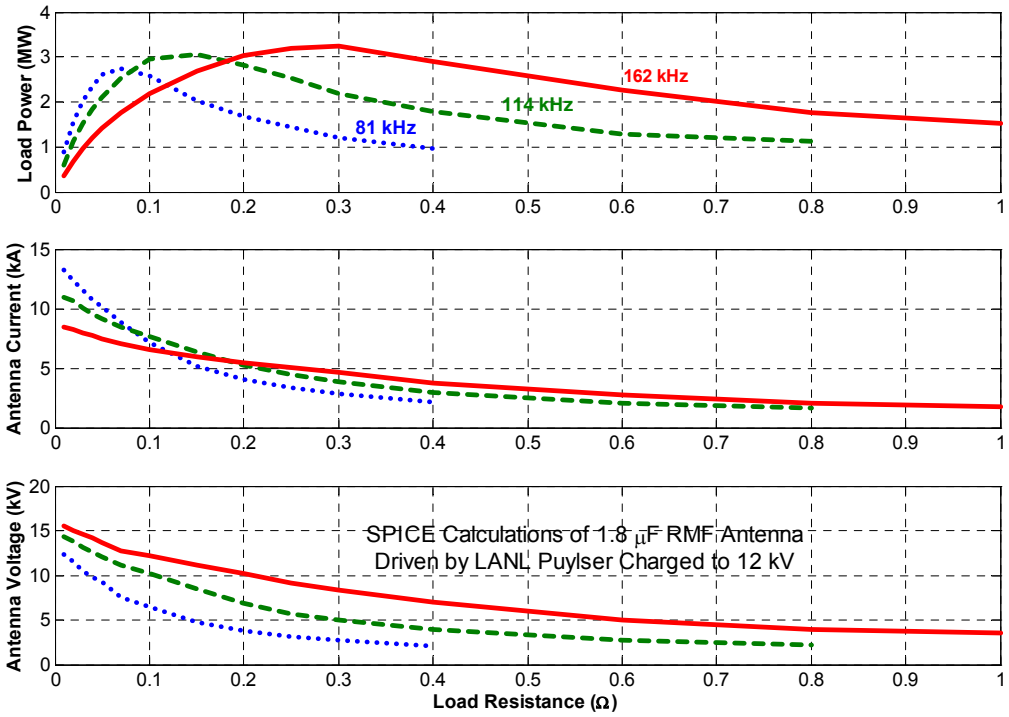

Figure 3-7. Antenna calculations as a function of specified load resistance.

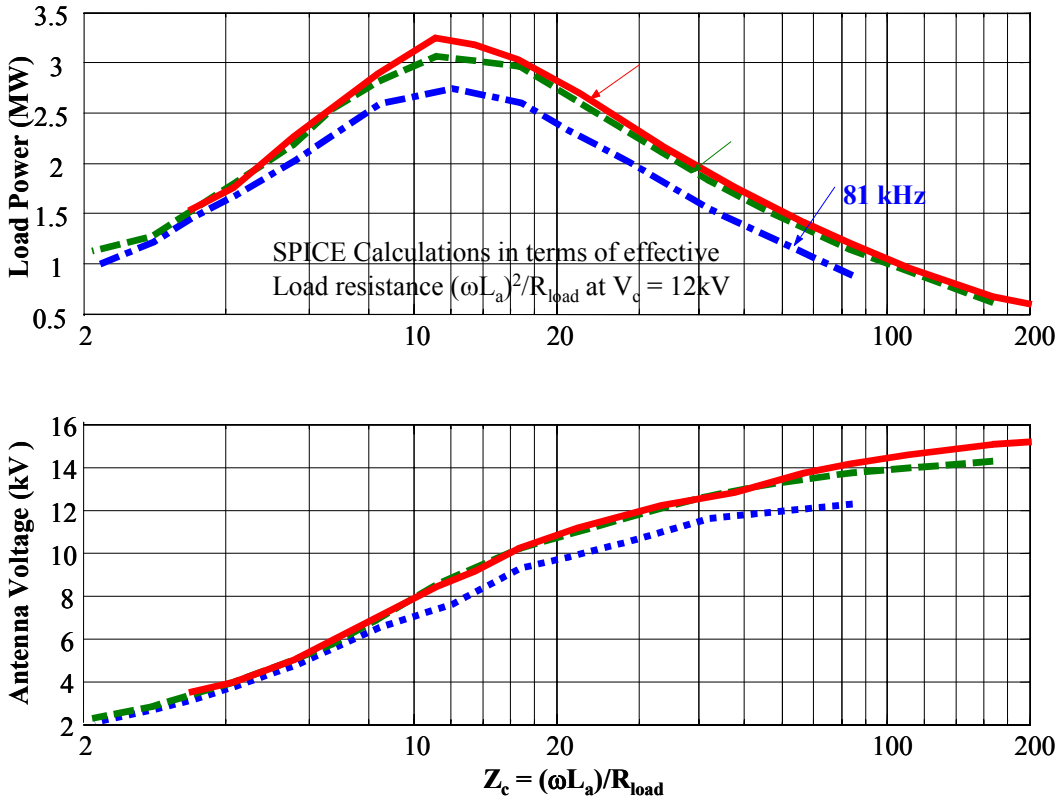

Figure 3-8. Antenna calculations versus tuned circuit impedance Z_c.

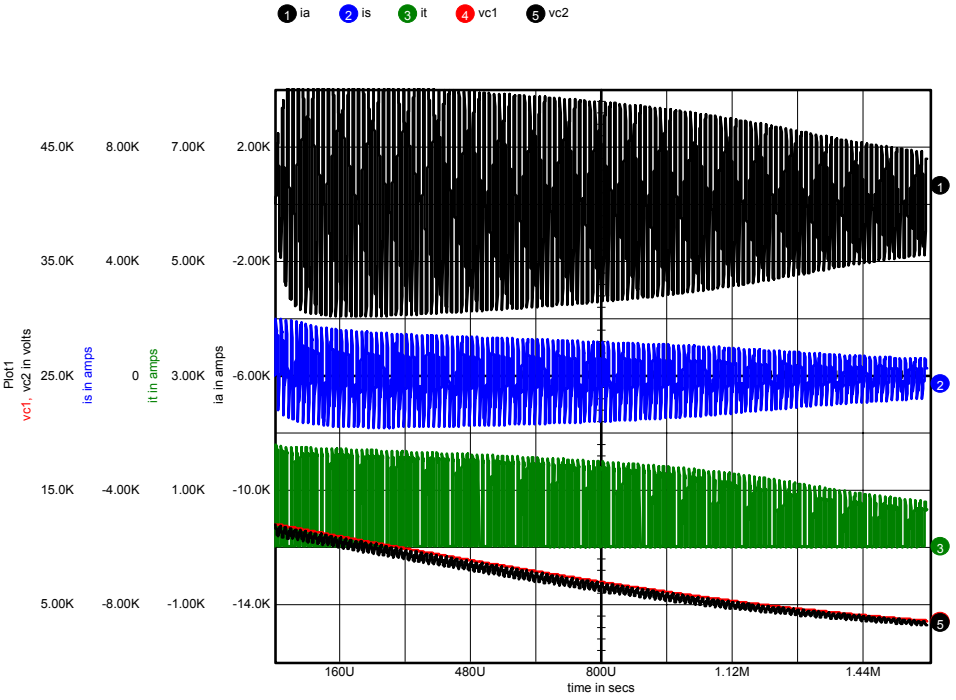

Figure 3-9a. SPICE calculation for 0.2Ω load resistor – 81 kHz, 12 kV.

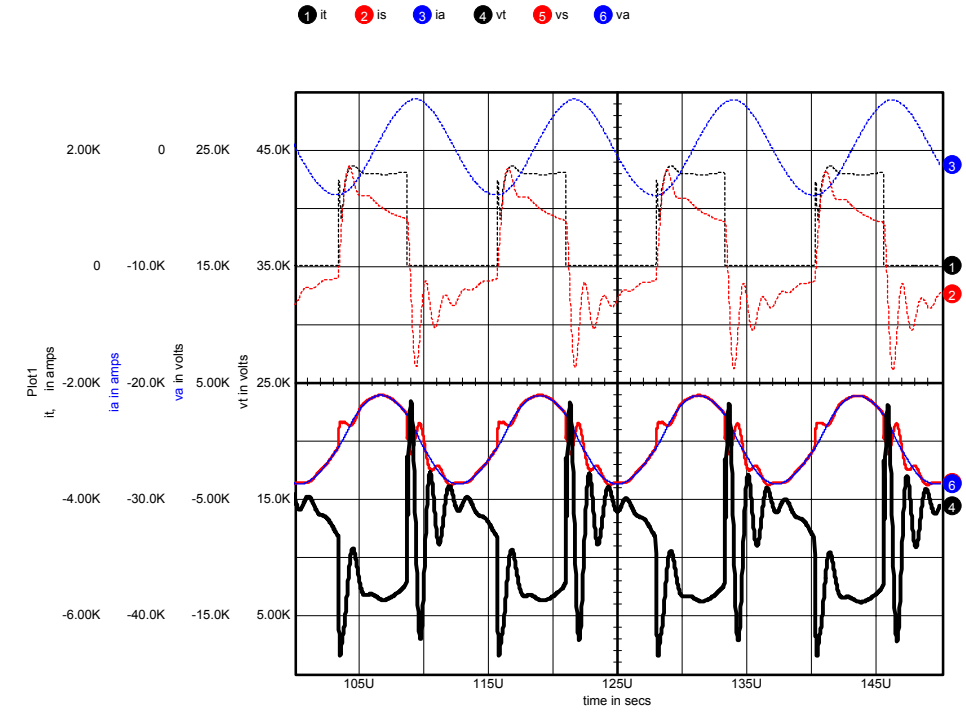

Figure 3-9b. Details of 0.2Ω SPICE calculation.

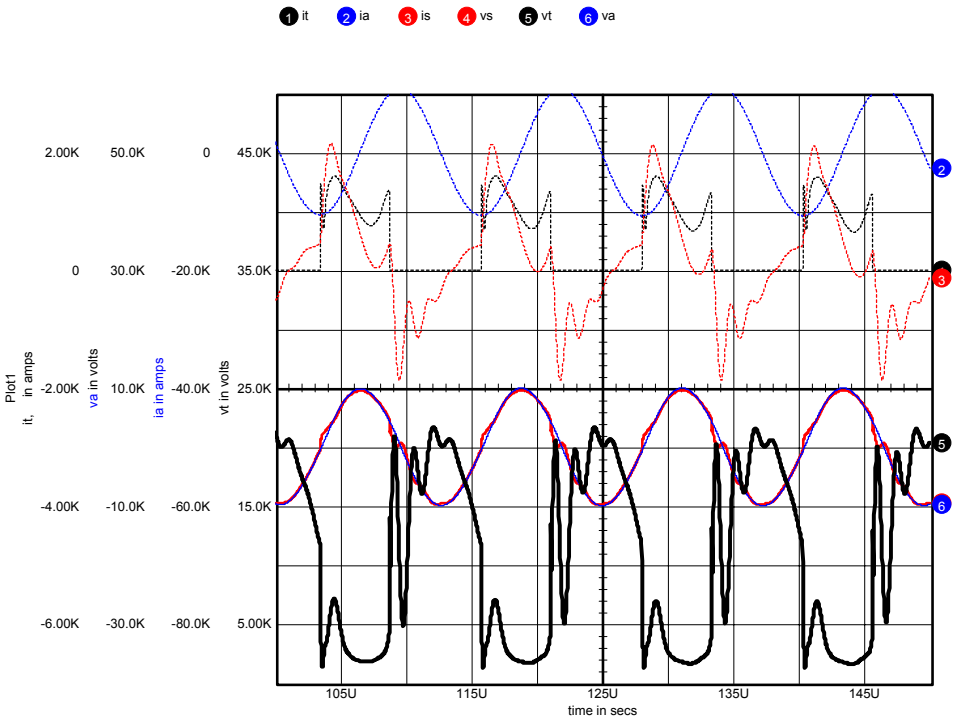

Figure 3-10b. Details of 0.04Ω SPICE calculation.

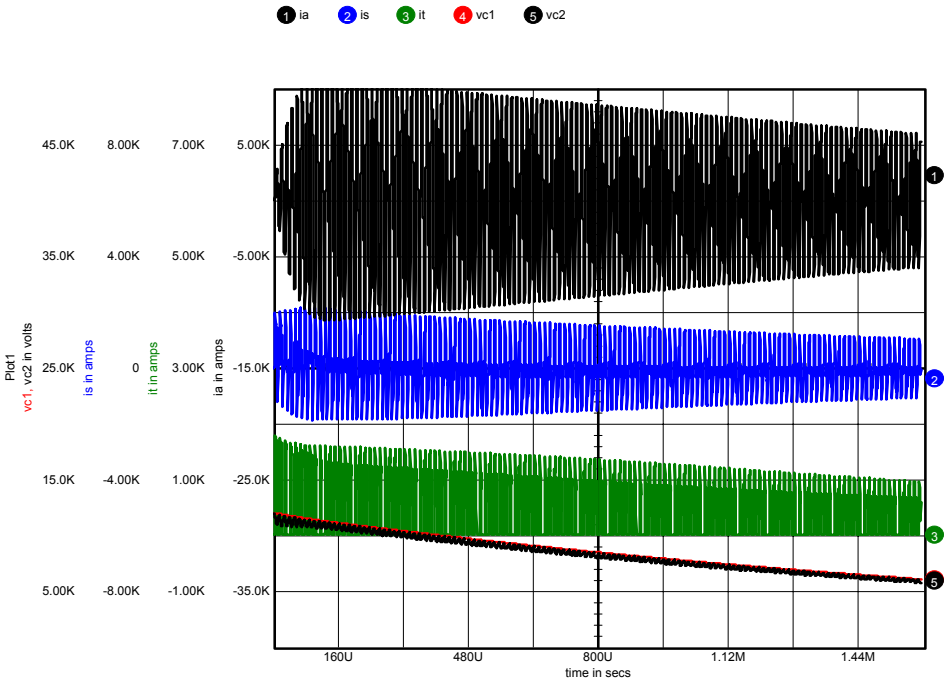

Figure 3-10a. SPICE calculation for 0.04Ω load resistor – 81 kHz, 12 kV.

The snubber capacitance is rather small, yielding the convoluted voltage traces with large overshoots, and the very asymmetrical transformer current pulses I_s. Surprisingly, SPICE calculations show the overall pulser performance to be very insensitive to the snubber component values, with the primary transformer current becoming more symmetric as the snubber capacitance increases, but the overall antenna current dropping slightly. Lower than 0.12 μf snubber capacitance per tube would result in dangerous tube plate voltage excursions.

Calculations for a low loading case (R = 0.04 Ω, Z_c = 21 Ω) are shown on Fig. 3-10. In this case the supply voltage decays at only 4.25 kV/msec, yielding a total power loss of 4.7 MW. The antenna current is now ±10.8 kA (on top of a 0.2 kA average current), for a load dissipation of 2.3 MW. It can be seen from Fig. 3-10b, that the tube current is no longer at its maximum throughout the pulse. If the loading were made even smaller, the tube current would decrease slightly, but it would mainly stay on for a shorter time. For the Fig. 3-10b calculation, assuming that during half the pulse the tube current is about 1.4 kA, with a tube voltage drop of ~4kV, and during the other half the tube current is ~1.0 kA, with a tube voltage drop of ~2kV, the resultant tube power would be 1.6 MW. About 0.8 MW would then be attributable to the rest of the circuit.

All-in-all it is impressive how well the pulser works over a wide loading range. However, the tube voltage drop limits the maximum power output to about 3 MW per pulser, with transfer efficiencies under 50%. The performance is significantly better at higher frequencies, especially at higher loadings (higher Z_c) where the primary currents are high. Higher antenna voltages can be achieved for the same Z_c at the higher frequencies but, of course the antenna current, $I_a \approx V_a/\omega L$ will then be smaller. A step-up transformer would ideally then be useful, but practically it could not be built as efficiently as the present 1:1 transformers, and the performance would probably not be better than for the 81 kHz operation. A lower inductance antenna would also, of course, allow for higher antenna currents at low loadings, but neither solution would increase the maximum possible pulser output power. The only means to do that would be to use more, or less lossy switching elements. An ideal solution, especially at the lower frequencies where high power IGBTs like to operate, would be to use a few parallel stacks of IGBTs. However, that would require a large development effort as the total primary circuit resistance would have to kept to under about 1 Ohm, and the delicate solid-state elements would have to be protected against over-voltages and currents. The present Machlett tubes have the advantage or ruggedness, and were a good choice at the time based on their availability at no cost.

In order to predict how the pulser may operate with split antennas SPICE calculations were run with L_{19} in Fig. 3-5 reduced to 0.5 μh. The antenna voltage and power delivered to the load are shown on Fig. 3-11 as a function of the tuned circuit impedance. The results are nearly identical to the 81 kHz calculations for the L_{19} = 1.8 μh antenna, which is not surprising since ωL for that case was 0.92 Ω while ωL for this case is 0.67 Ω.

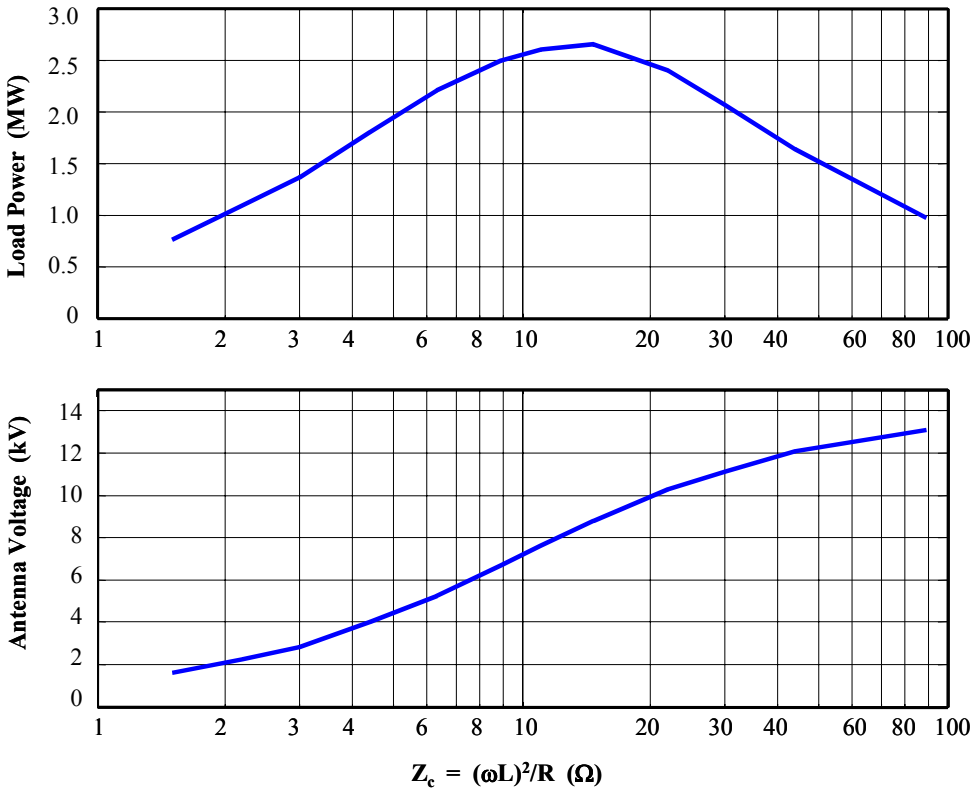

Figure 3-11. Antenna calculations versus Z for L_a = 0.5 μh at 12 kV and 212 kHz.

A split antenna is used to lower the inductance of each half so that higher antenna currents can be produced at high frequencies. Splitting the antenna into two sections and running them both in parallel lowers the inductance by a factor of 4. The pulser frequency can then be doubled without reducing each antenna section's current. For given plasma conditions the effective plasma resistance reflected into the circuit (R_{17} in Fig. 3-5) will also be lowered by a factor of 4. The circuit impedance $Z_c = (\omega L)^2/R$ will then remain the same, and match the pulser impedance, but at double the old frequency. The total tank circuit current will be doubled, but the tank circuit Q = ωL/R will also be doubled, so that the secondary current will remain unchanged. The only detriment to the split antennas will be the larger effect of stray inductances and resistances in the connections between the tuning capacitors and the split antennas due to the higher current there. That is why the calculations were run for L_{19} = 0.5 μh instead of 0.45 μh (old $L_{19}/4$).

3.3 Diagnostics

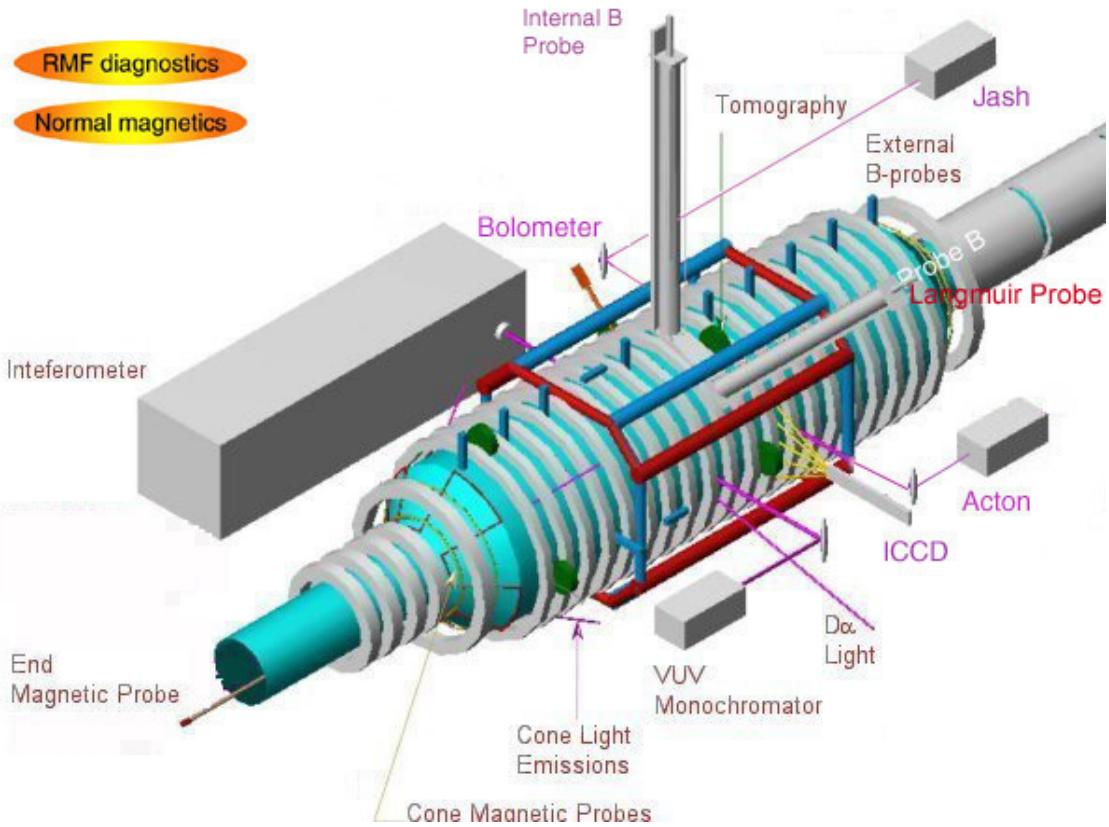

Figure 3-12. TCS Diagnostic Set

A sketch of the TCS diagnostic set is shown in Fig. 3-12. This sketch is available on the TCS data Web-site, and the descriptions of various diagnostics can be obtained by clicking on them. The individual diagnostics are described in Appendix A.

3.4 Prototype Experiments

The previously built STX facility was kept operational for several purposes. The principal ones were to explore new technologies for use on TCS, and to develop methodologies to be used on the new TCS modifications. The two most important of these were to put in internal flux rings, which demonstrated that they did not short out the RMF axial electric field, and the use of a magnetized cascade arc source (MCAS)[14] to supply ionized plasma to refuel the FRC, instead of relying on simple recirculation (as stipulated in numerical models) or ionization of a neutral background. Use of the MCAS, in conjunction with a much smaller plasma chamber, operating at a much smaller value of the key ωr_s^2 parameter, but higher B_ω than possible in TCS, produced interesting results in a much different operating regime than seen on TCS. These results will be described in this section, although it is probably more desirable to read Section 4 first, on the type of 'standard' operation that is described in Section 2.

The testing of the internal flux rings was conducted in a 27-cm diameter quartz plasma tube, attached to one end of the old 40-cm diameter STX. The experiments using the MCAS were conducted in a 14-cm diameter quartz tube, also attached to STX. This smaller configuration was called STX-HF. A sketch is shown in Fig. 3-13. The high 0.3 T axial field in the MCAS was tapered down to about 20 mT in the RMF region to spread out the plasma jet radially. The MCAS is known to produce a nearly fully ionized plasma flow, with neutral flow further limited in our configuration by a coaxial low conductance 2.5 cm diameter, 50 cm long quartz tube. The MCAS current was between 100 to 200 Amps, with an observed plasma flow speed of ~3x10^4 m/s. The main STX-HF plasma chamber was 50 cm long and 14 cm in diameter. Axial fields were provided by 8 parallel-fed 14-turn solenoidal coils with an effective flux conserving radius of r_c = 7.5 cm. The RMF antennas were 17 cm long and fed in series with tank capacitors by the old STX IGBT RMF power supplies. Series resonant operation allows high voltages to be produced on the RMF antennas without a high voltage source, but has the disadvantage of producing an antenna current that depends on the loading.

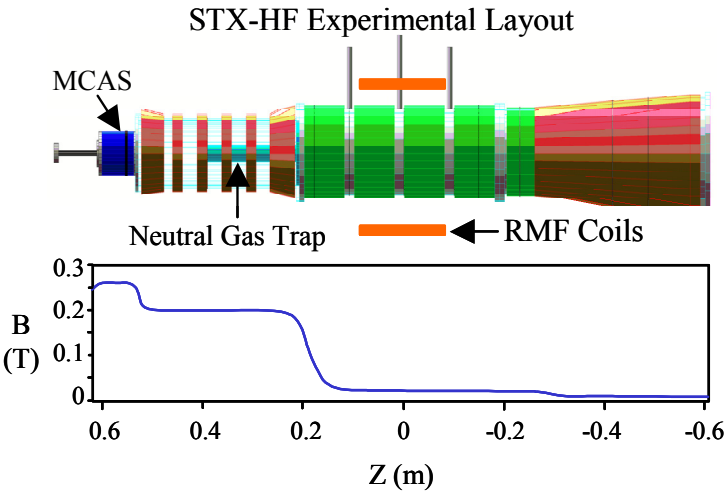

Figure 3-13. Schematic of STX-HF with initial vacuum field

The RMF on STX was run at a frequency of $\omega = 2.3\times10^6$ s^{-1} (365 kHz), about 40% higher than the highest frequency used on TCS, but at higher B_ω values of 9 mT. However, the FRC separatrix radius was only about 5.3 cm, about one-seventh of the FRC radius on TCS. Thus, the key ωr_s^2 parameter was only 6.5x10^{-3} (using the 10^6s^{-1}-m^2 units of Section 2) compared to the smallest parameter of 0.08 seen on TCS at the lowest $\omega = 0.52\times10^6$ s^{-1} frequency utilized on TCS. Based on the empirical TCS scaling, given in Eq. (4.1) of $n_{em}(10^{20}\ m^{-3}) = 0.01B_\omega(mT)/(\omega r_s^2)^{1/2}$, STX-HF would produce peak plasma densities of $n_{em} = 1\times10^{20}$ m^{-3}. This was about what was measured. At compressed external fields of B_e = 40 mT, this results in ζ values of about unity, so STX-HF would be expected to operate in the fully penetrated regime, which is also what was observed. Thus, the physics is very different than what we have described in Section 2 as our 'standard' model of RMF current drive in flux confined FRCs.

The measured internal magnetic field profile on STX-HF is shown by the solid data points on Fig. 3-14. The dashed line is a simple RR profile, while the solid line is an adjusted RR profile of the form

$$B_z = (B_e - B_\alpha)\tanh Ku + B_\alpha \qquad [3.4]$$

with $u = (r/R)^2-1$ and K taken as 1.0. The external magnetic field can exceed the internal field $|B_i| = B_e \tanh K$ by an even greater amount than that given by the RR value due to two effects. The internal pressure p(0) may be higher than the RR value (and perhaps greater than the separatrix pressure), and the centrifugal pressure may be significant. As discussed in Section 2.3, the change between B_e and $|B_i|$ due to centrifugal pressure can be expressed as $\Delta B = 2B_\alpha = 0.5\langle n\rangle m_i(\omega_i r_s)^2/(B_e/\mu_o)$. If we assume synchronous rotation, then $B_e/\mu_o \approx 0.25\langle n\rangle e\omega r_s^2$, yielding $B_\alpha = (m_i/e)\alpha^2\omega$, where $\alpha = \omega_i/\omega$. For the deuterium + helium fill, this yields $B_\alpha \approx 75\alpha^2$ mT. The measured α was about 0.13, which would result in B_α only about 1.3 mT, while the data agrees better with a B_α value of 1.8 mT. This is within the accuracy of the field measurement as well as the estimation of the helium content of the plasma.

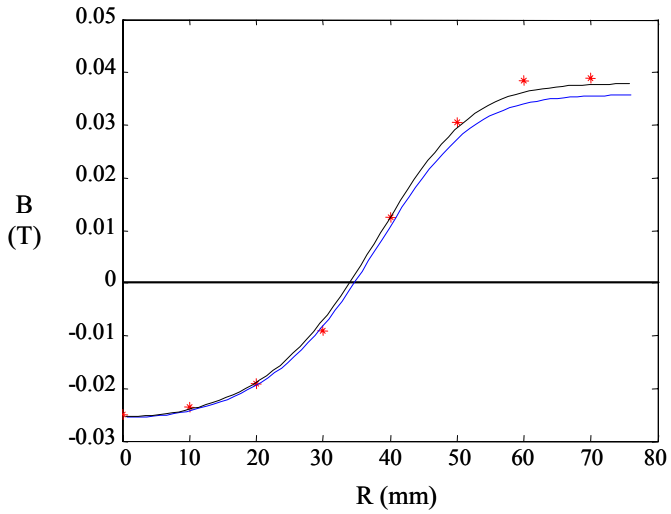

Figure 3-14. Measured $B_z(r)$ profiles (diamonds). The dashed curve is a simple RR profile, while the solid line has a B_α correction as given by Eq. (3-4)

The total temperature given by pressure balance is about T_t = 40 eV. The ion temperature and rotational velocity were evaluated by observing the broadening and Doppler shift of the HeII 468.6 nm line. The ion temperature was about 15 eV, and the electron temperature about 25 eV, which agreed with Langmuir probe measurements (although the probe tended to arc for $T_e > 20$ eV). Helium gas was puffed into the RMF section a few msec prior to plasma initiation at a level to comprise roughly 25 to 35 % of the total ion inventory when ionized. The helium was rapidly ionized as the FRC was generated. The presence of this additional source of plasma shortened the formation time from ~100 μsec to ~ 50 μsec, and increased the peak magnetic field by roughly 60%. The helium was not replaced during the discharge and the driven current decreased back to what could be sustained in steady state with the MCAS plasma source alone. Thus, the density with the MCAS source alone was probably less than could have been sustained by the RMF in normal, partially penetrated operation, since the full penetration torque is much lower than maximally possible.. Limiting the available particles is one way of reaching $\zeta = 1$ and full RMF penetration. The other, of course, would be to increase the plasma temperature for a given, resistivity limited density.

One strange effect of operating in this manner with the limited, MCAS supplied plasma flow, was that the ions were not spun up by the RMF. In fact, they rotated in the opposite direction, at nearly their normal diamagnetic drift velocity, $4KkT_i/eB_er_s^2$ for the RR distribution. This is shown in Fig. 3-15. The ion rotational speed appears to be approximately rigid rotor with an α value of –0.13 (indicated by the dashed line). Since there was very little plasma or neutral gas outside the FRC separatrix, the only mechanism that could accomplish this appears to be shorting out of the radial electric field that would be required to contain the ions if they didn't carry their own current or, even worse, were forced to flow in the paramagnetic direction by the RMF.

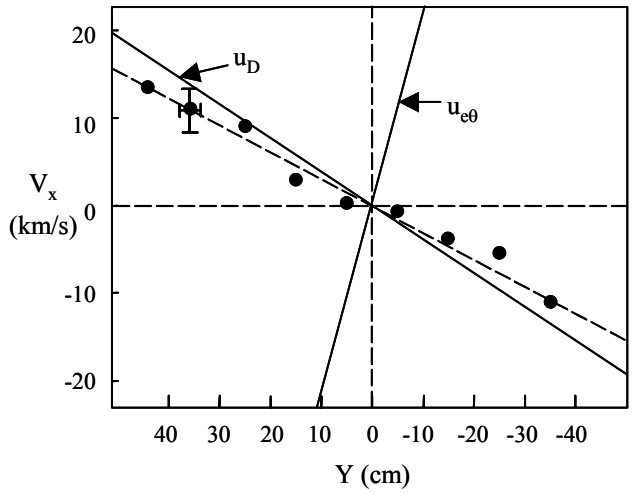

Figure 3-15. Plasma rotation obtained from the Doppler shift of the HEII line. The solid lines represent values corresponding to the ion diamagnetic drift velocity and the synchronous

The global plasma resistivity was estimated as $\eta_\perp = 40$ μΩ-m from the power loading of the antenna and integrating j^2 over the FRC volume. This is considerably lower than seen on TCS, which is either due to the higher electron density, or to the fully penetrated mode of operation. Although the value of B_r/B_z is high throughout the plasma when the RMF fully penetrates, the generated torque is lower and the process may be steadier, without requiring strong radial flows to maintain drive on the inner field lines. However, the fact that particles are being trapped for longer then $\tau_N \sim \mu_o r_s^2/16\eta_\perp \sim 5$ μsec indicates that the RMF is confining plasma in the normal RMF manner. A particle confinement time of $\tau_N \sim 120$ μsec was estimated from the ratio of plasma inventory to the flow rate supplied by the MCAS. Strong confinement effects were seen even before the axial field was reversed, which is probably necessary to even allow FRC formation to be initiated.

The results described in this section indicate that it is possible to prevent ion spin-up in fully penetrated plasmas by shorting out the radial electric field, but we have no intention of trying to operate in this manner on TCS. Such electric field shorting is probably undesirable since it implies effectively open field lines. It is hard to imagine good electron thermal insulation when operating in this manner. We do intend, however, to make use of the MCAS to supply plasma in a controlled manner to the TCS FRCs when we operate in a manner to restrict the neutral background. MCAS may also find use in providing the preionization for start-up, without requiring use of LSX/mod.

IV. RMF START-UP EXPERIMENTS

4.1 Basic Operation & Operational Space

All RMF start-up discharges were preceded by a puff of D_2 from the LSX/mod upstream puff fill valves, which filled the TCS chamber to an atom number density about equal to or less than the final FRC electron density. This generally occurred 200 msec before the RMF discharge was initiated. Seven and one-half msec before RMF initiation a second short puff was introduced into LSX/mod and its coils were rung to send down a pulse of preionized gas, resulting in a measured average electron density of about 10^{18} m^{-3} in TCS before RMF application. Typical data traces are shown in Fig. 4-1 for an intermediate RMF frequency. The RMF antenna current is shown for one antenna pair. For the antenna location at r_a = 54 cm, the vacuum RMF field is related to the antenna current by B_ω(mT) = 0.64I_{ant}(kA).

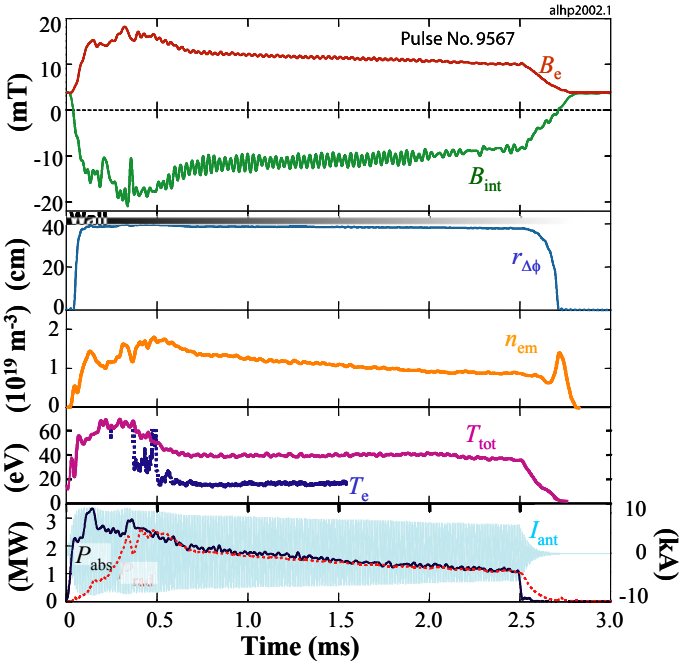

Figure 4-1. Basic measurements for RMF formation of an FRC. $\omega = 0.72 \times 10^6$ s^{-1}, B_ω (mT) = 0.64I_{ant} (kA)

Although the excluded flux traces shown can only be produced by an FRC, we have measured the profile of the on-axis axial field $B_z(0,z)$ using an internal magnetic probe inserted from the end of the TCS chamber. This is shown on Fig. 4-2 along with $B_z(0,z)$ in vacuum. The external magnetic fields measured by two external magnetic loops located at the midplane and the end region are also indicated. It can be seen that the separatrix location z_s is well defined (central axial field B_z changes sign), and is away from the end cone, whose location is indicated in the figure.

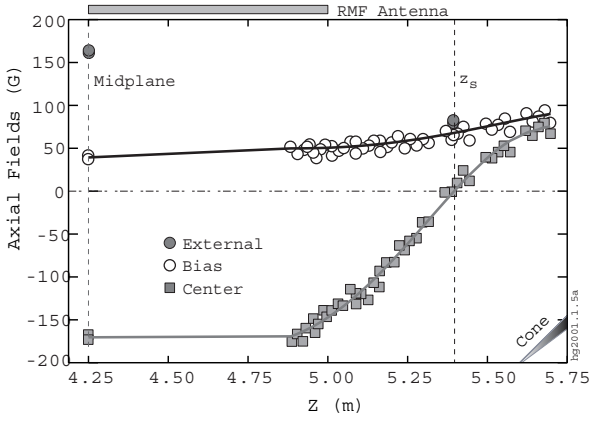

Figure 4-2. Axial profile of the axial magnetic fields at r = 0 (solid squares), and the external fields at two positions (solid circles), for a series of repeatable discharges. The initial axial bias field profile prior to the onset of a discharge (open circles) is also shown. The positions of the

Experiments were also run varying the phase between the horizontal and

vertical antenna currents. The effect of varying phase delays is shown in Fig. 4-3. The data was taken during the steady phase of the discharge for shots with otherwise identical conditions. Best performance was achieved for a 90° phase separation, as expected, but the peak is fairly broad making precise phase control unnecessary. Some current is even produced for zero phase shift as recently demonstrated by Xu *et al*,[15] but many non-simple effects could account for this. The power deposited to the plasma, P_{abs}, is also shown. There is little variation for the phase between 0 and 180°, but the absorption is greatly reduced for the RMF rotation in the 'wrong' direction, presumably due to poor penetration. The derived energy confinement time is also shown, and displays the same peak near a phase separation of 90º.

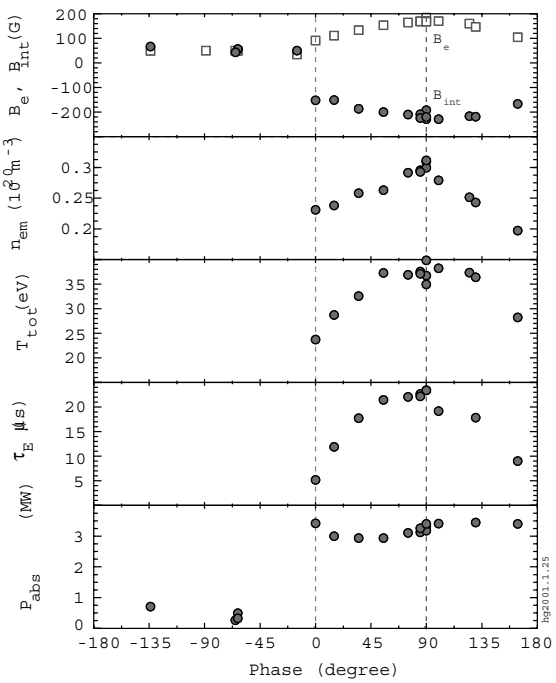

Figure 4-3. Effect of phase shift between horizontal and vertical oscillating

The initial bias field B_o was chosen to yield an FRC with its separatrix close to the plasma tube wall, r_w. If the bias field was too low for the RMF B_ω, r_s would exceed r_w. Likewise, if it was too large either an FRC could not be formed, or r_s would be enough less than r_w that an n=1 or n=2 instability, or other unstable behavior, might develop. This behavior is illustrated in Fig. 4-4, where the optimum bias field was about 60 G. There was always a reasonable range about this optimum where similar behavior could be obtained, and the bias field was easily chosen based on operating experience.

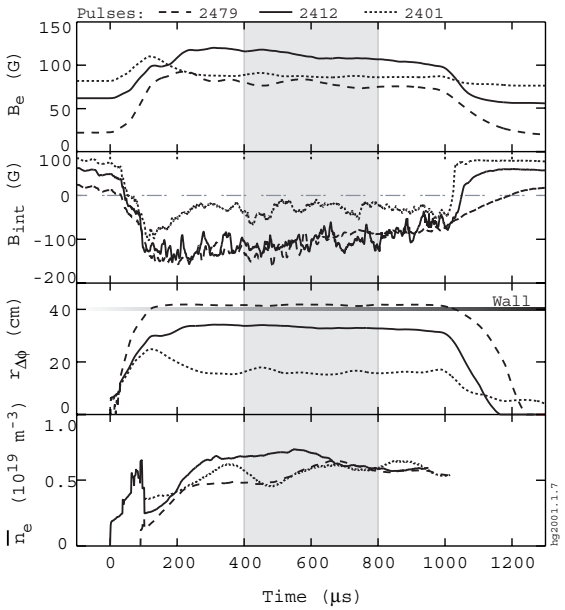

Figure 4-4. Time traces of midplane quantities for three comparable discharges with different initial bias fields. The

One other control was important in some cases. It was always desirable to have the vacuum magnetic field increase slightly at the ends of TCS to prevent axial motion of the FRC. In some cases, especially at higher RMF frequencies, performance was sensitive to the increase in vacuum end field not being too high. The exact reasons for this are not understood, but it was always easy to achieve good performance.

The data shown in Figs. 4-2 - 4-4 were obtained during initial operation at frequencies of $\omega = 0.5$ and 1.0×10^6 s^{-1} , and were previously published.[11] Almost all the following data in this section were obtained using copper straps wrapped around the quartz tube at a radius of $r_c = 41$-cm. This addition was made in the last year of the grant period in an attempt to reduce plasma contact with the quartz tube walls. The straps had an L/R time of 4-msec, about the same as the main TSC coil quarter cycle time. The external flux was bled in in such a way that the total flux inside the straps remained roughly constant during the RMF discharge. This prevented the separatrix radius from reaching the plasma tube wall at $r_w = 40$-cm. The optimal results were not significantly better than obtained earlier without the straps, but the reproducibility and resistance to radial distortions were much improved. A smaller bias field B_o of approximately one-fifth of the final achievable external field, B_e, was generally used. If the copper straps were ideal flux conservers that would produce relative separatrix radii $x_s \equiv r_s/r_c$ values of about 0.9 based on the relationship $B_e = B_o/(1-x_s^2)$. For all experiments shown here the FRC separatrix radius was always between 37 and 39 cm. The radius could be made smaller by starting with a higher bias field but, due to RMF induced plasma rotation, this generally resulted in an n=2 rotational distortion which, while non-destructive, made data interpretation more difficult.

The traces on Fig. 4-1 show the internal and external magnetic fields starting at a bias level of 4 mT. Upon application of the RMF the external field increases to about 17 mT, while the internal field is reversed to about the same magnitude. The excluded flux radius is measured using diamagnetic loops; $r_{\Delta\phi} = (\Delta\phi/\pi B_e)^{1/2}$. This was always equal, within an experimental accuracy of ±1 cm, to the separatrix radius, r_s, as determined from a thin Be-O tube containing an array of (31) internal magnetic pickup loops, inserted radially into the FRC. The B_{int} trace on Fig. 4-1 came from a loop at $r = 0$, while the B_e trace was from a loop at $r = 39$-cm. The excluded flux radius was roughly constant over most of the 1.6-m length of the RMF antennas, with a typical separatrix length of $\ell_s \sim 2$ m as defined by where $r_{\Delta\phi}$ is reduced to half its midplane value (slightly shorter than the measured X-point). (Somewhat surprisingly, neither this separatrix length nor the overall performance changed much for a few discharges run with shortened, 1-m long RMF antennas. See Section 4.11.)

The peak electron density shown in Fig. 4-1 is calculated from the 2-pass interferometer trace as $n_{em} = \int n_e d\ell/4\langle\beta\rangle r_s$ where $\langle\beta\rangle = 1 - 0.5x_s^2$. This data reduction methodology may slightly underestimate the peak density when the density profile is highly peaked. The interferometer accuracy is about 0.005 fringes which, for the 10.6 μ CO_2 laser wavelength, corresponds to an $\int n_e d\ell$ value of 1.0×10^{18} m^{-2}. Most of the density data was taken for 1.5 msec discharges since magnet firing induced interferometer vibration became a problem for longer times.

The total plasma temperature T_t is calculated as $(B_e^2 + 2B_\omega^2)/2\mu_o k n_{em}$ based on the observation that the RMF B_θ is about equal to $2B_\omega$ when the RMF only partially penetrates into the FRC, which is the desired mode of operation. This RMF pressure rotates around the separatrix, producing some fluctuations in the internal magnetic field. The electron temperature shown in the figure was measured on several identical shots

using a double Langmuir probe at r = 37 cm using various bias voltages. It has not yet been possible to make an accurate swept probe measurement on a single shot due to the pick-up from the RMF.

The power absorbed from the RMF is measured by a careful integration of the product of antenna voltage and current over a cycle, with the leads to the digitizers carefully adjusted so that a zero value is registered for vacuum shots, other than due to charging the tank circuit during the first 100 μsec. At several MW input levels this measurement is accurate to about 5% based on observed variations for vacuum shots. The radiated power is calculated from the average of two bolometers viewing across the mid-plane diameter, $\int p_r d\ell$, as $P_{rad} = \pi k_r r_s \ell_s (\int p_r d\ell)/2$ where k_r is a correction factor for bolometer response that is somewhat above unity at low temperatures. This, of course, assumes that the radiation is both axially and radially uniform. Impurities concentrated near the separatrix would make this value an underestimate but, judging from the near equality with the absorbed power for all but very low density cases, this is probably not the case.

The behavior seen in Fig. 4-1 where the temperature increases rapidly, but then decays to a lower value as the radiated power increases, is typical of all shots. It becomes even more pronounced at high frequencies where the electron density is lower and the initial temperature is higher. The electron temperature becomes pegged near 15 eV, independent of input power, by a strong radiation barrier. It appears that the electron and ion temperatures are about equal. Results obtained with a 25% CO_2 doping, and even in pure CO_2 are not much different from those for pure D_2 discharges, except for the absence of the strong initial temperature increase, and a more rapid build-up of radiated power. It seems that impurities adsorbed on the untreated quartz tube walls rapidly find their way into the FRC. After a prolonged vacuum opening it may take up to a full day of running to achieve optimal results, so very dirty walls are even worse than operation in pure CO_2. Most of the scaling data we present here is for times near 0.5 msec (peak of B_e signal) and at 1.0 msec.

Initial experiments without the straps were run at a frequency of $\omega = 1.0 \times 10^6$ s^{-1} using a set of home-made cylindrical capacitors in the RMF tank circuit. It was desired to decrease this value in order to increase ζ to allow for more efficient current drive with deeper RMF penetration, and ten low loss 0.23 μf capacitors capable of intense ringing operation were then obtained. Use of all ten allowed us to run at a frequency of $\omega = 0.52 \times 10^6$ s^{-1}, with higher frequencies obtainable by using fewer tank capacitors. The initial $\omega = 1.0 \times 10^6$ s^{-1} and 0.52×10^6 s^{-1} results were reported in Ref. 11. However, effective diffusivities, or resistivities, were based on simple scaling assuming a fixed value of $(\gamma/\lambda)_{req} = 1/\sqrt{2}$ rather than the more accurate scaling discussed in Section 2.1. We now use effective resistivities calculated based on power absorption measurements.

Experiments with external flux straps were run over a wide range of ω and B_ω. The frequencies are necessarily discrete since they were chosen by changing the number of tuning capacitors in the RMF antenna tuned circuit. The range of λ and ζ seen in the experiments is shown on Fig. 4-5 for ω = 0.52, 0.72, 0.92, and 1.62×10^6 s^{-1}. The highest

frequency results were obtained using only one of the ten available tuning capacitors. The achievable values of B_ω at high frequency were restricted by the high value of antenna inductive impedance, $\omega L_{ant.}$ The antenna impedance will be reduced in the future by either splitting the antennas into two parallel sections or using a shorter length antenna.

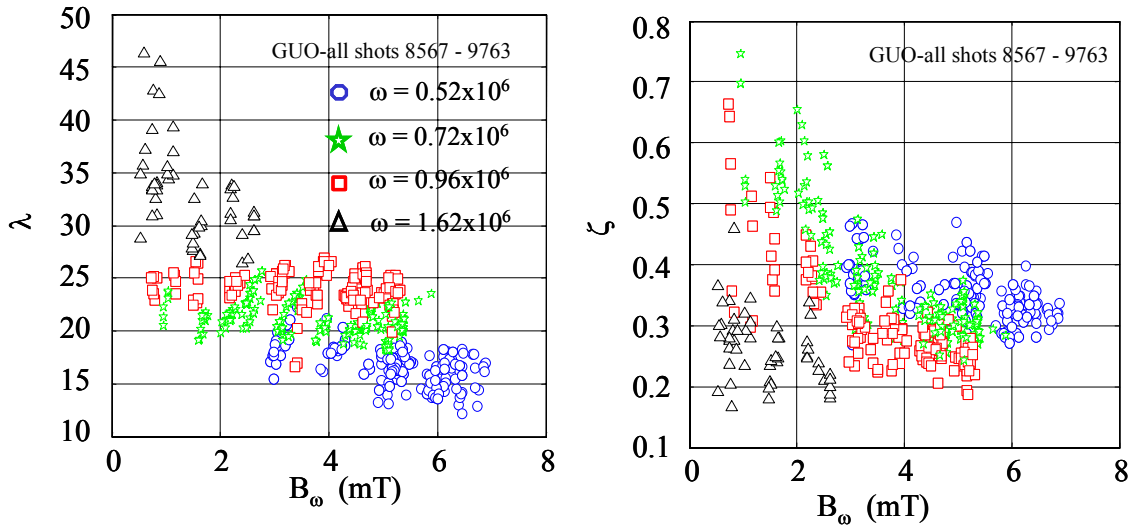

Figure 4-5. Experimental range of λ and ζ

4.2 Power Absorption & Resistivity

Resistivity measurements based on the absorbed power (calculated as outlined in Sec. 2.1) are shown in Fig. 4-6. The data is plotted versus the ratio B_e/B_ω since this gave the best correlation over the range of experiments. The ratio varied by over a factor of three for reasons which will become evident. Two data points are shown for each discharge, one near the peak value of B_e (at about 0.5 msec), and one for the very steady conditions at 1.0 msec.

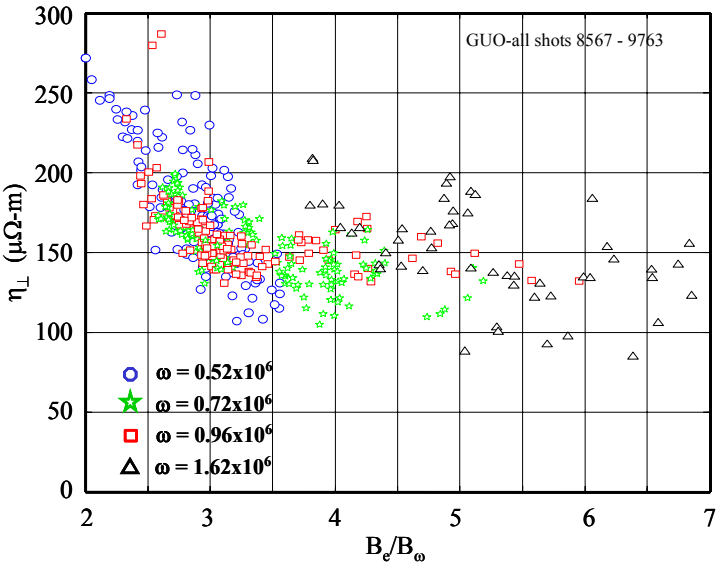

Figure 4-6. Resistivity measurements based on absorbed

Over the range of experiments, with $B_e/B_\omega < 3$, the resistivity appears to scale as $\eta_\perp \propto (B_\omega/B_e)^2$, which indicates that the RMF drive process itself is responsible for high effective resistivity when B_ω is a significant fraction of B_e.

The initial data with external flux rings was taken at the lowest, $\omega = 0.52\text{x}10^6$ s^{-1} frequency where most of the results presented in Ref. 11 were obtained, and then extended to higher frequencies. The investigations were extended to higher values of B_e/B_ω for the higher frequency cases by operating at lower values of B_ω. In that case the deleterious effect of the RMF drive started to disappear and the resistivity approached the basic resistivity of low density non-driven FRCs. For LSX and other FRTPs at several times 10^{21} m^{-3} densities, the non-driven resistivity scaled as $\eta_\perp \approx 19/n_e^{1/2}(10^{20}\ \text{m}^{-3})$ μΩ-m.[16] At lower 10^{19}-10^{20} m^{-3} densities achieved in translation and expansion experiments on the Osaka FIX device[17] and in TCS, effective resistivities less than one-half this scaling value were seen. The highest B_e/B_ω ratios in the TCS RMF formation experiments were reached at low values of $B_\omega \sim 1$ mT, and densities of ~10^{18} m^{-3}, so that the lowest resistivities shown in Fig. 4-6 are consistent with the non-driven FRC results. It is not known why the highest frequency results have so much scatter, but the high frequency results generally tend to deviate more from the analytic results. That is why specific calculations were carried out for $\omega = 1.6\text{x}10^6$ s^{-1}. Some of the deviations may be due to the low power operation, where the measured absorbed power may be in error, and to the low density operation, where the $\int n_e d\ell$ measurements are barely above instrument resolution, but may also reflect deviations from the simple uniform $\eta_\perp$ model at very low values of ζ.

4.3 Density Scaling

For our experiments Eq. (2-15) is representative of the numerically calculated density scaling. Measured densities, as shown in Fig. 4-7, scale approximately as $n_e \sim B_\omega/\omega^{1/2}$, which is indicated by the dashed lines. The lack of dependence on the ratio B_e/B_ω (a dependence implicit in the Eq. 2.15 ζ dependence) implies a resistivity scaling of $\eta_\perp \sim (B_\omega/B_e)^{1.16}$. A reasonable fit to the Fig. 4-6 data over the range $3 < B_e/B_\omega < 7$ is $\eta_\perp = 570(B_\omega/B_e)^{1.16}$ μΩ-m. Taking $\langle\beta\rangle$ as 0.6, this yields an approximate density scaling of $n_{em}(10^{20}\ \text{m}^{-3}) = 0.008B_\omega(\text{mT})/(\omega r_s^2)^{0.42}$. Since all the experiments have r_s values within ±0.01 m of 0.38 m, the $n_{em}(10^{20}\ \text{m}^{-3}) = 0.026B_\omega(\text{mT})/\omega^{1/2}(10^6\ \text{s}^{-1})$ scaling indicated by the dashed lines on Fig. 4-7 represents an empirical density scaling of

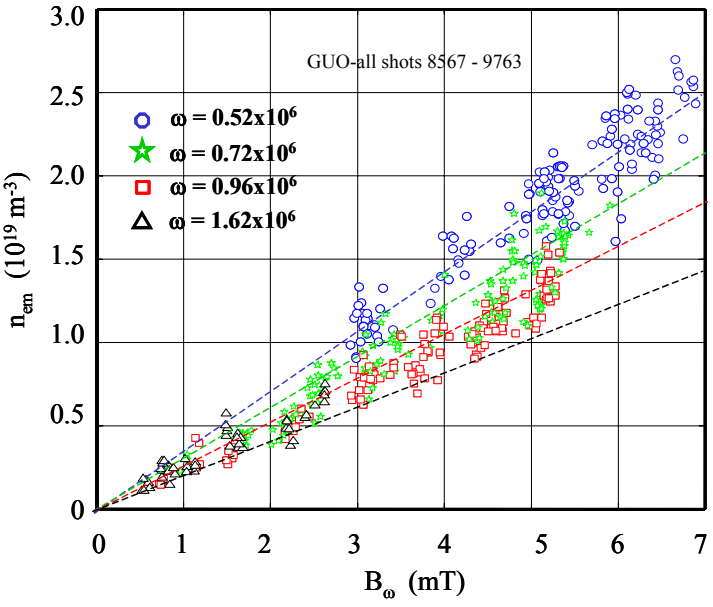

Figure 4-7. FRC peak density as a function of RMF magnitude. Dashed lines are for $n_{em} =$

$$n_{em}\left(10^{20}\,\mathrm{m}^{-3}\right) = \frac{0.01B_{\omega}(\mathrm{mT})}{\left(\omega r_s^2\right)^{1/2}} \quad . \qquad [4.1]$$

The Eq. (4-1) scaling is in rough agreement with the numerical scaling using absorbed power inferences of plasma resistivity, but is about 25% higher in absolute magnitude. That is part of the reason resistivities calculated from such scaling in Ref. 11 were lower than those shown here. Either the plasma resistivity is actually lower than shown in Fig. 4-6, and non-steady behavior causes the absorbed power to be higher than calculated using Eqs. (2.16) and (2.17), or our numerical modeling is not completely accurate. We would expect that three-dimensional effects ignored in the modeling, especially the FRC length being greater than the antenna length, would cause Eq. (2.15) to be an overestimate of the achievable density. The very high frequency data seems to deviate even more strongly from the analytical scaling. This could be due to systematic interferometer errors, such as caused by a layer of plasma at the ports for the interferometer windows. Another strong possibility is that the resistivity is higher at the plasma edge, making the power absorption high, but low elsewhere, requiring less RMF torque to balance the overall resistive friction. This effect would be especially important for the low ζ high frequency operation.

Given the observed density scaling, it is now clear why the value of B_e/B_ω varies so much in Fig. 4-6, and why it is larger at lower values of B_ω. The external field B_e is equal to $(2\mu_o n_{em} k T_t)^{1/2}$, and the temperature would also have to increase linearly with B_ω for B_e/B_ω to remain constant. However, the electron temperature is pegged near a low value due to radiation barriers, so B_e/B_ω decreases as B_ω is increased. For given $\eta_\perp$, B_ω, $r_{c,}$, and ω, only the density is determined by force balance. Higher temperatures and external fields could be achieved with the same RMF parameters and plasma resistivity, if allowed by power balance, since both T'_{RMF} and T'_η would increase as the temperature (and $\Delta r/r_s$ and ζ) rose. Of course, the absorbed power would also increase as the current increased, but this would be mitigated by lower values of B_ω/B_e and thus lower $\eta_\perp$.

As a further test of our basic modeling, the achieved ratio of B_e/B_ω can be plotted as a function of the scaling parameter given in Eq. (2.13), using the values of $\eta_\perp$, and thus $\lambda_{,}$ obtained from the absorbed power. The results of this exercise are shown in Fig. 4-8. The correlation is again good except at the highest frequency. This deviation could be due to lower average resistivities than

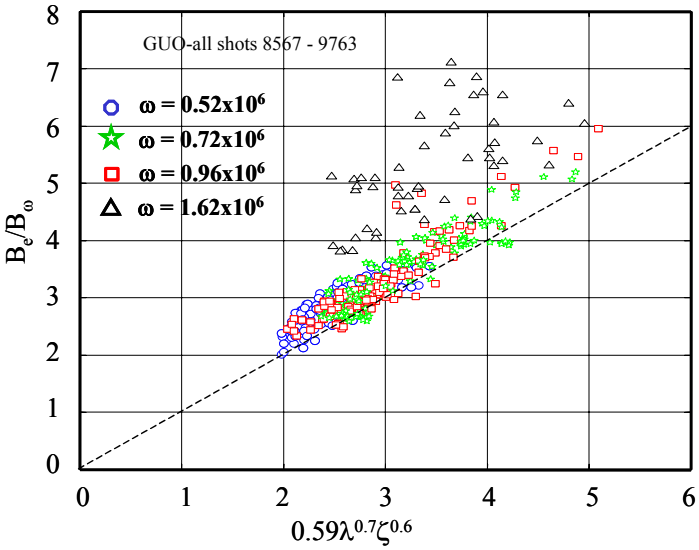

Figure 4-8. Measured field ratio versus calculated scaling parameter.

calculated using Eqs. (2.16) and (2.17) (making λ larger), or lower densities than calculated from the 2-pass interferometer measurements (making ζ larger).

4.4 High Frequency Operation

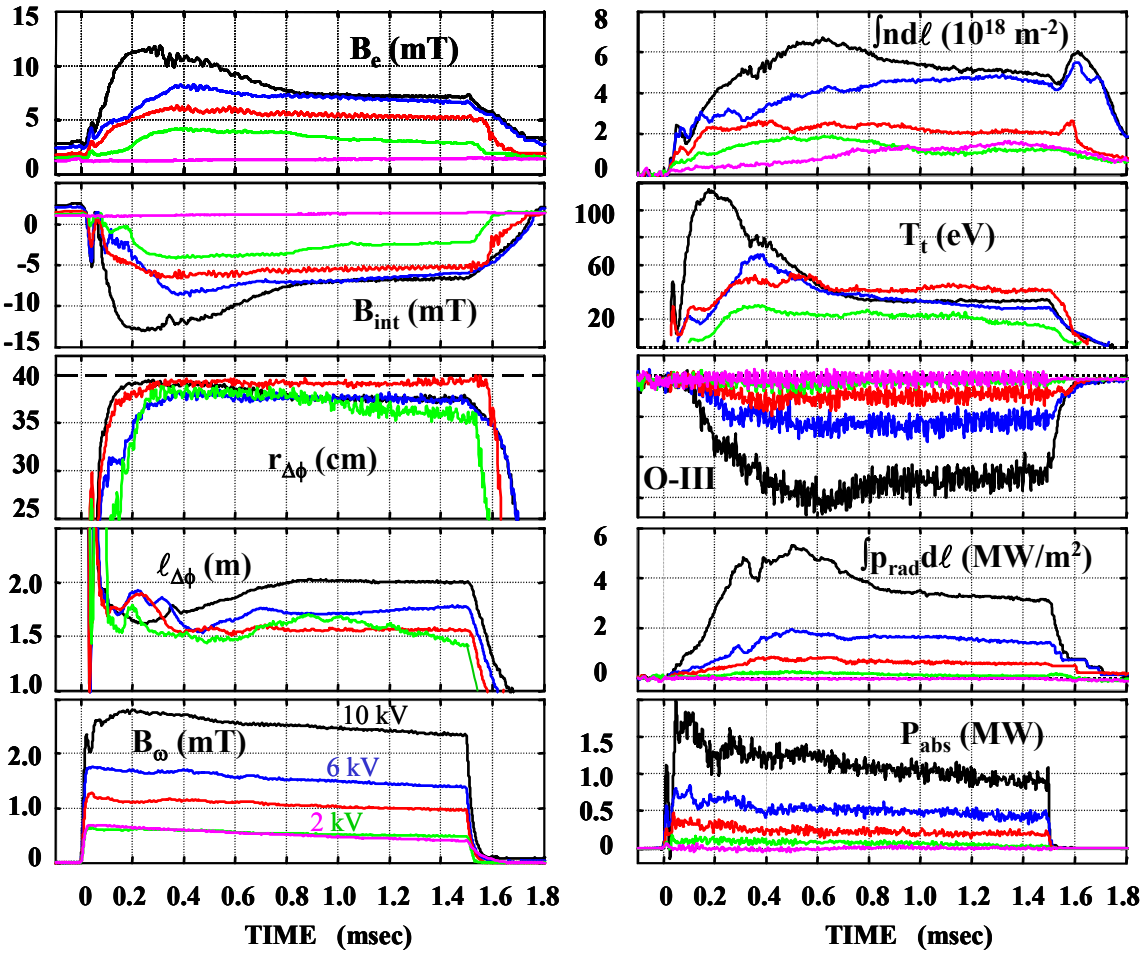

Figure 4-9. High frequency, ω =1.6x10^6 s^{-1} data taken at RMF charging voltages of 10, 6, 4, and 2 kV. A second shot at 2 kV is shown for reference where the initial fill pressure was set too low for an RMF discharge to occur. The measured density there is

With the above aforementioned caveats on measurement errors, it is worth looking at some of the high frequency discharge time histories since they illustrate some important features with regard to temperature histories. Examples are shown in Fig. 4-9 for four different RMF pulser voltages. One shot at the lowest voltage, where the initial fill pressure was set too low to achieve breakdown, is also shown. In accordance with Eq. (4.1) the measured line densities are very low (barely above instrument resolution for the lowest RMF magnitude). However, the absorbed power was still relatively high. This allowed higher temperatures to be transiently reached for the highest RMF amplitude before rapid impurity ingestion again pegged the electron temperature. The radiated power is seen to rise on a rapid several 100 μsec timescale, although this is partially due

to an increasing density. Radiation from a doubly ionized oxygen line is also shown for comparison. It was noted in all experiments that the radiated power correlated well with this line.

In accordance with Eq. (2.11), the final low equilibrium temperatures resulted in the low ζ values shown on Fig. 4-5. At high λ and low ζ we might expect the RMF induced axial currents to be more concentrated near the separatrix, and even to see some greater concentration of the azimuthal currents in that location. The internal field traces showed lower fluctuation levels for this high ω condition, but that was also a general tendency at all frequencies as B_ω/B_e decreased. We will not be able to resolve the discrepancies between the high and low frequency results until we change the RMF antenna configuration to allow larger values of B_ω to be produced at high RMF frequencies.

One favorable tendency seen in the highest RMF power traces in Fig. 4-9 is the scaling of average resistivity implied by the $\eta_\perp \propto P_{abs}/B_e^2$ relationship. This ratio is much lower at early times when B_e (and B_e/B_ω) is higher, with T_t higher and n_e lower.

One final note should be made about the numerical scaling represented by $B_e/B_\omega \propto \lambda\zeta/(\gamma/\lambda)_{req}$ and $(\gamma/\lambda)_{req} = 0.85\langle\beta\rangle\lambda^{0.3}\zeta^{0.4}$. The less than linear scaling with λ, and hence with $\eta_\perp^{-1/2}$, would seem to imply that current drive is *relatively* less efficient as λ increases, when it actually means that at low λ the current drive, although becoming overall poorer, is somewhat augmented by high resistivity allowing greater penetration than would be possible due to synchronous electron rotation alone. At high λ the above scaling will no longer apply and $(\gamma/\lambda)_{req}$ will tend to approach a fixed value of about 1.25. It is a basic tenet of RMF current drive theory that current drive becomes more efficient at lower plasma resistivity (higher λ) due to the ability to better drive the outer electrons into near synchronous rotation.[6]

4.5 Pressure and Magnetic Field profiles

The magnetic field profiles $B_z(r)$ and $B_\theta(r)$ can be determined from the internal probe data assuming that the B_x data represents B_θ. The contribution due to B_θ can even be determined when the probes are placed at a 45° angle to the tube centerline since B_θ will have a frequency equal to the RMF frequency. However, as discussed in Section 2.3, the pressure profile will also depend on the ion rotation. The data reduction is straightforward if both the temperature and ω_i are assumed uniform.

Typical profiles of B_z and B_θ are shown in Fig. 4-10. A low-pass filter with a cutoff frequency of 10 kHz (roughly equivalent to time averaging over 100 μsec) has been applied to the B_z signal in this figure. Without filtering, the B_z signal has a high fluctuation level, indicating that the plasma is turbulent or the RMF is inducing many waves. The effect of filtering is illustrated in Figure 4-11, which shows both filtered and unfiltered signals at $r = 0$, 0.2, 0.3, and 0.4 m as a function of time. A 10 kHz low-pass filter was chosen to be consistent with the B_x signal. B_x is separated from the B_z signal using a notch filter between $f_{rmf} \pm 10$ kHz, and thus its envelope has a 10 kHz bandwidth.

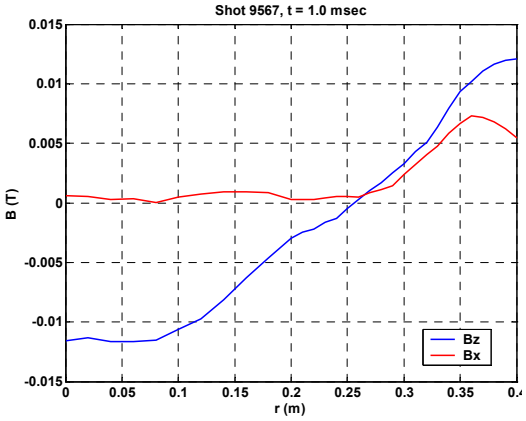

Figure 4-10. Typical radial magnetic field profiles with $\omega = 0.72 \times 10^6$ s^{-1}

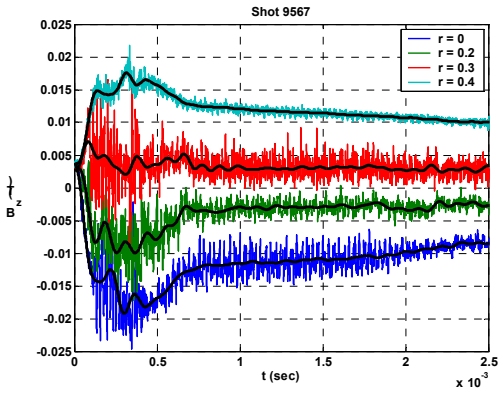

Figure 4-11. Four B_z signals as a function of time without filtering, and with a 10 kHz low pass filter

In the previous sections we have evaluated the peak density by assuming that $n_{em} = \langle n_e \rangle / \langle \beta \rangle$ with $\langle \beta \rangle$ given by $1 - 0.5x_s^2$. We have then calculated the total temperature from $T_t = (B_e^2 + 2B_\omega^2)/n_{em}kT_t$. Although these are good approximations that can be used when internal field and rotation data are not available, they contain several errors. The interferometrically measured density is a line density and it is only an approximation to divide it by an area weighted density. The RMF contribution to the radial pressure is only approximately B_ω^2/μ_o. The centrifugal forces will subtract from the peak pressure as discussed in Section 2.3. Although these errors may be on the same order as assuming the temperature is uniform, we will evaluate them below for a particular case where there are both internal field and rotation measurements.

The internal magnetic field profiles can be combined with the radial pressure balance equation

$$p + \frac{B_z^2}{2\mu_o} + \int_0^r \langle j_z B_\theta \rangle dr - \int_0^r \rho r \omega_i^2 dr = \text{const} \qquad [4.2]$$

to estimate the radial plasma pressure profile. Before this expression can be evaluated, we must estimate $\langle j_z B_\theta \rangle$, where j_z is the induced axial current in the plasma and B_θ is the θ-component of the RMF field. $\langle j_z B_\theta \rangle$ is evaluated by taking the time average of the instantaneous value of $j_z B_\theta$ over one RMF cycle. The 2nd term in $j_z = \frac{1}{\mu_o}\left(\frac{1}{r}\frac{\partial}{\partial r}(rB_\theta) - \frac{1}{r}\frac{\partial B_r}{\partial \theta}\right)$ is neglected because B_r is much smaller than B_θ in the outer region where the RMF pressure is large, and the spatial distance over which B_r changes (in the θ-direction) is much larger. It is trivial to integrate the above equation to get a pressure profile for the case with no rotation. The constant on the right-hand-side is specified by assuming that the minimum pressure is small (usually at maximum radius). However, if there is significant rotation, the 4th term on the left-hand-side must be included and this requires a temperature specification so that p and ρ can be related. Or better yet, if $\int n_e d\ell$ is known, the temperature can be solved for simultaneously.

Figure 4-12 shows pressure profiles consistent with the magnetic fields of Figure 4-10. This figure shows a pressure profile for two cases, one where the plasma is assumed to be stationary, and the other where the plasma is assumed to be rotating with $\omega_i = 0.7\text{x}10^5$ s^{-1} (close to the 11 kHz measured for similar conditions). In each case, a self-consistent temperature is also found. It should be noted that we now have three independently derived temperatures:

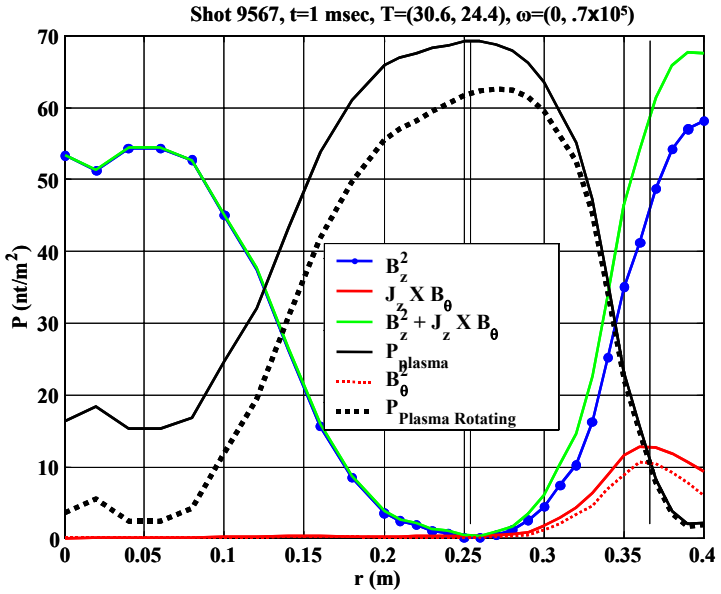

Figure 4-12. Pressure profiles consistent with the magnetic field profiles of Fig. 4-10

1. 39.7 eV derived from assuming pressure balance and assuming that $\int n\,dl \approx 4r_s\langle\beta\rangle n_{em}$, and $p = \frac{B_z^2}{2\mu_o} + \frac{B_\omega^2}{\mu_o}$.
2. 30.6 eV derived using a self-consistent profile with higher n_{em}, assuming no rotation.
3. 24.4 eV derived using a self-consistent profile and a rotation of $0.7\text{x}10^5$ s^{-1}.

The estimated temperature using the *self-consistent* profiles may be a bit low, because our total pressure estimate may be low. Normally we estimate that the RMF contributes an inward radial pressure of $B_\omega^2/2\mu_o$, which is about 17.6 Nt/m^2 for this case. The maximum pressure from the $\int_0^r \langle j_z B_\theta \rangle dr$ is about 12.8 Nt/m^2, and there is reason to believe that this value is low. The RMF produced by a finite radius antenna has a minimum midway between two rods of the same phase, and that is precisely where the magnetic probe is located. We are currently investigating ways to improve upon this measurement. Applying a multiplier to $\int_0^r \langle j_z B_\theta \rangle dr$, so that the peak pressure is $B_\omega^2/2\mu_o$, increases the temperature to 33.0 and 27.0 for the no rotation and $\omega = 0.7\text{x}10^5$ cases respectively; thus there is still a significant discrepancy from the density profile effects alone.

The separatrix radius in Fig. 4-12 is 0.366 m, and $\langle\beta\rangle$ = 0.732 for the non-rotating case, and 0.701 for the rotating case. Here we define $\langle\beta\rangle = \frac{1}{p_{\max}} \int_0^{r_s} prdr$. The implied values of x_s for these two values of $\langle\beta\rangle$ are 0.732, and 0.773 for the non-rotating and

rotating assumptions respectively. For the rotating assumption, the implied coil radius r_s/x_s is 0.473 m, compared with 0.455 from $\Delta\phi$ measurements.

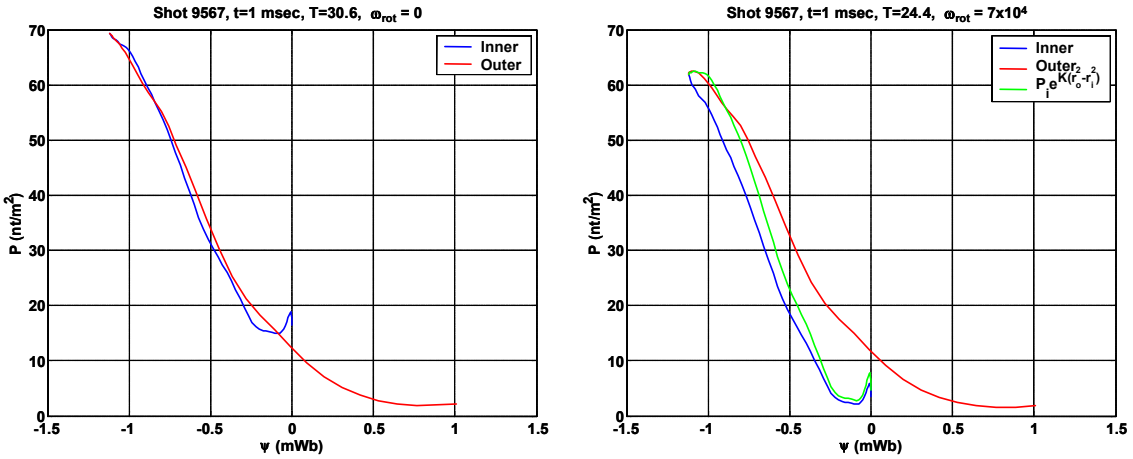

Figure 4-13. Pressure as a function of magnetic flux for a non-rotating and a rotating

Normally it is assumed that the pressure is constant on a flux surface; p = p(ψ). It is straightforward to plot the pressure as a function of the flux surface using the magnetic and pressure profiles which is done in Figure 4-13. For this particular case, we see that the pressure is remarkably well equalized between inner and outer field lines when no rotation is assumed. The addition of rotation destroys this good agreement. The green curve shows the expected outer field line pressure, based on the inner field line pressure using the relationship $p_o = p_i \exp\left\{\frac{m_i\omega^2}{2kT}\left(r_o^2 - r_i^2\right)\right\}$ where p_o is the outer field line pressure and p_i is the inner field line pressure. Possible errors may arise from the center of the plasma tube, which we call $r = 0$, not being precisely aligned with the center of the FRC.

It is instructive to compare the experimentally measured profiles with numerical simulations. Figure 4-14 shows the experimentally measured profiles of Fig. 4-10 superimposed on numerically generated profiles for similar conditions. The main features of the numerically predicted profiles include: 1) the B_z profile tends to flatten near the magnetic field null and; 2) B_θ always penetrates all the way to the field null, as required for current drive. These features are fundamental to our understanding of RMF current drive, and yet they are

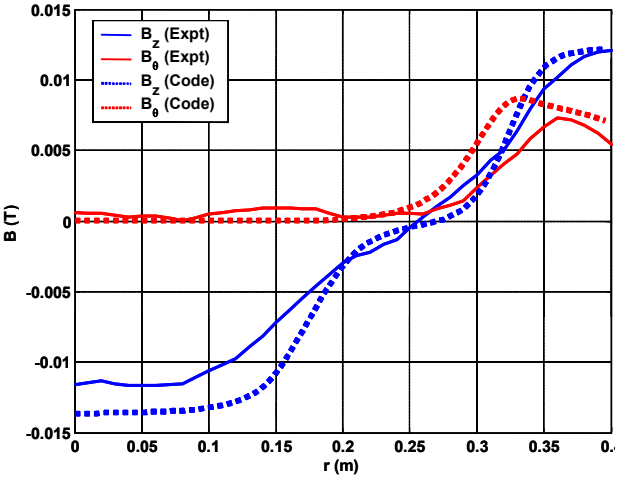

Figure 4-14 Comparison of measured and numerical profiles for similar plasma

not evident in the experimental profiles for shot 9567. A quick look at other experimental shots indicates that shot #9567 is representative of the experimental data with external flux rings, but a thorough analysis of many shots must be performed before any conclusions can be drawn. The MHD code is being modified to include plasma, but preliminary results do not show a strong influence on $B_z(r)$ flattening (current reduction) near the field null. Rather, dp/dr is finite at the null and balances the centrifugal term. Initial results with a non-uniform $\eta_\perp$ based on a Chodura type resistivity[18] can reproduce the profile shown in Fig. 4-14, but so far only with transient FRCs with a decaying poloidal flux.

4.6 Neutral D Measurements

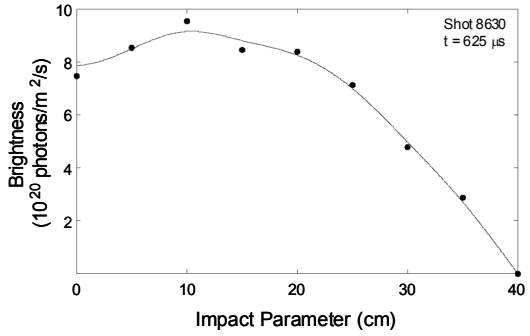

Figure 4-15. D_α brightness profile. Also shown is a smoothing spline fit to the experimental data with the brightness at the

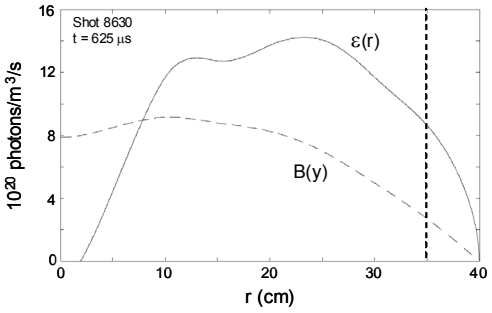

Figure 4-16. Abel inverted D_α emission profile. Solid line: Emission profile. Dashed line: Measured brightness. The impact parameter of

The neutral density profile is calculated from the emission profile of D_α, $\varepsilon(r)$. This emission per unit neutral depends on both the electron density and the excitation rate, so both $n_e(r)$ and $T_e(r)$ are needed. We assume T_e is uniform and equal to one-half T_t. As described in Appendix A.4, TCS has an eight-chord array of absolutely calibrated D_α emission detectors. The first step is Abel inverting the chord-integrated brightness. Assuming axisymmetry, then the chord-integrated brightness B at impact parameter y is given by

$$B(y) = 2\int_y^a \varepsilon(r)\frac{rdr}{\left(r^2 - y^2\right)^{1/2}} \qquad [4.3]$$

where a is the wall radius. Eq. (4.3) is the standard Abel transform. The inverse transform is

$$\varepsilon(r) = -\frac{1}{\pi}\int_r^a \frac{dB}{dy}\,\frac{dy}{\left(y^2 - r^2\right)^{1/2}}. \qquad [4.4]$$

The measured brightness profile B(y) is fit with a smoothing spline with the brightness at the wall forced to zero, as shown in Fig. 4-15. The derivative dB/dy is then computed using center differencing, with a Neumann boundary condition at the geometric axis

$(dB/dy)_{y=0} = 0$. Eq. (4.4) is integrated numerically to give the D_α emission profile, as shown in Fig. 4-16. It should be noted that the profile beyond the outermost chordal measurement (35 cm) is arbitrary and is dependent upon the shape of the spline fit from the last data point to the wall boundary condition.

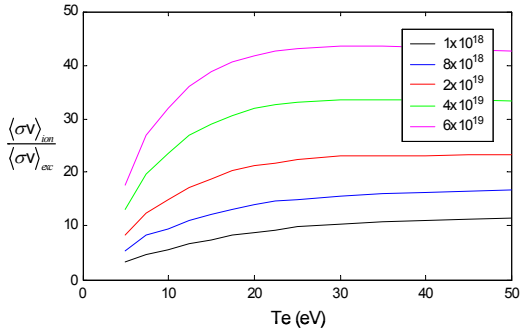

Figure 4-17. Johson-Hinnov Factor. Plotted for various electron densities (m^-

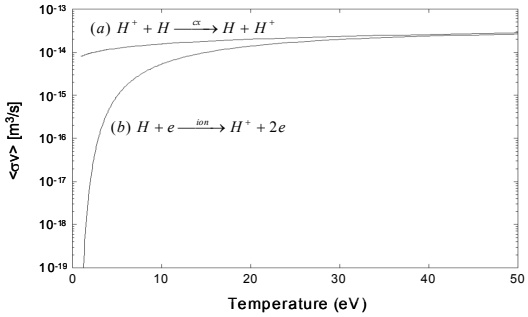

Figure 4-18. Hydrogen Rate Coefficients. (a) $\langle\sigma v\rangle_{cx}$ vs. T_i (b) $\langle\sigma v\rangle_{ion}$ vs. T_e

Assuming that electron-impact excitation is the sole source of Dα emission, then the neutral density can be found from

$$n_0(r) = \frac{\varepsilon(r)}{n_e(r)\langle\sigma v\rangle_{exc}} \qquad [4.5]$$

where n_e is the electron density and $\langle\sigma v\rangle_{exc}$ is the rate coefficient for this particular transition. The TCS plasmas are too dense to be in the coronal regime for D_α and $\langle\sigma v\rangle_{exc}$ is a function of both electron density and electron temperature. The excitation rate coefficient is obtained from the Johnson-Hinnov factor[19] from the ADAS database,[20] relating the ionization rate coefficient to the excitation rate coefficient as shown in Fig. 4-17. The ionization rate coefficient is assumed to be dominated by single-step ionization in the coronal regime, and is solely a function of electron temperature, as shown in Fig. 4-18.

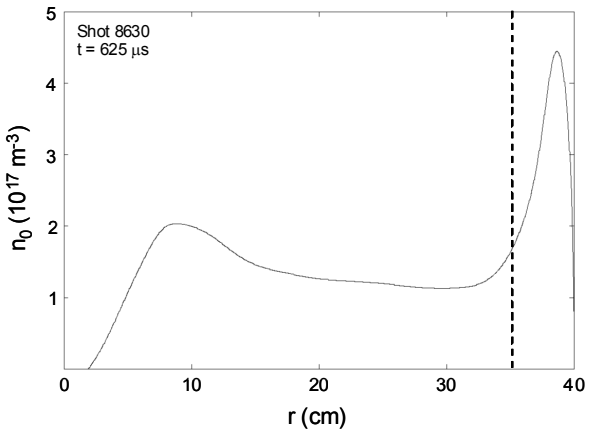

Figure 4-19. Neutral Density Profile. Outermost chord at 35-cm impact parameter

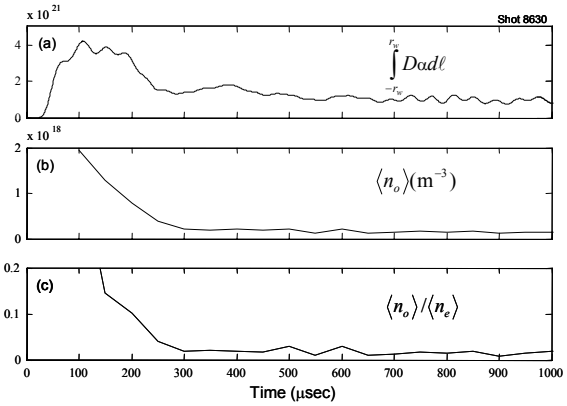

Figure 4-20. Average Neutral Density and Neutral Fraction.

Assuming that the electron temperature is half the total temperature, then Eq. (4.5) can be solved and a typical neutral density profile is shown in Fig. 4-19. The neutral density profile outside of the last viewing chord at 35 cm depends on the slope of the chord-integrated brightness profile dB/dy. In this analysis, the brightness at the wall (40 cm) has been forced to zero and the gradient scale length is 5 cm. In reality, the brightness gradient may be much shorter, raising the edge neutral density. The average neutral density is the area integral to the wall radius r_w is $\langle n_0 \rangle \equiv \frac{2}{r_w^2}\int_0^{r_w} n_0(r) r dr$. The evolution of the average neutral density is shown in Fig. 4-20. Once steady-state is reached, the average neutral density is about $1.5\text{x}10^{17}$ m^{-3}, or less than 2% of the plasma density.

Once the electron and neutral densities are known, the ionization rate, $S_{ion} = n_e n_0 \langle \sigma \mathrm{v} \rangle_{ion}$, and charge exchange rate, $S_{cx} = n_i n_0 \langle \sigma \mathrm{v} \rangle_{cx}$ can be calculated. Assuming that the rate coefficients for hydrogen and deuterium are equal, the ionization rate coefficient for electron-impact ionization of atomic hydrogen from the ground state is shown in Fig. 4-18. The charge exchange rate coefficient is also shown, assuming 1 eV neutrals.[21]

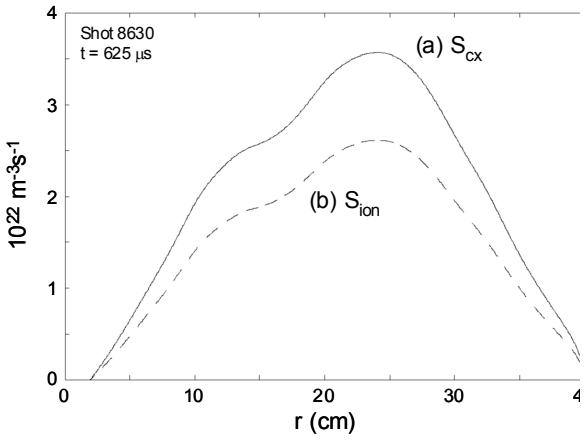

Figure 4-21. Plasma source rate profiles.

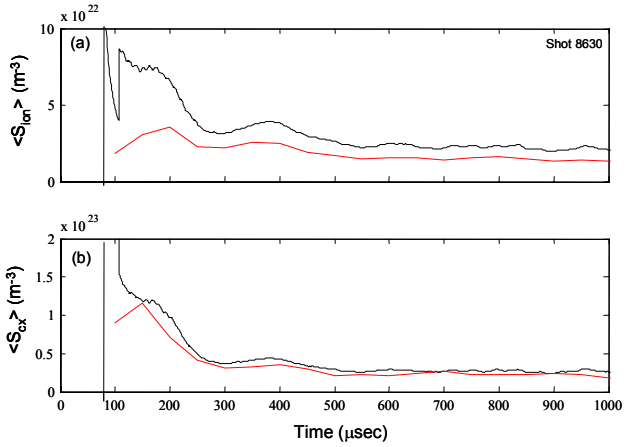

Figure 4-22. Average Source Rates. Black curve: chord integrated value. Red curve: Abel Inverted average. (a) Ionization source rate. (b) Charge-exchange rate.

Assuming axisymmetry, the average source rates are $\langle S_{ion} \rangle \equiv \frac{2}{r_w^2}\int_0^{r_w} S_{ion}(r) r dr$ and $\langle S_{cx} \rangle \equiv \frac{2}{r_w^2}\int_0^{r_w} S_{cxn}(r) r dr$. This definition is probably a lower bound on the source rates. An upper bound, used in a global power balance model is a zero-dimensional estimate taken from the center D_α chord at 0-cm impact parameter with rate coefficients based on the average plasma density. The local source rates are shown in Fig. 4-21, while the average source rates calculated by both methods are shown in Fig. 4-22. The average ionization rate lies between $1.5\text{x}10^{22}$ and $2.5\text{x}10^{22}$ $m^{-3}s^{-1}$, while the charge-exchange rate lies between $3\text{x}10^{22}$ and $5\text{x}10^{22}$ $m^{-3}s^{-1}$.

4.7 Plasma Shape

We could infer information about plasma shape from various cross-tube measurements, such as interferometry, bolometry, and spectroscopy. The tomographic system was used to confirm these inferences and get more details about the FRC structure, at least in the midplane of TCS. As discussed in Section 5, the tomographic system was also vital in determining the position of smaller translated FRCs, in order to correlate internal probe measurement to the FRC center.

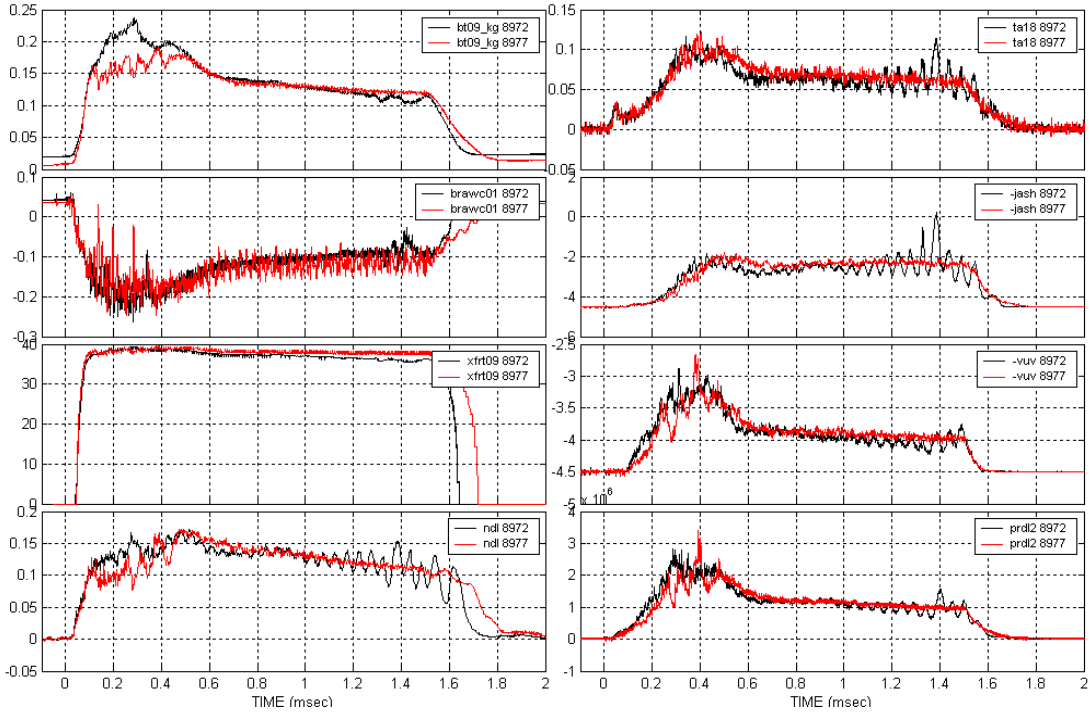

Figure 4-23. Typical data traces for two near identical shots, except for slightly different separatrix radii. Effects of the n=2 rotational instability are apparent on shot 8972 while the similar shot 8977 with the separatrix radii closer to the tube wall appears free of n=2 caused oscillations. The oscillations are apparent on the

Typical time traces are shown in Fig 4-23 for two FRC formation experiments using the external flux rings. Shots of this type were observed to have ion rotations of about 10 kHz using the ICCD diagnostic. The only difference between the two shots was the initial bias field, which was higher for the black traces (#8972) then for the red traces (#8977). (The trace bt09 does not show the true bias field since it is taken right under the flux rings and is strongly affected by the flux ring currents. The timing was designed to result in near equal fields inside and outside the flux rings only after the FRC was formed, so that bt09 reads correctly for the FRC.) The higher bias field led to a slightly smaller separatrix radius, with all other parameters being nearly identical. The small difference in separation from the tube wall led to the oscillatory behavior seen on all the cross-tube traces. If the plasma separatrix was far enough from the wall, this could lead to destruction of the FRC, although it would usually be regenerated if the RMF power was left on.

Tomographic reconstructions are shown in Fig. 4-24 during the initial phase of the FRC generation before any n=2 caused oscillations are seen on the cross-tube instrumentation.

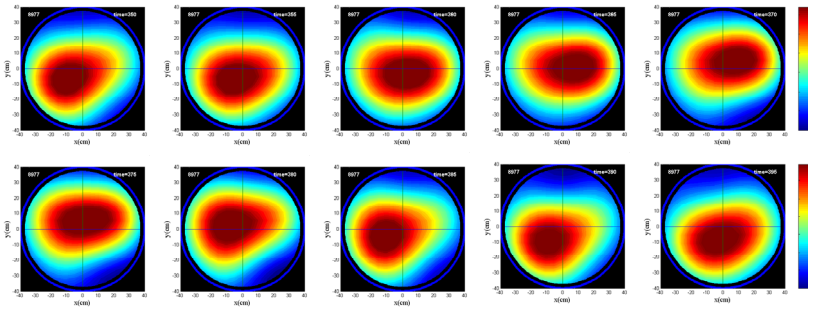

Figure 4-24. "Movie" of the n=1 wobble, using 3 azimuthal, 3 radial modes in the tomographic reconstruction for shot 8977 from 350-395 usec (every 5 usec), left to right, top to bottom.

The tomographic resolution is not fine enough to uncover the internal structure of the FRC (no emission minimum is even seen in the center), but it can indicate overall position and edge distortions. These edge distortions show up in Fig 4-24, where it appears that, although the separatrix radius r_s is less than the wall radius, small changes with azimuthal location can lead to wall contact. Unfortunately, it is not possible to tell if such small effects are real since they could be due to biases in the tomographic reconstruction. The ions are already rotating at about 10 kHz at the time of the reconstructions in Fig. 4-24, and one would expect to see rotation in any distortion if they were real. It does appear, however, that the center of the FRC is wobbling (n=1) in the ion paramagnetic direction. If the separatrix distortion is real, it can have several effects. The first is, of course, impurity ingestion. The second is retardation of the plasma spin-up through viscosity, which is discussed in Section 4.8. The third may be stabilization of the n=2 rotational instability, although that could also be due to closeness to the flux conserving rings.

Tomographic reconstructions during the equilibrium phase of RMF drive are shown in Fig. 4-25 for the larger separatrix radii shot. Although the images display some distortion, the FRC appears to be very stable. At this level of non-rotating distortion the tomographic system is not accurate enough to tell if the reconstructed distortions are real or not, since the tomographic chords are not very accurate at high angles, and could be contaminated by wall light-up.

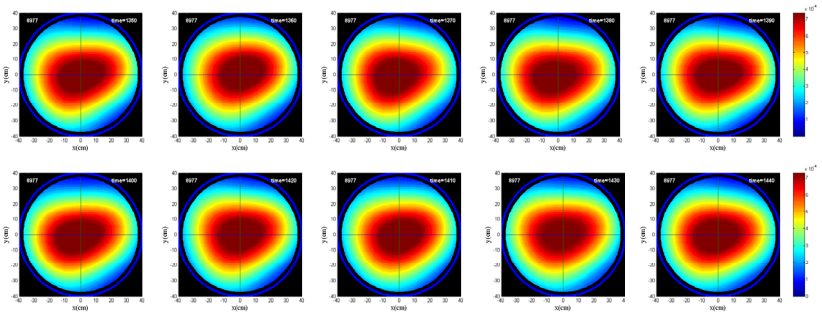

Figure 4-25. "Movie" of a stable FRC, using 3 azimuthal, 3 radial modes in the tomographic reconstruction for shot 8977 from 1350-1440 usec, 1 frame every 10 usec.

The tomographic reconstructions for shot #8972, with the strong oscillations seen by cross-tube instrumentation, are shown in Fig. 4-26. A rotating n=2 distortion is now clearly seen, with a frequency of about 10 kHz (for a full turn), about equal to the ICCD measured ion rotation frequency. It can be seen that there is also some n=1 component. Again, it cannot be said what is limiting the amplitude of the n=2 distortion, but for cases like this it does not have any effect on the overall current drive performance.

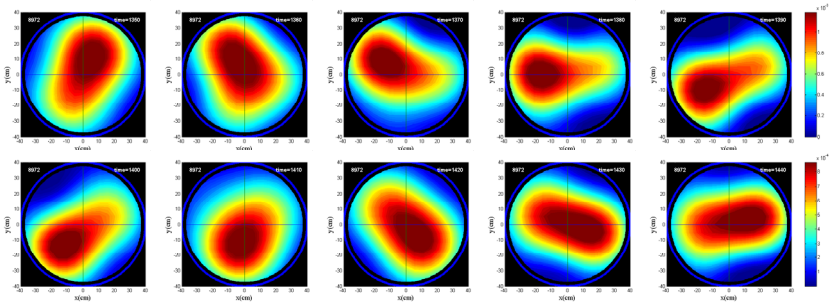

Figure 4-26. "Movie" of the n=2 rotational instability, using 3 azimuthal, 3 radial modes in the tomographic reconstruction for shot 8972 from 1350-1440μsec. 1 frame every 10μsec.

The n=2 distortion is of a large enough amplitude that it rotates at exactly the ion rotation velocity, at least within measurement accuracy. A comparison of the ICCD rotation measurements, with all the cross-tube measurements of the n=2 frequency (for a full rotation), is shown in Fig. 4-27. A plot of B_ω^2 is also shown, which is indicative of the RMF induced torque. The measured rotation frequency appears to decrease with this quantity.

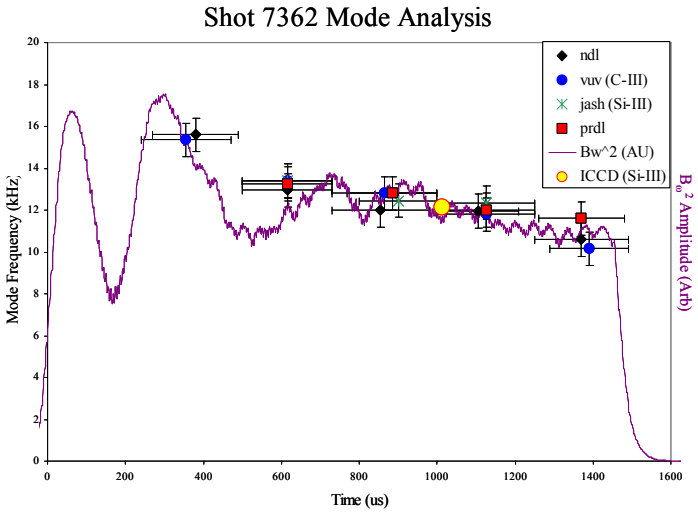

Figure 4-27. Correlation of n=2 rotational mode frequency for various spectrometers, the interferometer, and the ICCD measured ion rotation

4.8 Ion Rotation

The various lines used for the ICCD rotation measurements are listed in Table 4.1. Most of the results shown here are simple chord integrated data without a spectral deconvolution or spatial inversion since that displays the most important features without involved processing. A lot of the measurements were made during operation at $\omega = 0.52 \times 10^6\ s^{-1}$ before installation of the external flux rings.

Table 4.1
Spectral Lines used for Doppler Effect Measurements

Species	Wavelength (nm)	Atomic Mass (AMU)	Ionization Energy (eV)
Dα	656.103	2	13.6
Dβ	486.003	2	13.6
He I	388.865	4	24.6
He II	468.570	4	54.4
C III	229.687	12	47.9
O III	326.533	16	54.9
Si III	455.262	28	33.5

Chord-integrated velocity profiles for the C-III impurity line at 229.687 nm, viewed in third order, are shown in Fig. 4-28 for two repeatable shots. The collection fiber optics have been positioned in both a symmetric fan and an asymmetric fan, as shown in Fig. A-19, for comparison. The results are similar, proving that the inferred rotation is not due to a systematic error in the curvature calibration. Another proof of the validity of the calibration is agreement between first and third order measurements using different gratings and independent calibrations.

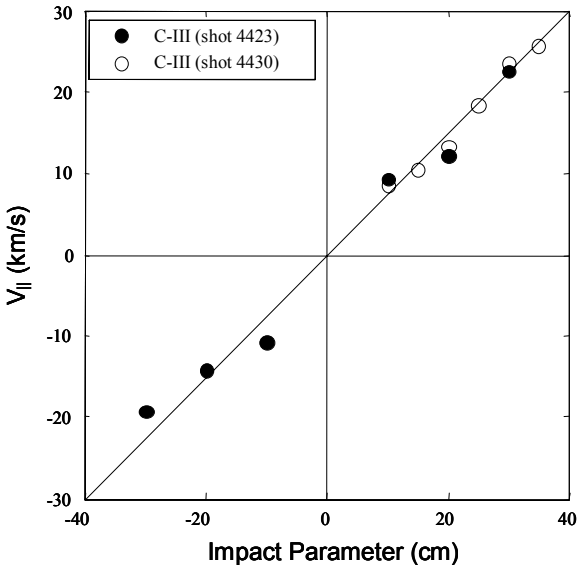

Figure 4-28. Chord-integrated carbon azimuthal velocity. C-III line at 229.687 viewed at third order (689.061 nm) at t=600 μs with RMF frequency ω = 0.5x10^6 s^-1

Carbon is a minority species so there is always the question of whether the carbon ions rotate at the same speed as the bulk deuterium ions. Evidence that they do can be seen from the measurements for Si-III and He-II (when pure helium is used) shown in Fig. 4-29. These ions have atomic masses higher and lower than carbon. No rotation is seen when looking at neutral deuterium. Measurements are shown in Fig. 4-30 for D_α, D_β, and He-I.

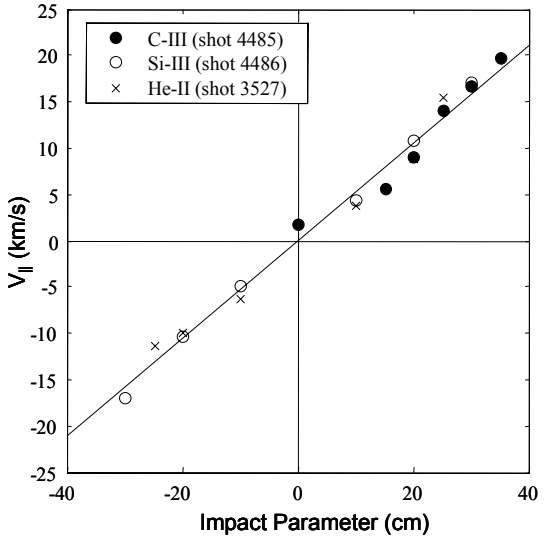

Figure 4-29. Chord-integrated rotation of various ion species. Doppler shift of C-III x3 (689.061 nm), Si-III (455.262 nm), and He-II (468.570 nm) lines for ω=0.5x10^6 s^{-1}.

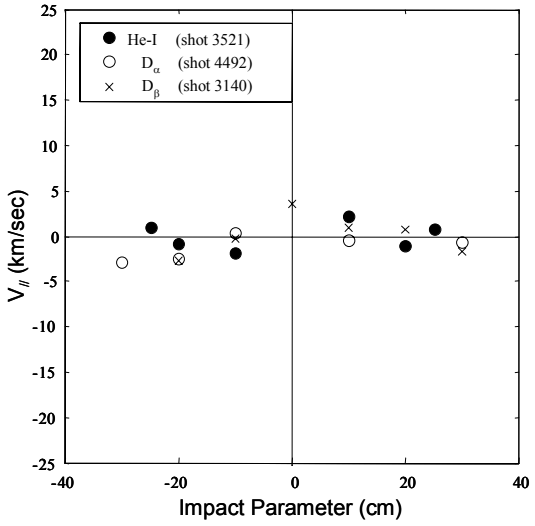

Figure 4-30. Chord-integrated rotation of various neutral species. Data obtained from He-I (388.865 nm), D_α (656.103 nm), and D_β (486.003 nm) lines for ω = 0.5x10^6 s^{-1}.

Although the ion rotation profiles appear to be rigid rotor, a spatial inversion should be performed to prove this. As described in Appendix A.7, a "peel" method of Abel inversion was developed that deconvolves the asymmetric instrument profile from the measured spectra by assuming that each shell radiates with a Gaussian distribution. For this method to be successful the measured spectra must be broader than the instrument function; otherwise the deconvolution will fail. Furthermore, if the velocity profile is anything but rigid rotor it must lead to apparent broadening of the chord-integrated spectra. In these low-density, low-temperature plasmas, Bremsstrahlung continuum radiation often dominates the emission in the wings of the line spectrum. When this background radiation is subtracted, the resulting line spectrum is often narrower than the instrument function, even though the instrument function has been obtained at a similar intensity level. This is particularly a problem when the exposure time is short (less than 50 μs), the signal-to-noise ratio in the wings of the spectrum is low, and the impurity species being viewed is massive and temperature broadening for ~10

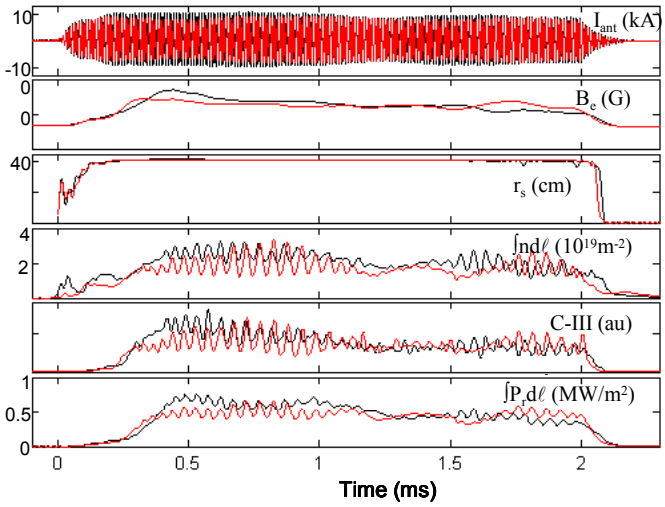

Figure 4-31. Plasma parameters for shots 4430 and 4438. Red line: shot 4430. Black line: shot 4438.

eV ions is insignificant. The instrument functions obtained from Hg and Cd lamps may also be slightly pressure broadened or temperature broadened and may not represent true delta function inputs.

Despite these difficulties, a handful of shots have been obtained where the observed spectra for all chords are broader than the instrument function. Fig. 4-31 shows plasma parameters for two such shots. These plasmas exhibit a mild n=2 distortion even though the separatrix is near the wall. These plasmas therefore do not strictly satisfy the inherent assumption of axisymmetry required for an Abel inversion. Nevertheless, an inversion and deconvolution is attempted.

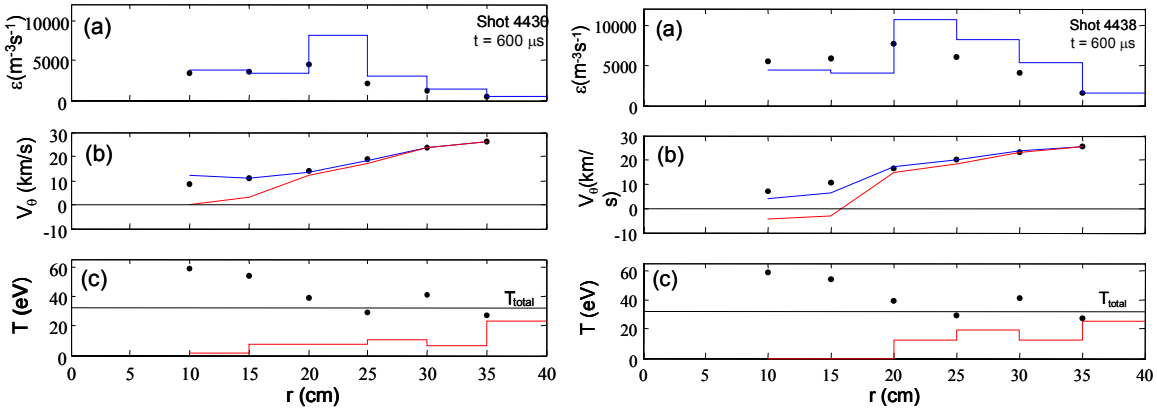

Figure 4-32. Inverted C-III profiles for shots 4430 and 4438. Data from C-III 229 nm line at third order. (a) black dots: chord-integrated brightness. Blue line: matrix inverted emission. (b) black dots: chord-integrated velocity. Blue line: matrix inverted velocity.

The chord-integrated spectra were spatially inverted and deconvolved using both the peel method and a simple matrix inversion technique. Inverted profiles for the C-III line at 229.687 nm, viewed in third order, are shown in Fig. 4-32. Both results are taken at t = 600 μs with a 25 μs exposure. The RMF frequency $\omega = 0.52 \times 10^6$ s^{-1}, the bias field B_o = 66 G, and the total temperature T_t = 32 eV are the same for both cases. For shot #4430 B_ω was 50 G and the average electron density $\langle n_e \rangle = 1.3 \times 10^{19}$ m^{-3}. For shot #4438 B_ω was 65 G, resulting in a higher density $\langle n_e \rangle = 1.7 \times 10^{19}$ m^{-3}. Despite these differences, the results are similar. The top graphs show the chord-integrated brightness data as black points, and the Abel-inverted emission profiles as blue lines. For shot #4430 the emission is peaked at the null, while the higher-density shot has a much broader emission profile. In the middle graphs, the chord-integrated velocity profiles are shown as black points, the matrix-inverted velocity profiles are shown in blue, and the deconvolved velocity profiles are shown in red.

The deconvolved results indicate that the plasma may not be truly rigid, but rather that the plasma near the geometric axis rotates more slowly. Finally, the bottom graphs show the deconvolved temperature profiles in red, along with the instrument temperature for each chord as a black point. The plasma total temperatures are shown as dashed lines. The carbon ion temperature is roughly equal to half the total temperature, although the temperature resolution below the instrument temperature is poor. The inverted spectra

from each shell are shown in Fig. 4-33 in black, along with the convolved Gaussian fit for each shell in red. From the close agreement, it can be claimed that although the inversion and deconvolution may not be a unique solution, it is certainly a valid solution.

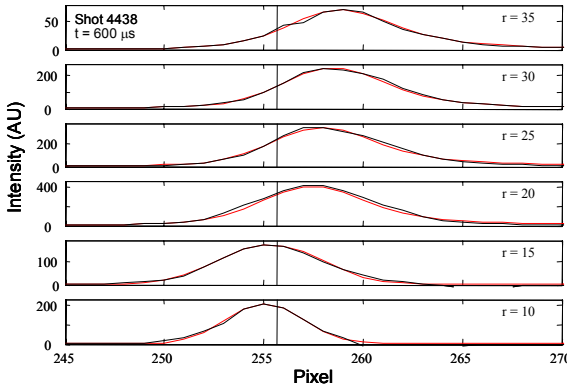

Figure 4-33. Inverted spectra and convolved fit for shot 4438. Black line: inverted spectra. Red line: Convolved Gaussian fit. Dashed line: rest wavelength

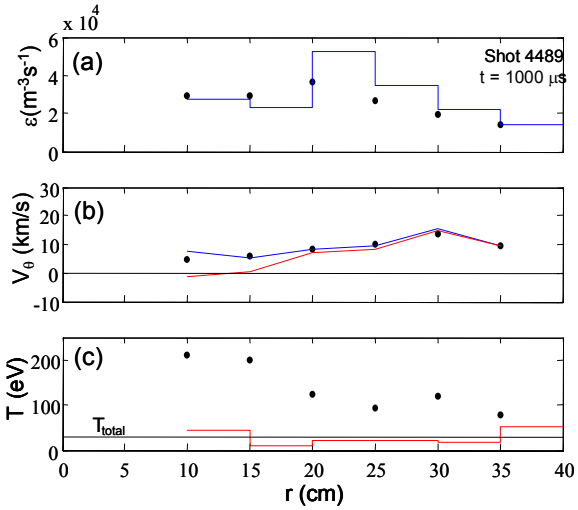

Figure 4-34. Inverted Si-III profiles for shot

Inverted profiles obtained from the Si-III line at 455.3 nm for similar plasma conditions are shown in Fig. 4-34. The emission profile is very similar to that of C-III and roughly follows the plasma density profile. The velocity profile, however, is quite different in that ions at the edge (35 cm) are rotating more slowly than plasma further in. This could be due to the fact that Silicon is introduced at the plasma edge due to wall ablation, and because of its large mass takes longer than carbon to spin up.

The ion azimuthal velocity profile was seen to be very close to rigid rotor. Ions near the geometric axis may be rotating more slowly, but the error bars in the spatial inversion are too large to make a definitive claim of this. In order to compare the ion rotation for different plasma conditions, the ion velocity profile is assumed to be rigid rotor and the chord-integrated velocity is fit to a rotation frequency ω_i: $v_{i\theta}(r) = \omega_I r$. The time evolution of the carbon ion rotation

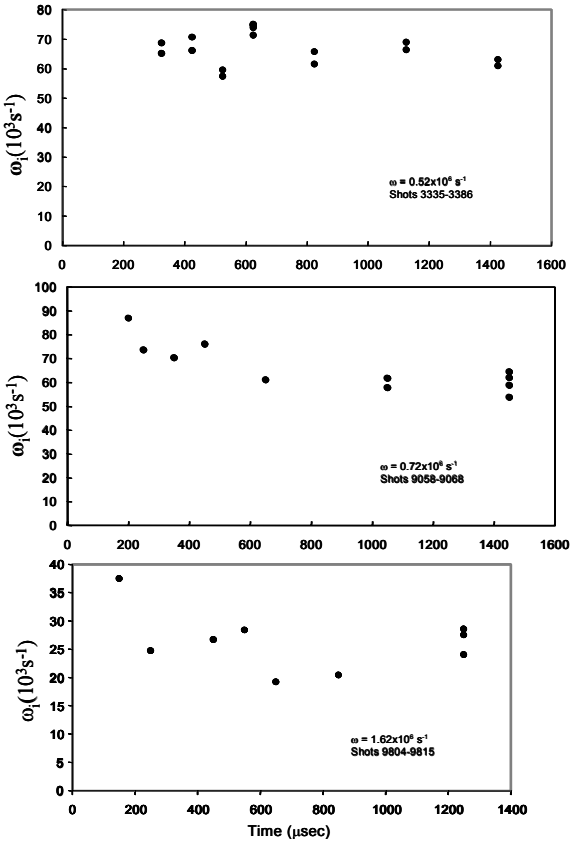

Figure 4-35. C-III rotation frequencies for various RMF frequencies. Top data taken with 50 μsec exposure, others with 100 μsec

frequency is shown in Fig. 4-35 for a series of repeatable shots at three different RMF frequencies. The ICCD camera can only take a single exposure during a shot, so each data point was obtained from a different shot, triggered at a different time. Data was taken as early as C-III started radiating, by which time spin-up to a steady value already occurred.

At the lower RMF frequencies ion rotational speeds were about 0.06×10^6 s^{-1}, only about 10% of the RMF rotational rate. There appears to be some slowing down in the rotation frequency after the initial build-up, which is most likely related to a decrease in RMF torque as the plasma temperature decreases in accordance with the modeling of Section 2. At the highest RMF frequency the ion rotational rate is significantly less, but this may be due to the lower values of B_ω applied under those conditions, and thus the lower RMF torque. The C-III rotation frequency is shown in Fig. 4-36 as a function of ω for the various RMF frequencies applied over the range of B_ω utilized.

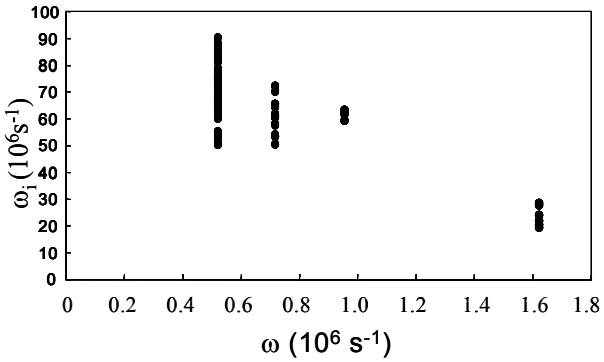

Figure 4-36. C-III rotation frequencies at t =

Regardless of whether the RMF torque is applied directly to the ions (at low ω/ω_{ci}) or to the electrons. It will be transferred to the ions due to electron-ion friction. The torque per unit antenna length is given by Eq. (2.3), $T'_{RMF} = T'_o(\Delta r/r_s)$ with $T'_o = 2\pi r_s^2 B_\omega^2/\mu_o$. For typical values of r_s = 0.38 m and B_ω = 5 mT, T'_o = 9 Nt-m/m. Using the numerical calculation for $(\Delta r/r) = 0.82\zeta^{0.2}/\lambda^{0.6}$, the ion rotation rate for various RMF frequencies is plotted as a function of RMF torque per unit length

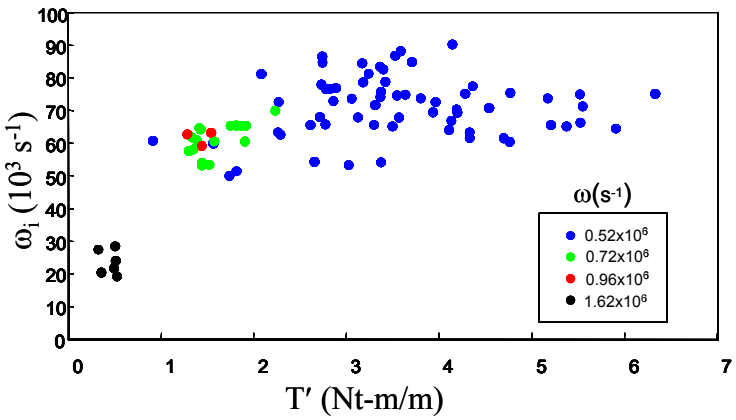

Figure 4-37. Ion rotation versus applied torque for various RMF frequencies, using C-II IICCD data.

$$T'_{RMF} = 0.86\frac{\zeta^{0.2}}{\lambda^{0.6}}T'_o \qquad [4.6]$$

in Fig. 4-37. At the highest RMF frequency, the applied torque is small because B_ω is low. Even if the antenna impedance could be lowered and B_ω at high frequency could be raised to match the field strength at lower frequency shots, the applied torque would still be lower because the penetration depth would be smaller. The fact that the ion rotation

does not scale linearly with the applied torque at lower RMF frequencies must mean that the drag torque is increasing as well.

It may be noted that the resistive torque per unit length can be written as

$$T'_\eta = -2\pi\int_0^{r_w} n_e e\eta_\perp j_\theta r^2 dr = 2\pi\int_0^{r_w} \frac{\eta_\perp j_\theta^2}{\omega_r} r dr = \left\langle \frac{1}{\omega_r} \right\rangle P_{abs\theta}/L_{FRC} \qquad [4.7]$$

since $j_\theta = -n_e\omega_r r$. If we just divide $P_{abs\theta}/L_{ant}$ by $\zeta\omega$ we usually get almost double the value given by Eq. (4.6) since the relative electron ion rotation ω_r is higher near the FRC edge, making $\langle 1/\omega_r \rangle$ much less than $(1/\omega\zeta)$.

In previous analysis researchers have specified ion-neutral collisions as a means of restricting the ion spin-up velocity. We do measure zero neutral rotation velocities, so if their drag on the ions were sufficient, this mechanism could be important. The drag torque due to ion-neutral collisions will roughly scale as

$$T'_n \approx \frac{\pi}{2}\langle S_{in}\rangle m_i \omega_i r_s^4 \qquad [4.8]$$

where the neutrals are assumed stationary and $\langle S_{in}\rangle$ is the average ion-neutral momentum transfer rate. Calling $\langle S_{in}\rangle = n_i n_o(\langle\sigma v\rangle_{in} + \langle\sigma v\rangle_{cx})$ with both $\langle\sigma v\rangle_{in}$ and $\langle\sigma v\rangle_{cx} \approx 2\text{x}10^{-14}$ $m^{-3}s^{-1}$, at a typical density of $n_i = 2\text{x}10^{19}$ m^{-3} and $n_o = 4\text{x}10^{17}$ m^{-3}, $\langle S_{in}\rangle = 3\text{x}10^{23}$ $m^{-3}s^{-1}$. For $m_i = 3.4\text{x}10^{-27}$ kg and $\omega_i = 7\text{x}10^4$ s^{-1}, T'_η only equals 0.6 Nt-m/m. The neutral density would have to be up to five times higher to alone account for the torque balance.

If ion-neutral collisions were the sole drag mechanism on the ions, the ion rotation frequency found by balancing torques, assuming the FRC and antenna lengths were equal, would be

$$\omega_i \approx \frac{2.3B_\omega^2\zeta^{0.2}}{\mu_o\langle S_{in}\rangle m_i r_s^2 \lambda^{0.6}}. \qquad [4.9]$$

The drag term $\langle S_{in}\rangle$ and neutral density required to provide the necessary drag is plotted in Fig. 4-38 versus the plasma density. This is at least twice that measured in the previous section from D_α emission, and would also result in some cases to higher powers being lost to ionization and charge-exchange than are supplied by the RMF. Neutrals alone do not seem able to account for the observed low ion rotation rates. The only other mechanisms are viscosity (to the plasma tube walls) and shorting out of the radial electric field that must be present if the ions are to rotate in the paramagnetic direction.

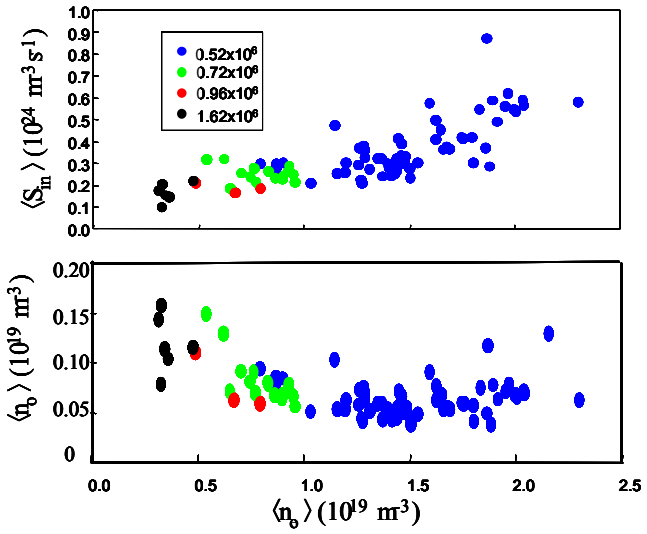

Figure 4-38. Neutral density and neutral drag required if sole mechanism for limiting ion spin-

The relative ion rotation rate appears to scale with plasma density if it is plotted for different RMF frequencies, as shown in Fig. 4-39. However this is misleading since the actual values of ω_i are nearly constant, except at the highest RMF frequency where the applied torques are low.

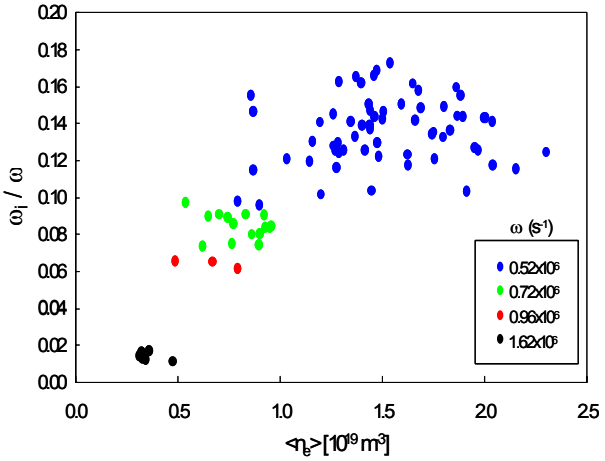

Figure 4-39. Ion rotation scaling with electron

There is no way of evaluating the contribution of radial electric field shorting, but we can make some estimates of possible contributions from viscosity. Since the measured edge density is very low, cross field viscosity should be low. However, it is possible that once the plasma reaches a given rotational speed, some n=2 distortion will develop that would rub on the plasma tube wall. If we call the plasma viscosity

$$\mu = 0.5 m_i n_i \rho_i^2/\tau_{ii} = 0.5 n_i k T_i \tau_{ii}/(\omega_{ci}\tau_{ii})^2, \qquad [4.10]$$

with $\omega_{ci}(s^{-1}) = 4.8\text{x}10^4 B(\text{mT})$ and $\tau_{ii}(s) = 3\text{x}10^{-8} T_i^{1.5}(\text{eV})/n_i(10^{20}\text{m}^{-3})$, then for typical conditions of B = 15 mT, T_i = 15 eV, $n_i = 0.1\text{x}10^{20}\text{m}^{-3}$, $\mu = 1.3\text{x}10^{-6}$ kg/m-s. The ions are magnetized since $\omega_{ci}\tau_{ii} = 12$. The wall torque per unit length is approximately of order

$$T'_\mu \sim \mu(v_{i\theta}/\delta)2\pi r_w^2 = \mu 2\pi r_w^3 \omega_i/\delta\ , \qquad [4.11]$$

where δ is the velocity scale length. For the above values, with δ = 2 cm, $T'_\mu \sim 2$ Nt-m/m, in the same range as the applied RMF torque. However, since the viscosity scales as $n^2_{edge}/T^{1/2}_{i,edge}B^2$, it is hard to imagine how the edge viscosities could be so high with realistic edge densities well under 10^{19} m^{-3}. Rotational centrifugal forces could result in higher separatrix densities, but a more likely explanation is that impurities such as oxygen, with a much higher viscosity due to the higher mass, could contribute significantly.

4.9 Flux, Energy, & Particle Lifetimes

Flux lifetimes are the most important quantity for pulsed FRCs, since they determine the lifetime of the configuration. For the RMF sustained FRCs the effective resistivity is the most important quantity, since it determines how much RMF power must be supplied to maintain the configuration. The energy lifetime is the next most important quantity, since it will determine how hot the plasma can get. Energy lifetimes are really a separate consideration from the power required to maintain the plasma current. Particle lifetimes in pulsed FRCs are similar to flux lifetimes (and energy lifetimes if particle loss is the dominant energy loss mechanism) since they both reflect the same cross-field diffusion process. In the sustained FRCs these processes are uncoupled since normal outward particle diffusion is reversed by the RMF force, with particles presumably lost out the

FRC ends. Particle lifetimes can thus be quite long. They can be estimated from the measured neutral densities and calculated ionization rates.

Power loss will occur due to several mechanisms: radiation (which is usually dominant in the present experiments), ionization, charge exchange, convection, and conduction. The first is measured using bolometry as discussed in Appendix A.9, while charge exchange, ionization, and convection losses are estimated from the measured neutral fraction. The neutral fraction is calculated from the measured D_α signal (photons/m^2s). The number of ionization events can be related to D_α using the function $Id_\alpha(n_e,T_e)$ given in the ADAS database. $\dot{N}_{ion} = (D_\alpha \cdot Id_\alpha \cdot V_p/2r_s)$ where V_p is the plasma volume. The power lost to ionization is then $P_{ion} = \dot{N}_{ion} kE_{ion}$ where E_{ion} is the ionization energy (13.6 eV). The convection losses are $P_{conv} = \dot{N}_{ion}(2.5kT_t + 0.5m_i v_{i\theta}^2)$ where the last term is usually small. The charge exchange losses are $(S_{chx}\dot{N}_{ion}/S_{ion})[1.5k(T_t\text{-}1) + 0.5m_i v_{i\theta}^2]$ where S_{chx} and S_{ion} are the charge exchange and ionization rate coefficients. (The neutral density can also be calculated as $n_o = D_\alpha \cdot Id_\alpha/(2r_s n_e\langle\sigma v\rangle_{ion})$.

We will make a rough estimate of possible conduction losses by assuming classical ion conduction with a temperature gradient such that $dT_i/dr = T_i/\rho_i$. Then $P_{cond} = n_i\kappa_{\perp i}S_{frc}T_i\rho_i$ using $\kappa_{\perp i} = 2kT_i/(m_i\omega_{ci}^2\tau_i)$ with $\tau_i = 0.0066A_i^{1/2}T_i^{3/2}(keV)/n_i(10^{20}m^{-3})ln\lambda$. Taking $ln\lambda$ as 13, $\rho_i = 4.57A_i^{1/2}T_i^{1/2}(keV)/B(mT)$ m, the conduction losses are $P_{cond}(W) = 1.8x10^8(n_i^2(10^{20}m^{-3})/B(mT))S_{frc}(m^2)$. We will use n_i as half the average density.

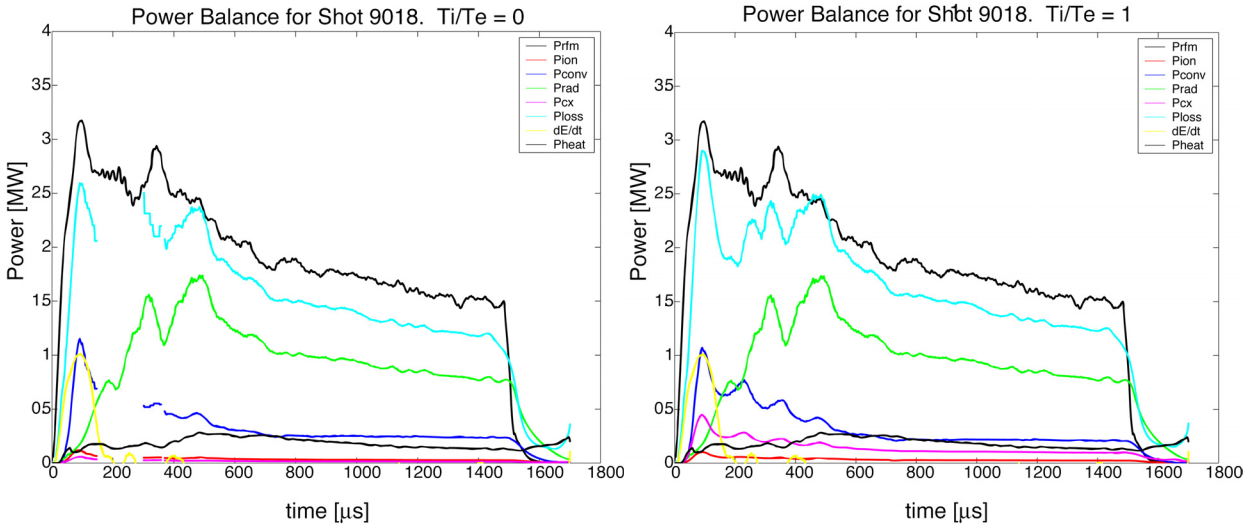

Figure 4-40. Power balance assuming $T_i = 0$ or $T_i = T_t/2$.

Typical power traces are shown in Fig. 4-40 using the above methodology, under the two assumptions that either $T_i = 0$ or $T_i = T_t/2$. The radiated power is dominant and almost equal to the input RMF power. The difference can be mostly accounted for by the combination of convection and the conduction (P_{heat}) power loss.

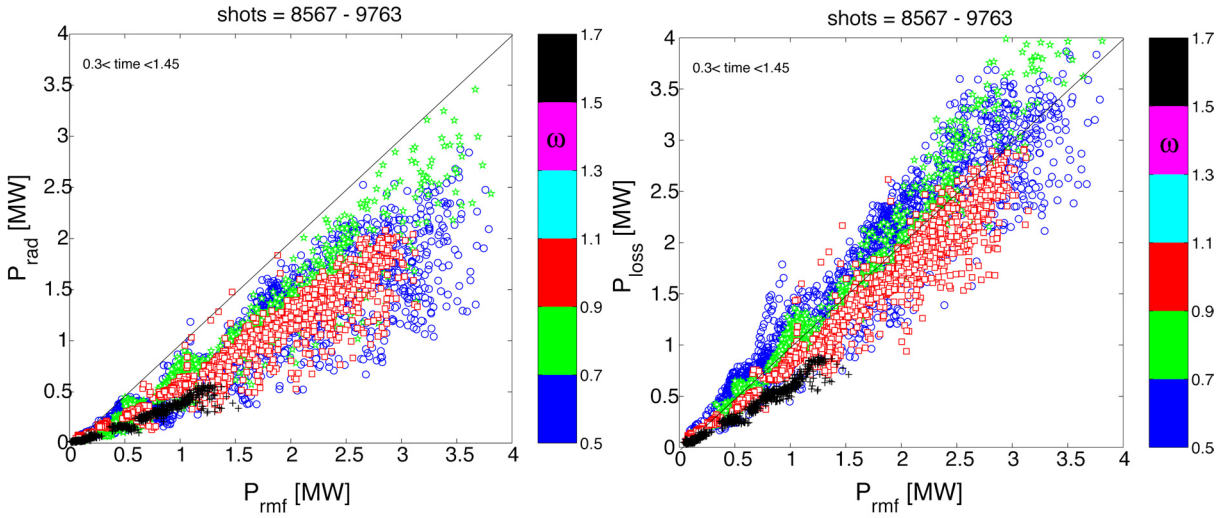

Figure 4-41. Radiated power and total loss power as a function of RMF input power for

The radiated power is plotted in Fig 4-41 for shots in the 'with flux rings' database for 20 times per shot for 253 shots. It can be seen that, except at low power inputs, the radiated power accounts for the largest percentage of the input power. Also shown is the calculated total loss power. Despite our crude approximations, there is good agreement with the total input power.

The plasma energy is calculated from the magnetic probes and flux loops, and the energy confinement time can be calculated in the normal way as $\tau_E = E_p/(P_{rmf} - dE_p/dt)$. Since the number of particles N_p, derived from the interferometer and FRC volume, is approximately constant, the particle confinement time is simply calculated as $\tau_N = N_p/\dot{N}_{ion}$. A typical time history of τ_E and τ_N is shown in Fig. 4-42. In non-sustained FRTP formed high density FRCs most of the energy loss is due to convection and τ_E and τ_N are within a factor of two of each other. For the present RMF sustained FRCs τ_E is short due to the high radiation losses, and τ_N is relatively long due to the inward pinch forces of the RMF, similar to what is seen in tokamaks.

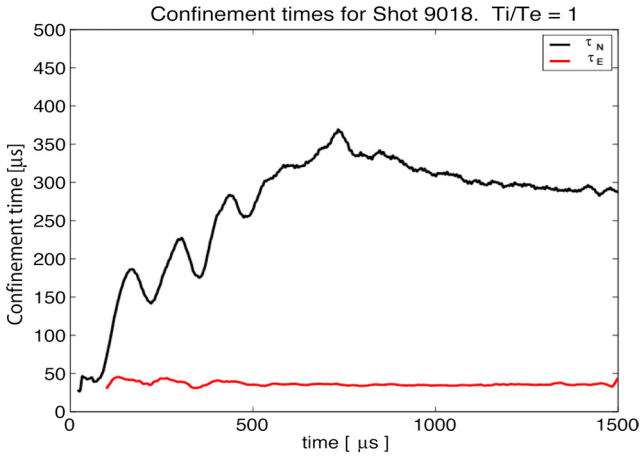

Figure 4-42. Particle and energy confinement times for a typical shot.

4.10 Impurity Studies

Spectroscopic measurements were made to investigate which impurities were important, how much impurity was present, and even to try and ascertain where the impurities were coming from. Three lines were monitored; O-III (326.5 nm), Si-III (455.3 nm), and C-III (2290 nm). C-V was only seen in the translated FRC. None of the monochrometers were absolutely calibrated, so any inferences of impurity content could only be made from doping studies. All measurements were line of sight across a diameter, and they were best normalized by the interferometer $\int n_e d\ell$ signal to approximate the line radiation per electron density, which should be roughly proportional to impurity content if the temperatures and time variations of shots were similar. Correlations could be made with the bolometer signal, prdl, normalized by $\int n_e d\ell$, to estimate the relative importance of each impurity species.

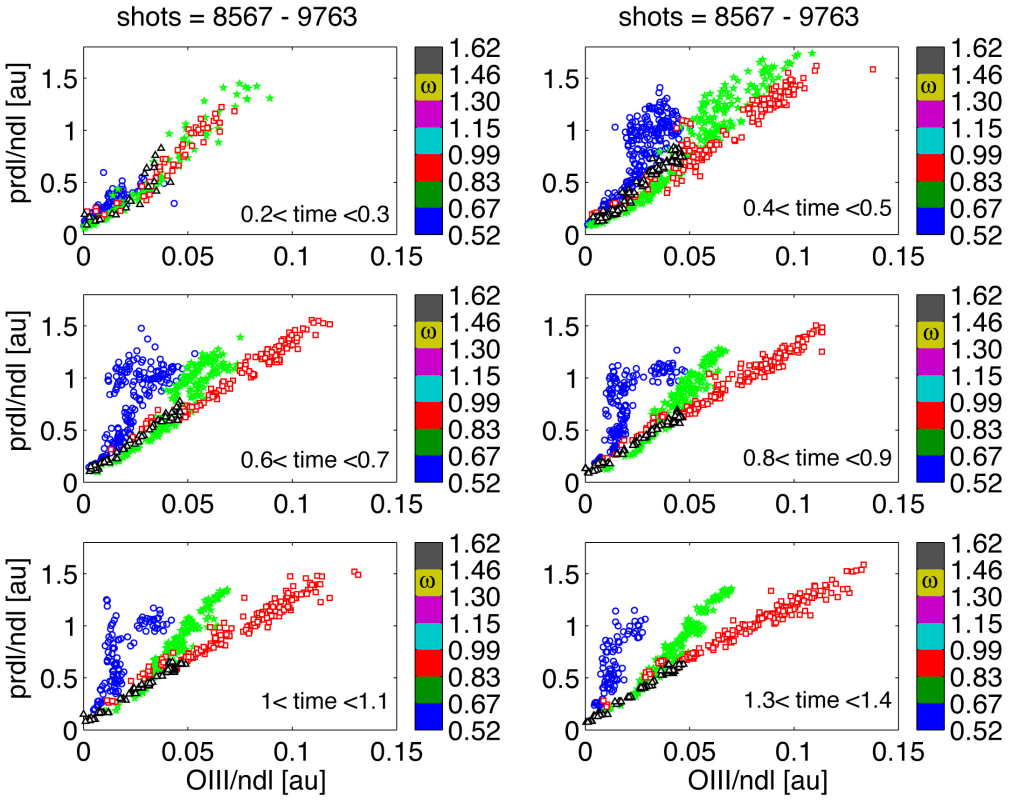

Figure 4-43. Radiation as a function of O-III line intensity for different times in the discharge.

The oxygen radiation is shown in Fig. 4-43 for the various RMF frequencies used, at various times during the discharge. There is always very good correlation between the radiated power and the oxygen line radiation. However, except for early in the discharge, there appears to be much more oxygen present for a given amount of total radiated power for the higher frequency shots. This is surprising since the input RMF power tends to scale as $\omega^{1/2}B_\omega^2$ as shown in Fig. 4-44. Since $n_e \propto B_\omega/\omega^{1/2}$, the absorbed power scales as $P_{rmf} \propto n_e^2\omega^{3/2}$. If the oxygen line radiation, P_{lO} is assumed to scale as $n_O n_e$, then the ratio of P_{lO}/P_{rmf} would scale as $(n_O/n_e)/\omega^{3/2}$. Even if prdl scaled as $P_{rmf}/\omega^{1/2}$, P_{lO}/prad would

scale as $(n_O/n_e)/\omega$. This would yield the impurity fraction n_O/n_e scaling as $(P_{lO}/prad)\omega$, which says that the oxygen impurity fraction is roughly constant for a given frequency whatever the density or power input, and it is much higher at higher frequencies.

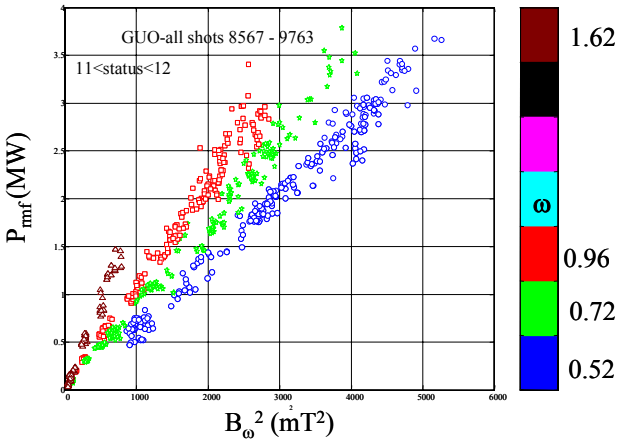

Figure 4-44. Absorbed RMF power versus B_ω^2.

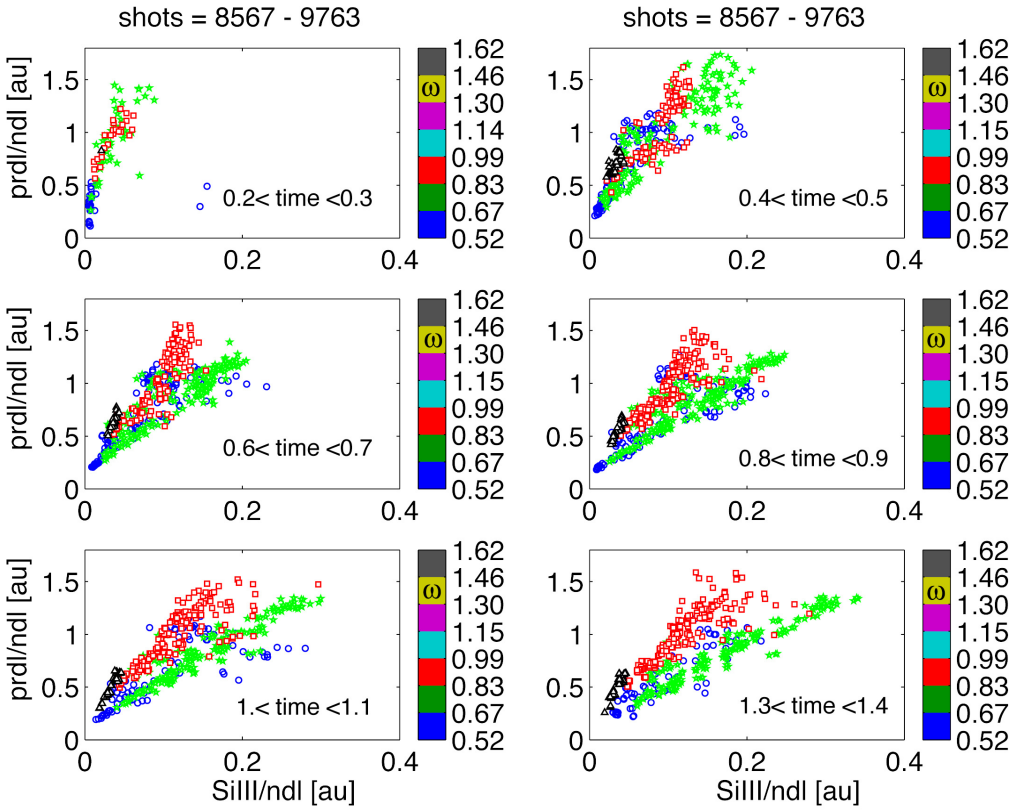

Figure 4-45. Radiation as a function of Si-III line intensity for different times in the

The same type of plots are shown in Fig 4-45 for silicon radiation. This has the opposite trend, with silicon radiation being stronger for the low RMF frequencies. This could be accounted for by the above arguments, which would say that the fraction of silicon impurity is roughly constant with density or absorbed power, and also doesn't appear to change much with RMF frequency. The carbon line radiation behaves similar to that for silicon, as shown in Fig. 4-46, but the data scatter is greater.

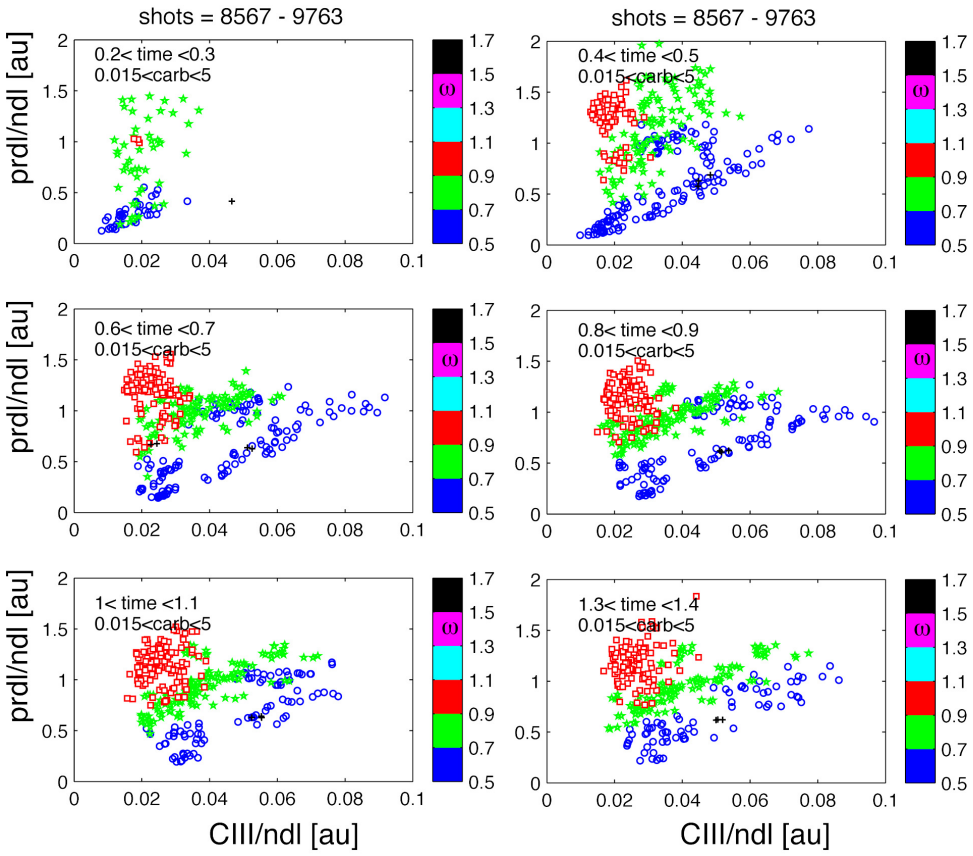

Figure 4-46. Radiation as a function of C-III line intensity for different times in the discharge.

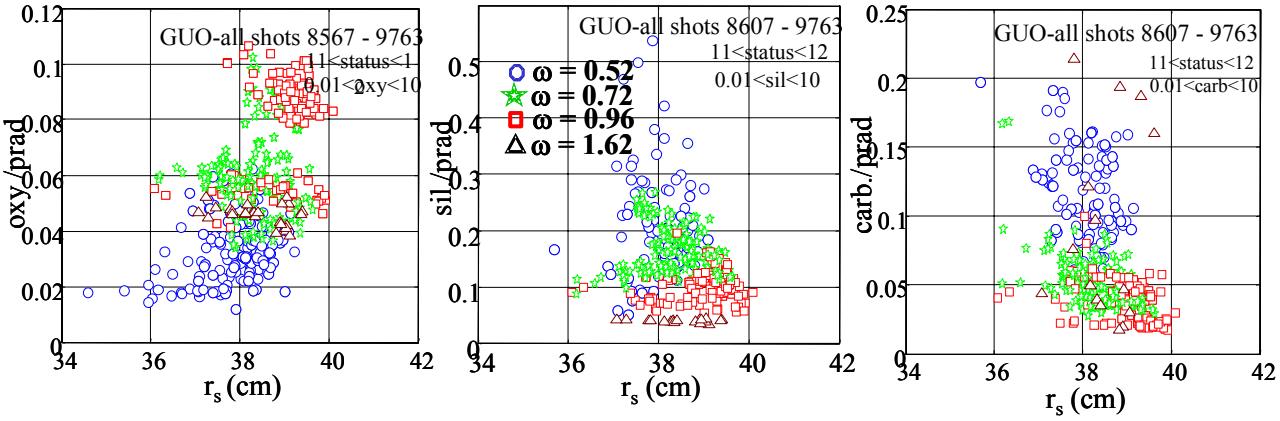

Figure 4-47. Normalized line radiation as a function of separatrix radius.

It might be thought that the amount of impurities, especially silicon and carbon, which probably come from the plasma tube walls, would be related to the closeness of the FRC separatrix r_s to the tube wall at r_w = 40 cm. The various impurity line monochrometer signals, normalized by the total bolometer signal, prad, are shown in Fig 4-47 as a function of r_s. There does not appear to be any correlation with closeness to the wall. The apparent correlation in the oxygen signal is probably more due to the

discharges conducted at $\omega = 0.96 \times 10^6$ s^{-1}, which produced more oxygen line radiation, being run with higher x_s values than the $\omega = 0.52 \times 10^6$ s^{-1} discharges.

A series of doping experiments was run to try and estimate the impurity content by plotting the line radiation as a function of doping fraction. This, of course, assumes that the plasma conditions, i.e. density and temperature, do not change. For the dominant loss producing species this is not a good assumption since, if there is enough impurity to form a radiation barrier, the radiation rate per ion will probably be a steep function of temperature. The sensitivity to impurity content will then be very small, with the plasma just reaching conditions needed to radiate away whatever input power is absorbed.

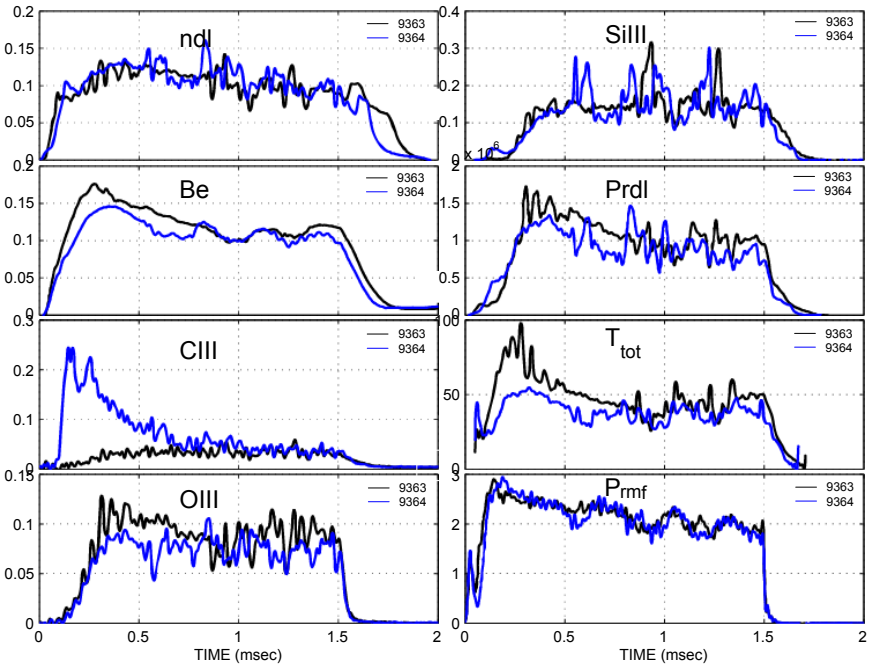

Figure 4-48. Time dependence of various plasma properties for a shot D2 without doping, 9363-black, and a shot with 25%CD4, 9364-blue

Two nearly identical discharges, one with pure D_2 and the other doped with 25% CD_4, are shown in Fig. 4-48 with $\omega = 0.72 \times 10^6$ s^{-1}. A large increase in CIII line radiation is seen, but only at the beginning of the discharge. The decay is consistent with the several tenths of a msec confinement times shown in Fig 4-42. After 0.7 msec the plasma parameters are essentially identical to those without the doping. This seems to imply that particle resupply is coming from the chamber walls, and not from the initial gas fill. If

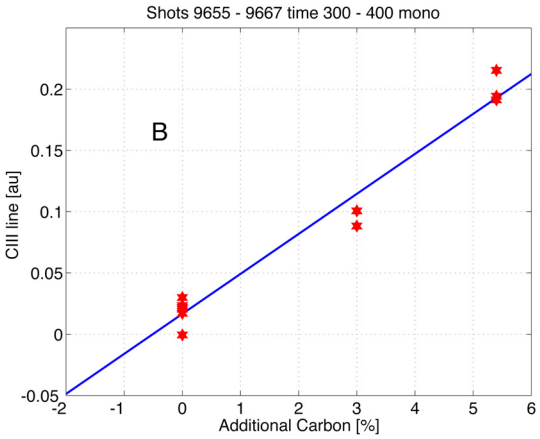

Figure 4-49. CIII line intensity for various CD4 additions to the plasma.

we plot the integral of the CIII signal between 0.3 and 0.4 msec as a function of doping percentage, the zero value intercept gives an idea of the basic C-III fraction. This is seen to be about 0.5% in Fig. 4-49. At later times the carbon impurity fraction in an undoped plasma certainly increases.

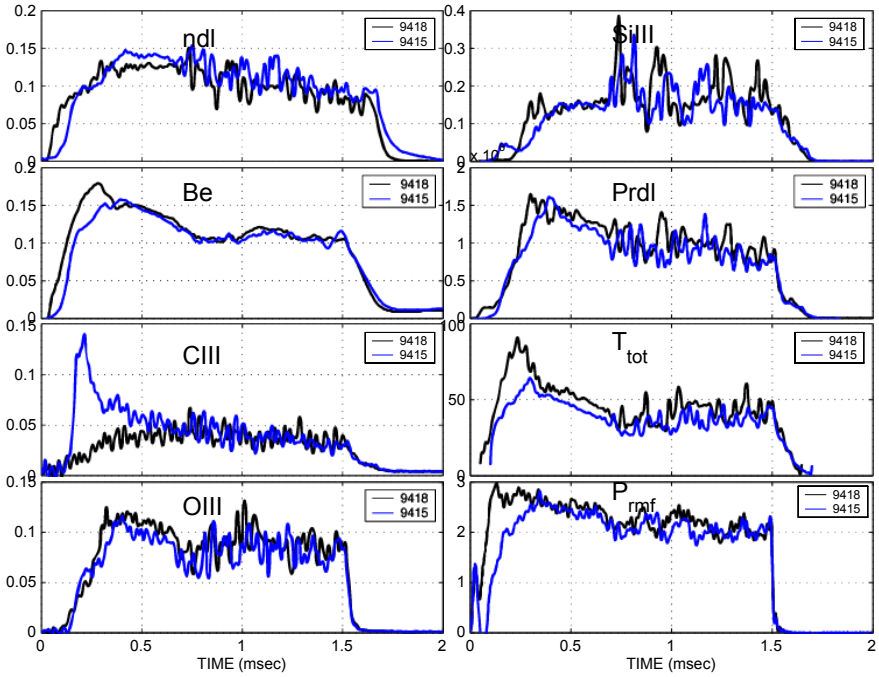

Figure 4-50. Time dependence of various plasma properties for a shot D2 without doping, 9416-black, and a shot with 25%CO2, 9415-blue.

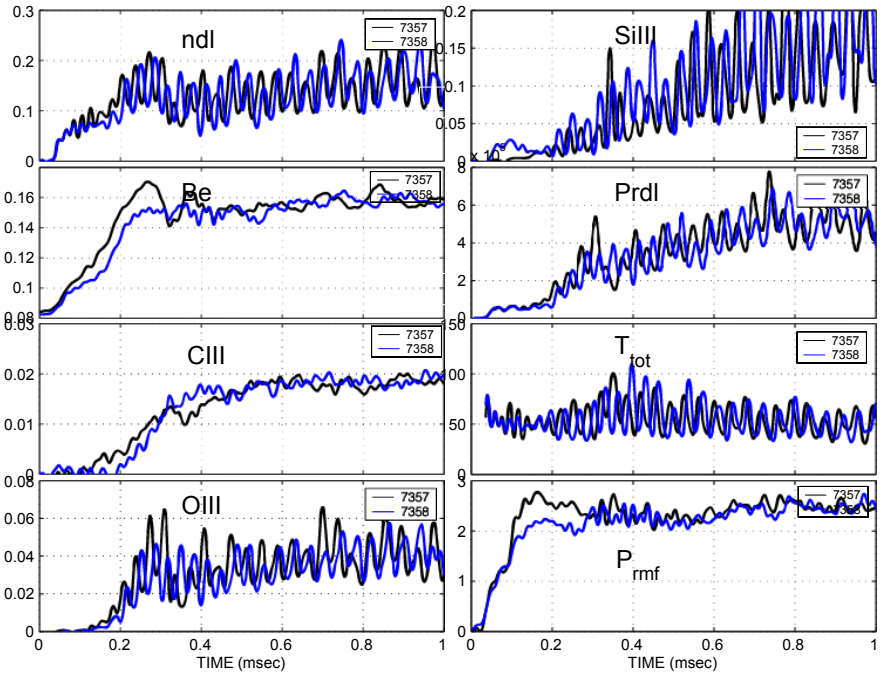

Figure 4-51. Time dependence of various plasma properties for a shot D2 without doping, 7357-black, and a shot with 1%SH4, 7358-blue.

Similar data traces are shown in Fig. 4-50 for a case with 25% doping of CO_2. There is a similar increase in the carbon signal, but no enhancement of the undoped oxygen signal. This implies that oxygen is the impurity which sets the observed radiation barrier. It is significant that the same performance is achieved in such highly doped plasmas as in assumed 'pure' D_2.

The same type of traces are shown in Fig. 4-51 for discharges with and without a 1% SiH_4 doping. A change in silicon line radiation is visible only in the very early portion of the discharge. After 0.2 msec the silicon content appears to be dominated by influx from the walls. Since a larger addition of SiH_4 was not possible due to safety hazards, determination of the amount silicon in the plasma by the doping method was not possible.

Table 4.2
Equilibrium Impurity Radiation Rates

Impurity	P_{rad} (W-m^3)	$T_{peak\ rad}$ (eV)
D	$5x10^{-35}$	1.5
C	$0.8x10^{-31}$	9
"	$0.8x10^{-33}$	100
O	$0.8x10^{-31}$	25
"	$1.0x10^{-33}$	250
Si	$0.8x10^{-31}$	100
"	$2.0x10^{-33}$	1000
Fe	$10^{-31} – 5x10^{-31}$	10-100

It can be inferred from the above measurements that, after the initial few 100 μsec, our plasmas contain several percent carbon and silicon, and a much larger amount of oxygen. The deleterious effect of these impurities can be seen from Table 4.2. Oxygen radiation for equilibrium conditions peaks at $T_e \sim 25$ eV at $\sim 10^{-31}$ W-m^{-3}, so that at a typical density of $n_e = 2x10^{19}$ m^{-3}, the radiation rate would be $p_{rad} \sim 40 f_O$ MW/m^{-3}, where f_O is the fraction of oxygen. Since the FRC volume is about 1 m^3, ten percent oxygen would easily radiate the maximum 4 MW that is ever supplied to the plasma by the RMF. Even if the temperature could be raised quickly beyond 25 eV, it takes a density-time product of about 10^{17} m^{-3}s (up to T_e at least double the value of $T_{peak\ rad}$) for the impurity to be ionized far enough for the radiation rate to be decreased significantly. This is about 5 msec for our conditions, longer than the length of our entire discharges. The doubly ionized C-III or O-III state peaks in equilibrium at about $T_e = 18$ eV, but it is still probably a good measure of the amount of impurity since it takes about $2x10^{16}$ m^{-3}s for the ion to be stripped further. This is about 1 msec for our conditions, which is still longer than the particle lifetime.

The prime focus of the new modifications to TCS is to reduce the impurity level to allow high temperatures to be achieved. It is thus important to try and understand where the impurities are coming from. The doping measurements suggest that carbon and silicon are initially present at fairly low levels, and must increase with time due to ingestion from plasma interaction with external surfaces. It is hard to draw any conclusions about oxygen since the oxygen line radiation rate and even total radiation rate does not seem to be highly effected by even a 25% doping with CO_2. However, it was possible to achieve high initial total temperatures for the first few 100 μsec when the input power was high and the density low, as shown in Fig. 4-9. Since it takes essentially zero time to establish high radiation rates (the more outer shell electrons the greater the

radiation), the ionization time of the impurities is not a factor, but it may be that we could simply overpower very high radiation rates during the time when the electron density was building up.

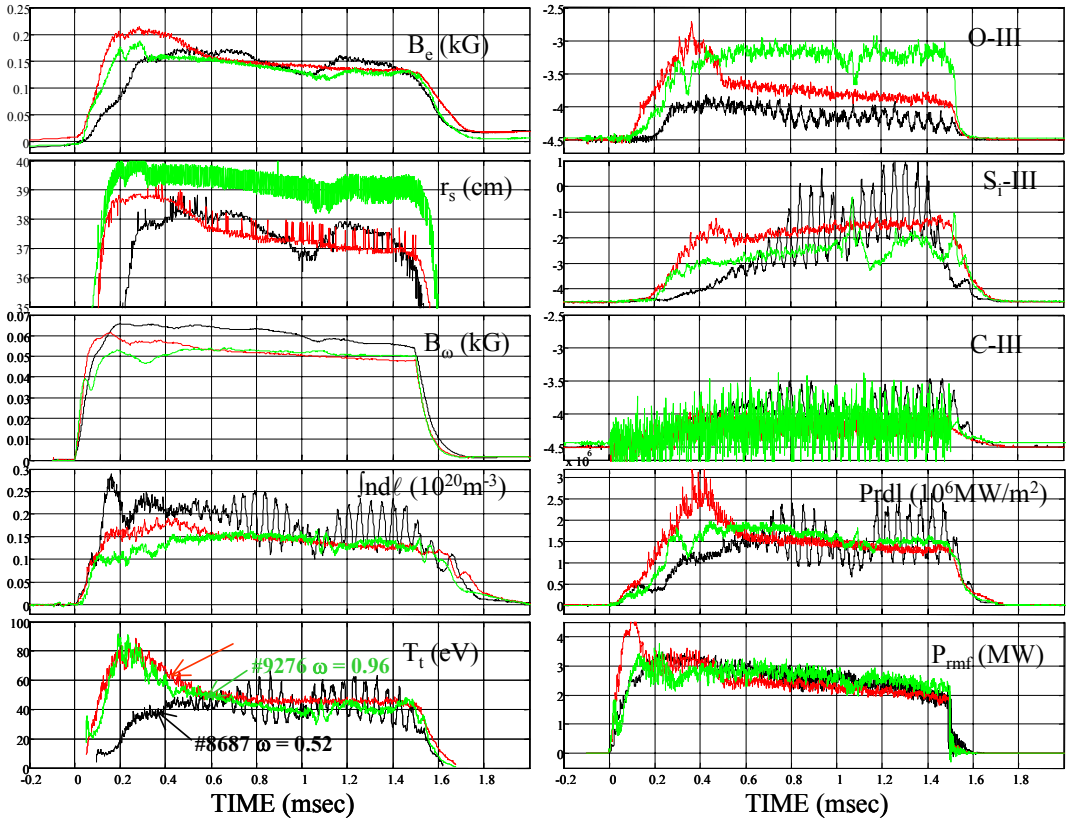

Figure 4-52. Data traces showing impurity line behavior for discharges at three different RMF frequencies with nearly the same plasma conditions.

Another question that arises is why there is such different behavior of the different impurity species for different RMF frequencies, as seen in Figs. 4-43, 4-45, and 4-46. The oxygen line radiation (as a fraction of total radiation) is higher at the high frequencies, while silicon and carbon radiation are higher at low frequencies. Typical time traces for discharges at different RMF frequencies, with similar plasma conditions, are shown in Fig. 5-52. At the higher RMF frequencies the FRC is formed earlier, with a higher initial temperature, perhaps resulting in more oxygen liberation. The n=2 rotational instability tended to be better stabilized at the higher frequencies. The build-up of silicon and carbon at the lowest RMF frequency may

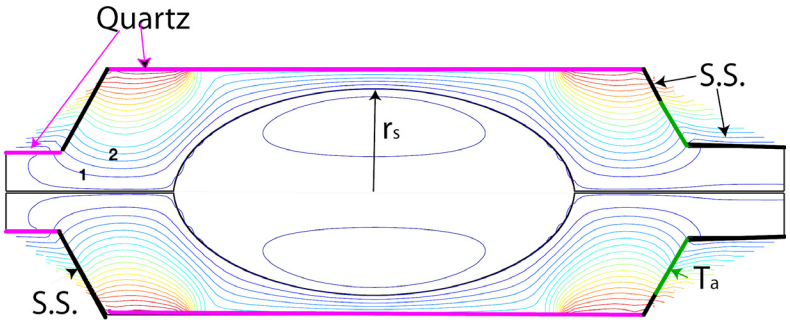

Figure 4-53. Schematic of RMF driven FRC showing external flux

be related to plasma contact with the quartz plasma tube walls, although, as can be seen in the field plots in Fig 5-53, exhaust plasma can also contact the end of the input quartz acceleration tube.

It appears most likely that quartz and carbon impurities come about from direct interaction of the plasma with the plasma tube quartz walls. The heat flux is not high enough to actually ablate the quartz, but there could be a combination of sputtering and loosely bound contaminants. Oxygen impurities are probably present to some extent in the gas fill, perhaps from the preionization method employing the ringing PI of LSX/mod. There may also be contributions from the stainless steel end cones where open field line exhaust plasma can make contact if not impeded by the RMF, especially if the exhaust occurs mainly from the FRC ends. Water vapor is known to be a large problem with bare stainless surfaces. The new modifications to TCS are being designed to address all of these possibilities.

4.11 Antenna Length Effects

We wished to use only a single 1.25-m long quartz tube in the new modification to TCS in order to minimize the number of joints. We thus made some studies of antenna length effects (actually somewhat after the grant period being reported on here). In order to do this in an economical manner, we changed from the 3" diameter tubes used on the original 1.6-m long antenna to 1.5" wide copper strips. Considering the strip antennas as equivalent to 1-cm radius hollow tubes (about the same circumference), the calculated self inductance of each leg increased from 3.2 μh to 4.55 μh (see Table 3.2). Since the mutual inductance between the two rectangular legs of the antennas was about M = 0.55 μh, the calculated total inductance $L_{ant} = (L_{self}+M)/2$ changed from 1.88 μh to 2.55 μh. The actual measured inductances were 1.8 μh and 2.5 μh.

We first investigated changing the radial location of the 1.6-m long strip antennas from 54 cm to either 50 cm (placed directly on the axial field coils) or to 60 cm. It was thought that moving the antennas closer to the plasma tube might reduce performance due to higher order modes being accentuated ($r_s/r_{ant} < 0.7$ had been our rule-of-thumb for minimizing higher order modes), but we did not see any major effects. We thus kept to the 50-cm distance for the antenna length studies, which are outlined in this section.

The strip-line antennas were run at lengths of 0.7, 1.0, and 1.6 meters. A 2.6-m long antenna was also tried, but its location had to be moved to r_{ant} = 60 cm due to physical constraints, and it was also run at a considerably lower RMF frequency than the other antennas due to its higher inductance. Typical time histories of important quantities are shown in Fig. 4-54 for the three antennas. Two things were immediately noticeable as the antenna length was shortened. The first was that the operation became much more stable, with the separatrix radius being able to be kept further from the plasma tube wall (and the external flux rings) without resulting in a significant n=2 rotational distortion. This was in spite of the fact that the plasma rotational speed was unchanged. The initial bias field B_o was thus kept higher for the shorter antennas to take advantage of this capability.

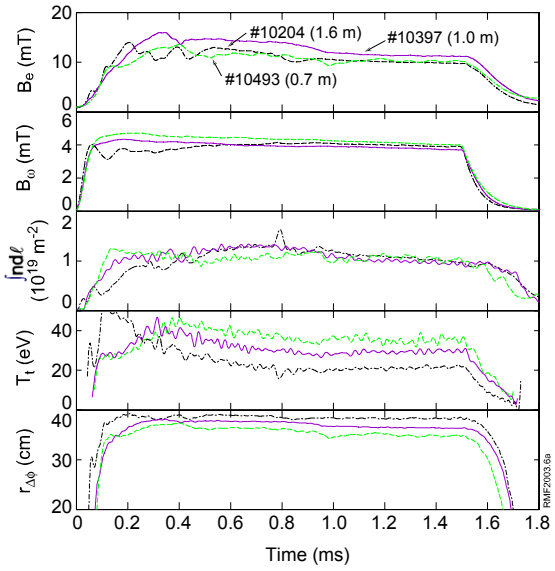

Figure 4-54. Basic data traces from operation with three different RMF

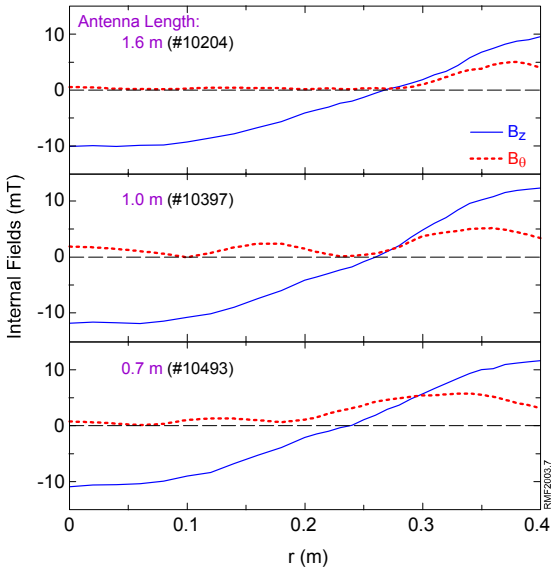

Figure 4-55. Comparison of $B_z(r)$ profiles for different antenna lengths

The second observation was that the internal $B_\theta(r)$ profile changed from the somewhat unusual profile shown in Fig. 4-10, where the RMF does not penetrate fully to the field null, to a more expected profile with greater RMF penetration, as shown in Fig 4-55. We have been investigating possible reasons for the lack of penetration to the field null in our MHD code, which can only be accounted for by having a variable resistivity profile which is much higher at the edge of the FRC than near its field null. However, we presently have no method of modeling 3-D effects, and the observed changes may be related to differences in the ratio of FRC length to antenna length. The shorter antennas produced FRCs with larger values of ℓ_s/ℓ_{ant}. Since the antennas need to produce enough torque to overcome the total FRC electron friction, n_e should be lower for the shorter antennas, all else being equal. If the same external field were to be produced, Δr would have to be larger. It is interesting that as long as sufficient RMF torque is applied to balance the total FRC resistive torque, the RMF finds a way to maintain the FRC.

Table 4.3
Conditions at 1 msec for various antenna lengths with similar RMF fields.

ℓ_{ant} (m)	ω ($10^6 s^{-1}$)	B_ω (mT)	ℓ_s (m)	ℓ_s/ℓ_{ant}	r_s (cm)	B_e (mT)	n_{em} (10^{19} m^{-3})	T_t (eV)	P_{abs} (MW)	P_{rad} (MW)
0.7	0.64	4.3	1.20	1.7	35	11	1.0	36	1.0	0.6
1.0	0.66	4.0	1.40	1.4	37	12	1.3	28	1.2	0.9
1.6	0.80	4.1	1.75	1.1	39	10	1.4	20	1.4	1.4
2.6	0.47	4.1	1.30	0.5	39	11	1.4	24	1.1	0.5

The RMF values of B_ω and ω were kept as close as possible for the three shots displayed in Figs. 4-54 and 4-55. From the point of view of producing the highest external field, the 1.0-m antenna appears to be optimal. The temperatures also appear to be higher for the shorter antennas. The total temperature is derived from radial pressure balance, based on the pressure profile obtained from the internal $B_z(r)$ and $B_\theta(r)$ profiles, assuming that the total temperature was uniform. More detailed information is shown in Table 4.3 for the three different pulses during the equilibrium phase (t = 1 msec). Data is also shown for a comparable pulse obtained with the 2.6-m long antenna (#10600). It can be seen that the shorter the antenna, and the further the FRC can be kept from the wall, the higher the temperature.

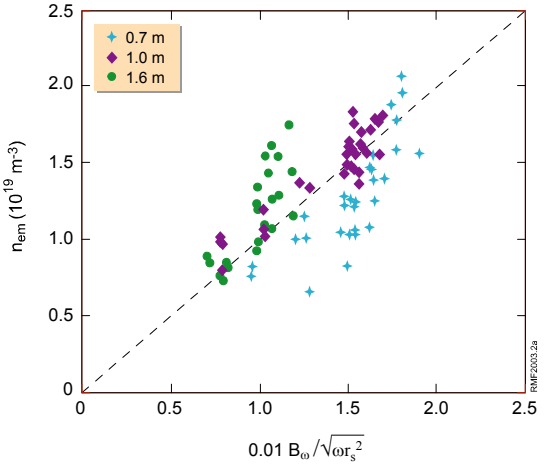

Figure 4-56. Peak density as a function of scaling parameter for various antenna

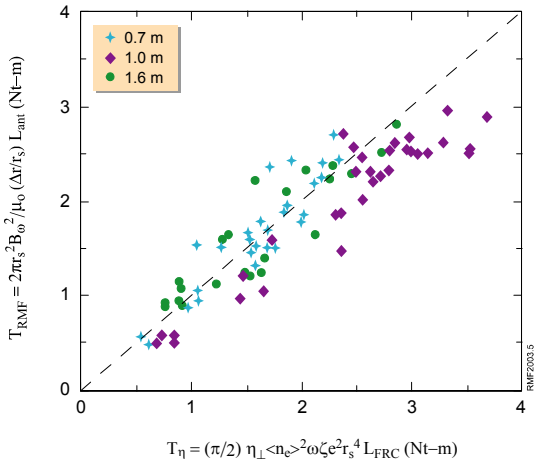

Figure 4-57. Applied RMF torque, T_{RMF}, versus the total resistive torque, T_η, for various antenna lengths. Δr is the

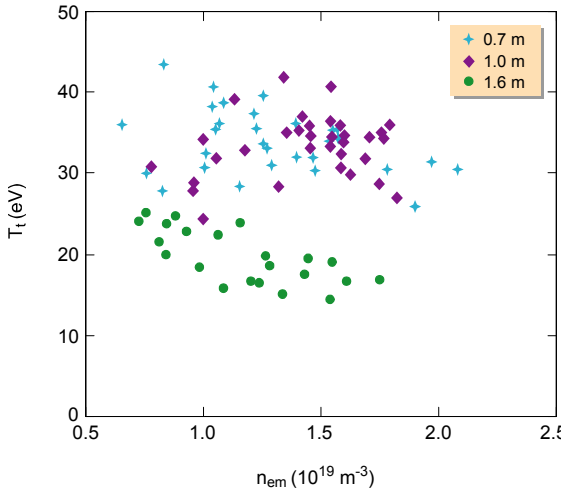

Figure 4-58. Total temperature as a function of

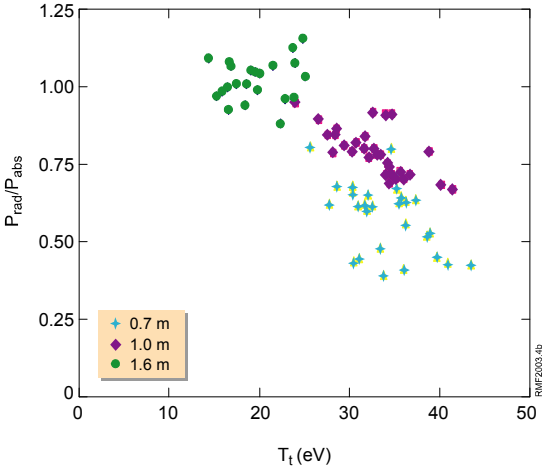

Figure 4-59. Ratio of radiated to absorbed power for various antenna lengths versus total temperature

Several database plots are shown in Figs. 4-56, 4-57, 4-58, and 4-59 for the three antenna lengths. Figure 4-56 shows the achieved peak density as a function of the previous empirical scaling parameter $0.01B_\omega/(\omega r_s^2)^{1/2}$. It appears that n_{em} is slightly lower for the shortest antenna, probably for the reason discussed above. This discrepancy would tend to disappear if we plotted n_{em} versus $B_\omega(\ell_{ant}/\ell_s\omega r_s^2)^{1/2}$. Equating total antenna and resistive torques in Fig. 4-57 shows this scaling.

The total temperatures exhibit the opposite tendency, with higher temperatures realized for the shorter antennas, as is shown in Fig. 4-58. This may be related to a lower ratio of P_{rad}/P_{abs}, as is shown in Fig. 4-59. Other losses may become important for the shortest antenna, such as particle loss out the ends where the FRC extends well beyond the antenna.

The external fields are higher for the shorter antennas for a given value of n_{em} or $B_\omega/(\omega r_s^2)^{1/2}$ due to the higher temperatures. The ratio of B_e/B_ω also appears to be highest for the 1.0 m antenna when plotted against the previous scaling parameter, $0.59\lambda^{0.7}\zeta^{0.6}$, which may be related to a smaller value of $(\gamma/\lambda)_{req}$, or simply due to inaccuracies in comparing the effective resistivities for the various configurations. The database plots of $\eta_\perp$ based on Eqs. (2.16) and (2.17) exhibit the same type of scaling with (B_e/B_ω) as seen in Fig. 4-6, but with slightly higher resistivities for the shortest antenna.

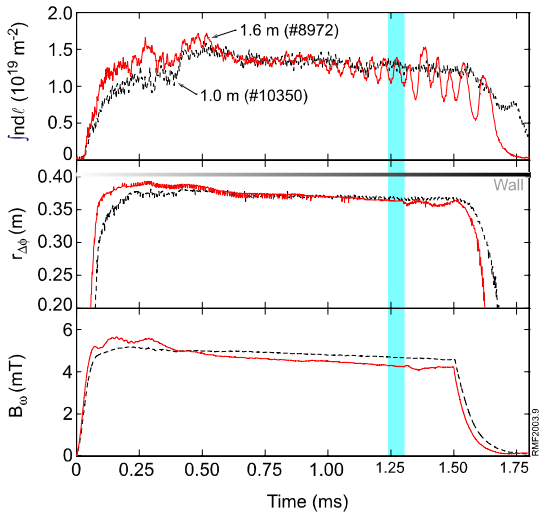

Figure 4-60. Two comparable shots with similar RMF field strengths and frequencies: $\omega = 0.66x10^6\ s^{-1}$ for #8972, and $\omega = 0.72x10^6\ s^{-1}$ for #10350, but with

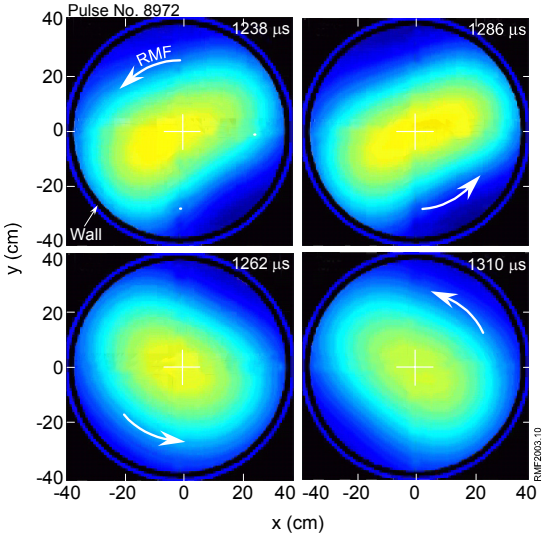

Figure 4-61. Tomographic reconstruction for #8972 during the period indicated on Fig. 4.29 to illustrate the structure of the rotational mode. The direction of rotation

As mentioned earlier, operation with the shorter antennas is less prone to rotational instabilities. To demonstrate this, Fig. 4-60 compares two pulses obtained with the standard 1.6-m long antenna and the 0.7-m strip long antenna, respectively. The two

discharges had similar RMF field strengths and frequencies. The plasma density and the separatrix radius were also kept the same. As can be seen, the rotational instability started to grow after a stable period of about 1 ms in the discharge with the longer antenna, as indicated by a growing modulation of the line integrated density. In contrast, the discharge with the 1.0-m antenna stayed oscillation free for the entire discharge. The structure of the rotational instability can be seen from the tomographic reconstruction in Fig. 4-61. Note that the instability can be suppressed by operating at a lower initial bias flux to enable the FRC to expand closer to the wall, for example, see #10204 in Fig. 4-54.

For typical conditions with $T_i \approx T_e \sim 15$ eV, $B_e \sim 15$ mT, R = 27 cm, the diamagnetic drift for ions in a rigid rotor profile,

$$\omega^* = \left(\frac{4K}{R^2}\right)\frac{v_{ti}^2}{\omega_{ci}} = 4x10^3 \frac{KT_i(\text{eV})}{R^2(\text{eV})B_e(\text{T})} \ \text{s}^{-1} , \qquad [4.12]$$

with K = 1, is $5.5x10^4$ s^{-1}, which is about 30% lower than the observed ion rotational speeds of $\omega_i \sim 7x10^4$ s^{-1} at the onset of the n = 2 rotational instability. This is consistent with the critical threshold for the rotational instability predicted by the single fluid MHD model, i.e., $\omega_i/\omega^* \sim 1$-2. It is unclear why the shorter antennas allow more stable operation. It is possible that the higher temperature obtained with the shorter antennas increases ω*, thus delaying the onset of the n = 2 rotational modes, as the ion rotation is limited to about $7\times10^4\ s^{-1}$ for nearly all the RMF driven FRCs obtained in TCS.

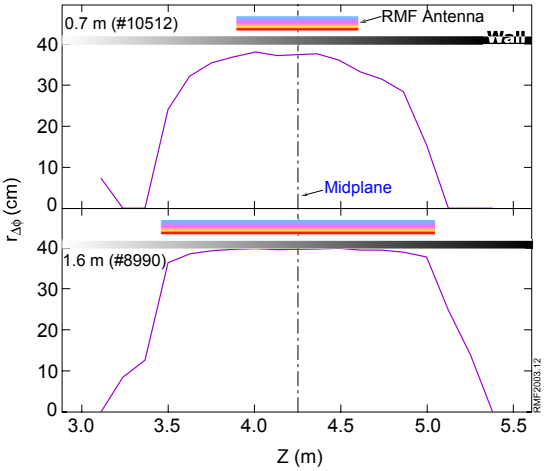

Figure 4-62. Excluded flux radius $r_{\Delta\phi}$ versus axial distance Z at 1 msec for two comparable FRCs produced at similar RMF fields and frequencies, but with

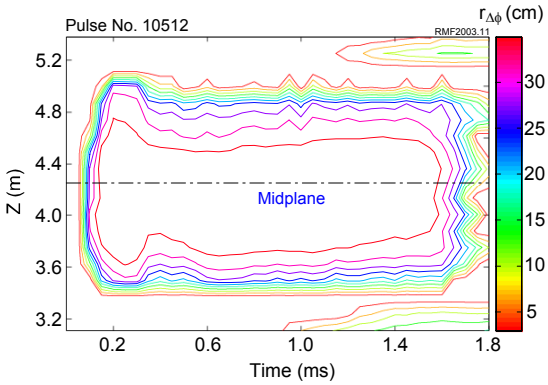

Figure 4-63. Evolution of excluded flux radius ($r_{\Delta\phi}$) profiles of the FRC (#10512), produced with the 0.7-m long antenna.

One unexpected result from the operation with different antenna lengths is that the length of the FRC appears to be only weakly dependent on the length of the RMF antenna, as illustrated in Fig. 4-62. The shape of the separatrix, as indicated by the measured excluded flux radius, $r_{\Delta\phi}$, appears to be elliptical for the FRC produced with the shorter antenna (0.7-m long), but racetrack-like for the discharge obtained with the 1.6-m

long antenna. In the shorter antenna case, the FRC extends axially far beyond the antenna with the FRC length reaching nearly two times the antenna length. This is not unexpected for an FRC where the toroidal currents are diamagnetic, but it is interesting how the RMF manages to sustain the currents everywhere despite the drive torque only being applied near the center. The configuration is sustained for the entire duration of the applied RMF, which was switched off at 1.5 ms, as shown in Fig. 4-63.

Based on the generalized Ohm's law, the azimuthal electric field, E_θ, driven by the RMF, can be written as

$$E_\theta = \eta_\perp j_\theta + \left\langle -\tilde{v}_{ez}\tilde{B}_r \right\rangle + V_r B_Z - V_Z B_r \qquad [4.13]$$

where $\left\langle -\tilde{v}_{ez}\tilde{B}_r \right\rangle$ is the RMF drive term. B_z and B_r are the axial and radial components of the steady confinement fields, j_θ is the azimuthal current, V_z and V_r are the axial and radial flow velocities (assuming $\mathbf{V}_i = \mathbf{V}_e = \mathbf{V}$). In steady state, E_θ must be zero everywhere. The azimuthal current outside the antenna can only be sustained by the local plasma flow, *i.e.*, $(-j_\theta) = (V_r B_z - V_z B_r)/\eta_\perp$.

A possible flow pattern is illustrated in Fig. 4-64. Besides the normally postulated swirling flow (to balance the central inward V_r), there is also diffusion of plasma across field lines at the end, which can account for the measured particle confinement times. The elliptical shape accentuates the $V_z B_r$ term. The RMF drive term must be stronger in order to produce a larger inward flow velocity.

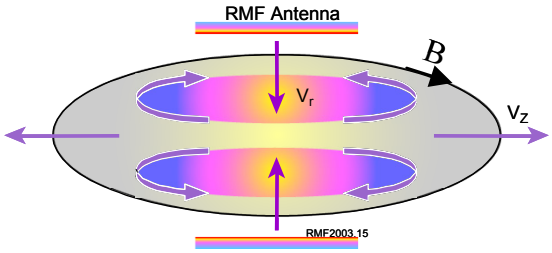

Figure 4-64. Sketch of plasma flow that could be present inside an RMF driven

To test the above hypothesis, we have carried out an experiment with the RMF antenna extending axially to cover the entire TCS confinement chamber of ~ 2.6-m. In this case, the RMF should drive an inward flow everywhere and inhibit the swirling flow to the outer field lines. Figure 4-65 shows the time evolution of the axial profiles of excluded flux radius of two shots obtained with the 2.6-m long antenna, *i.e.*, #10600 with normal end field configuration and #10620 with nearly doubled end field strength. Profiles of an FRC with the 1.6-m long antenna are shown for comparison. The end field configuration makes little difference for the long antenna, except at start-up, since the FRC quickly shrinks to an even shorter separatrix length than for the 1.6-m antenna. This might be related to inhibition of the swirling flow at the ends, which somehow reduces particle lifetimes.

More results are shown in Fig. 4-66 for the two comparable shots with the 2.6-m and 1.6-m long antennas, i.e., #10600 and #10204, respectively. The maximum magnetic field, B_e, that can be sustained by the RMF is similar for the two discharges. The line integrated density, $\int n d\ell$, is also similar except for the initial formation phase, which is dependent on the gas fuelling rate and the bias field configuration. However, the particle

confinement time, τ_N, as deduced from D_α measurements, is significantly reduced in the longer antenna case, most likely due to the restriction of the swirling flow around the FRC ends. In the figure are also shown the measured RMF heating power P_{abs}, together with the loss power P_{loss}, determined from a 0-D model for particle and power balance.

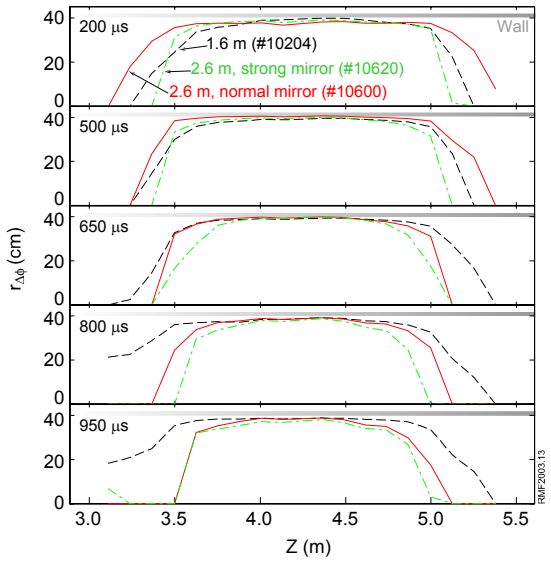

Figure 4-65. Excluded flux radius, $r_{\Delta\phi}$, versus axial distance Z for two FRCs formed with the 2.6-m long antenna, but with the different end mirror fields: #10600 with normal end field configuration, #10620 with nearly

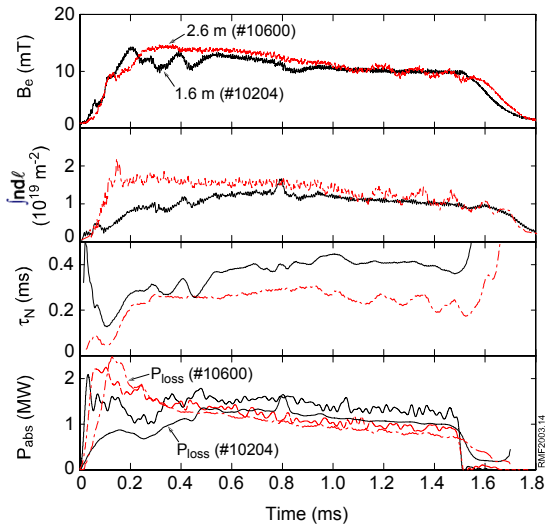

Figure 4-66. External magnetic field, B_e, line integrated density, $\int n d\ell$, measured at the midplane and absorbed power, P_{abs}, for two comparable FRCs produced with the 2.6-m long and 1.6-m long antennas. Particle confinement time τ_N and loss power $P_{\ldots}$ from a global particle and

Detailed contributions from the different loss channels, including radiation P_{rad}, conduction P_{cond}, convection P_{cond}, charge-exchange P_{cx}, and ionization P_i losses, are shown in Fig. 4-67. The power losses related to the recycling processes (P_{conv} + P_{cx} +P_i) are significantly increased in the discharges obtained with the 2.6-m long antenna, compared to the cases where $\ell_s > \ell_{ant}$, at reduced antenna lengths, as shown in Fig. 4-68. It is to be noted that the simple 0-D model cannot account for all the power losses in the cases where the FRC lengths are sufficiently longer than the RMF antenna length, which is at least in part due to inhomogeneity of the FRCs at the ends, as shown in Fig. 4-69.

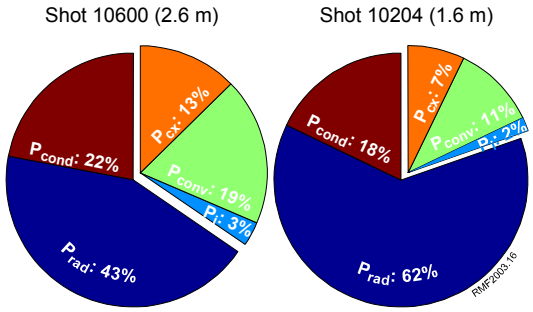

Figure 4-67. Comparison of power losses from various channels for the 2.6-m and 1.6-m long antennas

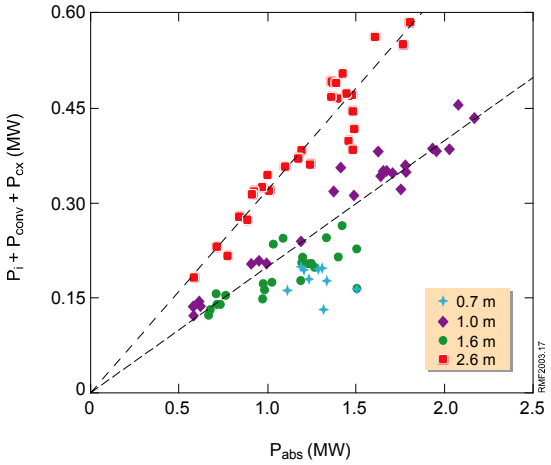

Figure 4-68. Power losses from ionization, convection and charge-exchange ($P_i + P_{conv} + P_{cx}$) versus the total absorbed power P_{abs} for different

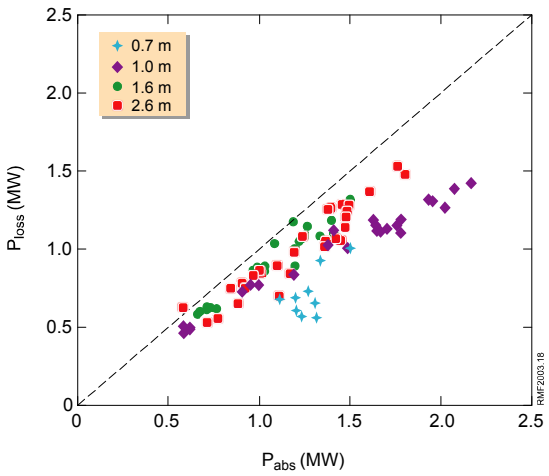

Figure 4-69. Total power losses P_{loss} versus the total absorbed power P_{abs} for different antenna lengths.

In summary, reducing the antenna length has led to more stable operation and a significant increase in plasma temperature. The FRC can be sustained far beyond the axial extent of the RMF antenna, presumably due to the presence of an axial flow. As a result, the plasma density that can be achieved at a given RMF field strength is somewhat reduced, especially in the shortest antenna case (0.7-m long), because the RMF torque in the center must balance the resistive torque over the full FRC. The axial internal field $B_Z(r)$ profile remains nearly identical for all the different antenna lengths. However, the FRCs obtained with the shorter antennas exhibit a more expected RMF $B_\theta(r)$ profile, with greater RMF penetration. Finally, the operation with the antenna extending over the full TCS confinement chamber has caused the FRC to shrink axially, resulting in a significant reduction in the particle confinement time, which may be due to hindering the swirling flow around the FRC ends required in our MHD calculations.

V. FRC TRANSLATION EXPERIMENTS

As described in Section 4, FRCs can be formed in the TCS confinement chamber from a pre-ionized deuterium gas using the rotating magnetic field (RMF) alone, and have been sustained in steady state by RMF. However, these FRCs are limited to sub-100 eV temperature by impurity radiation. Hot FRCs can be obtained in the present TCS machine by translating a hot FRC from LSX/mod. As a prerequisite for the sustainment of translated FRCs by the RMF, the electron density of the preformed FRCs must be sufficiently low so that the RMF torque can exceed the electron-ion frictional torque. In addition, the radiative losses resulting from impurity pick-up during the translation and capture process must be minimized so that the RMF heating is sufficient to balance the total power losses, including convection, conduction and charge-exchange losses.

5.1 Basic Operation

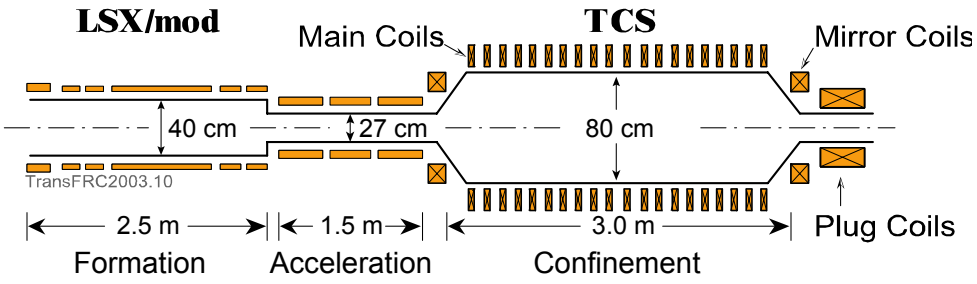

Figure 5-1. Schematic of TCS with LSX/mod attached.

Details of the TCS facility are described in Section 3, but a sketch of TCS with LSX/mod attached, is shown in Fig. 5-1. FRCs are formed in the 2.5-m long, 0.4-m diameter LSX/mod, by the conventional field reversed theta pinch (FRTP) method, at fairly low deuterium puff fill pressures (compared to high fill pressure operation for TRAP applications). The theta pinch capacitor banks are either charged to a nominal voltage of ±20 kV (high energy) or half voltage, ±10 kV, (low energy). Although the peak fields that can be obtained at these conditions are 1.0 and 0.5 T, the FRCs are ejected before these peak fields are reached, at either 0.45 T (high energy) or 0.3 T (low energy). LSX/mod field reversal is called time zero. To minimize neutral pressure in the TCS confinement chamber, a deuterium gas puff is introduced from the upstream end of the source, typically 10 ms before starting the formation process, so that neutrals do not have enough time to reach the confinement chamber. The initial FRCs have typical conditions of n_e = 6×10^{20} m^{-3}, T_t = 900 eV, and ϕ_p ~ 2 mWb (high energy) or n_e = 6×10^{20} m^{-3}, T_t = 400 eV, and ϕ_p ~ 1.5 mWb (low energy). The poloidal flux, ϕ_p, is estimated from the measured excluded flux, $\Delta\phi$, by the Rigid Rotor (RR) approximation $\phi_p = 0.31 x_s \Delta\phi$. $x_s \equiv r_s/r_c$ and r_s is generally taken to be the excluded flux radius $r_{\Delta\phi} = \sqrt{\Delta\phi/(\pi B_e)}$ where B_e is the external axial field at the flux conserver boundary. The commonly used kinetic parameter

$$s = \int_R^{r_s} \frac{rdr}{r_s \rho_i} = 1.56 \frac{\phi_p(\mathrm{mWb})}{\mathrm{r_s(m)}\sqrt{A_i T_i(\mathrm{eV})}} \qquad [5.1]$$

was about unity for either case. FRCs are MHD unstable to an internal tilt and observed experimental stability has generally been attributed to a *reduction*, but not elimination, of the MHD growth rate at low s.

The FRCs are translated out of LSX/mod by having a higher external field at the upstream end. There are 4 independently driven 0.23 m diameter single-turn fast coils, including 2 main coils and 2 plug coils installed at both ends. These coils are sequenced to initiate the acceleration process. The FRCs are then accelerated through a 1.65-m long, 0.27-m diameter quartz drift section by three successively energized three-turn coils. Transition to the much smaller diameter acceleration section was specially designed for the previous TRAP experiment, but is not desirable for TCS experiments, as this may lead to strong local interactions with the quartz tube wall during translation and after reflection from the downstream end of TCS. The FRC is finally expanded into the 2.5 m long and 0.8 m diameter quartz confinement chamber where a low bias field is present, resulting in low density FRCs that are desirable for RMF current drive. The optimal bias field in TCS was about 50 mT, with higher fields resulting in smaller radius and shorter lived FRCs, and lower fields exacerbating wall contact and also resulting in shorter lived FRCs.

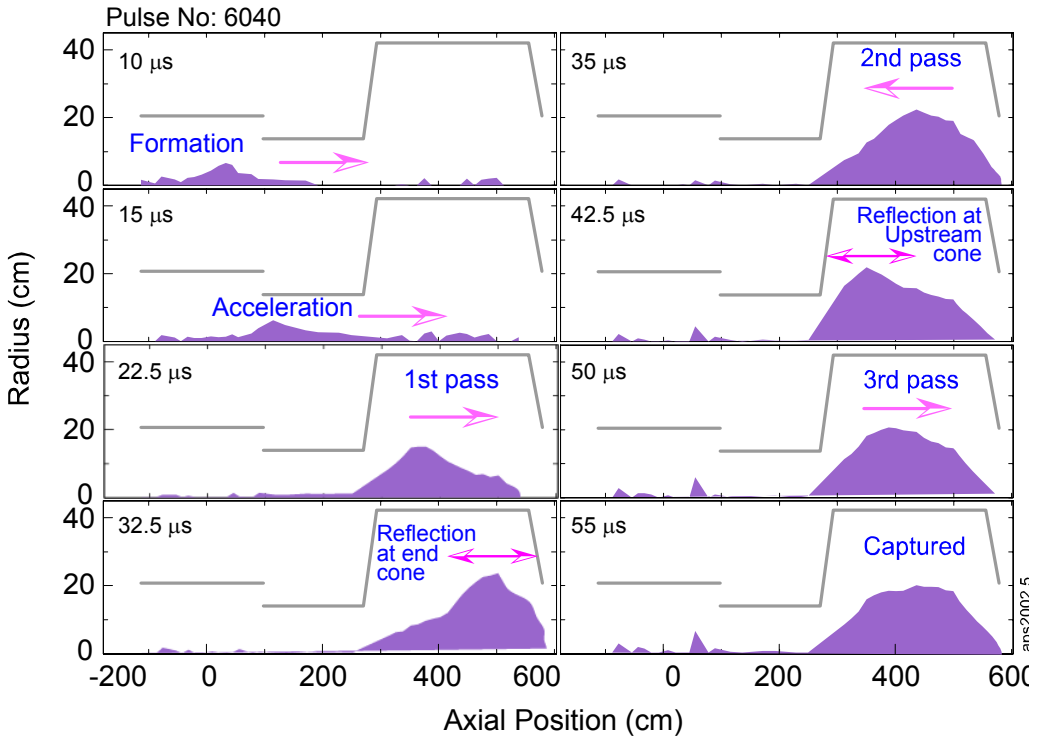

Figure 5-2. Time evolution of the excluded flux radius $r_{\delta\phi}$, illustrating the dynamics of translation.

The evolution of a translated FRC is shown in Fig. 5-2, where the excluded flux radius is plotted versus axial position at several selected times during translation. As can be seen, the FRC expands into the TCS confinement chamber at about 22 μs, and impinges at the downstream end mirror at about 32 μs, at a highly supersonic speed of about 400 km/s. It is remarkable that the FRC can survive such a violent interaction with the end cone during the reflection process. The FRC then continues to undergo a few reflections off the upstream and the downstream mirrors before finally being captured in the TCS confinement chamber.

5.2 Flux amplification

In order to achieve a good first reflection and a long lived FRC it was found necessary to not activate the TCS mirror coils shown on Fig. 5-1. Thus, the FRC would interact directly with the 45° end cone. The reasons for this requirement are not known, but it is remarkable that the FRCs can survive such a violent reflection in the first place. The inner portions of the downstream end cone were covered with a tantalum insert, extending a few inches into the 27-cm diameter end tube, which eliminated noticeable ablation of the uncovered stainless steel.

A common feature of all data obtained with optimal magnetic field profiles at the downstream end cone was the large increase in diamagnetism occurring after the first reflection, as previously seen in a very similar FRC translation-expansion facility, FIX (FRC Injection Experiment) at Osaka University.[22] The low diamagnetism on the first pass, and subsequent increase, is not due to simple two-dimensional dynamics, and cannot be duplicated using 2-D numerical codes. A typical time history of the diamagnetism inside TCS is shown in Fig. 5-3. Mesh plots are shown from two viewpoints to illustrate both the entrance behavior and the settling down to an equilibrium FRC. The axial distance refers to the distance from the upstream end of LSX/mod, and the time contours are 2.5 μsec apart. Eighteen diamagnetic loops are located about 12.5-cm apart, except at the center of TCS (Z = 4.25 m) where a gap exists to provide access for an interferometer, bolometers, and internal probes. The FRC enters TCS at about 25 μsec and rapidly traverses the 2.65-m between end cones in about 7 μsec. There are two obvious reflections before it settles down. A large increase in diamagnetism (column cross-section) is evident after the first pass.

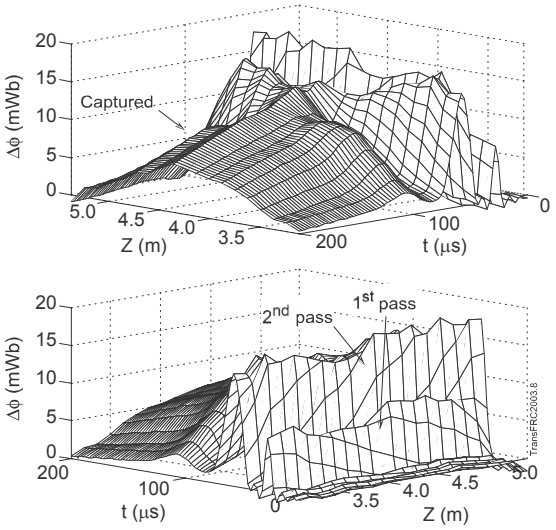

Figure 5-3. Diamagnetism time histories inside TCS.

Time histories of $\Delta\phi$, B_e, and interferometer line density, $\int nd\ell$, for several shots are shown in Fig. 5-4. Small variations are seen from shot to shot, partially due to small changes in operating conditions, and partially due to variations in the reflection processes. Although the end mirror coils on TCS were not activated, a slight mirroring was provided by having slightly more current to the independently powered main field coils on either end (CMP). Similar behavior was seen on the FIX device where the recovery to a long lived FRC was dependent on the downstream mirror ratio not being too high. However, it is essential to provide sufficiently high fields at the downstream end by the plug coils to stop the translated FRCs. The internal probe was inserted radially at the center of TCS, up to 12 cm past the axis. There was essentially no difference between shots without the probe except that the best shots without the probe had a slightly longer lifetime. The 31 magnetic loops inside a 5 mm diameter BN tube could be oriented to record either $B_z(y)$ or $B_x(y)$.

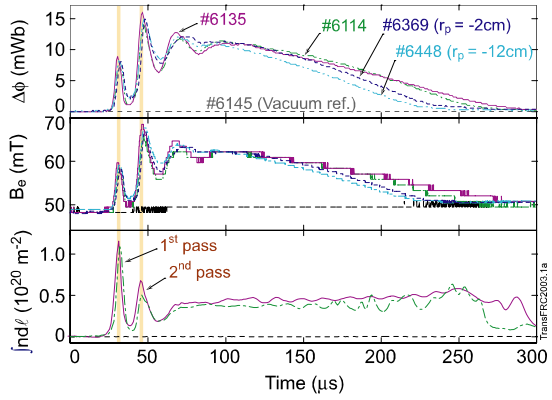

Figure 5-4. Time histories of basic data for several injected FRCs. The furthest insertion of the internal probe, from r = 40 cm to r_p,, is also indicated. Note that $\int nd\ell$ is not available for the discharges with the probe inserted past the axis, which blocked the CO_2 laser beam.

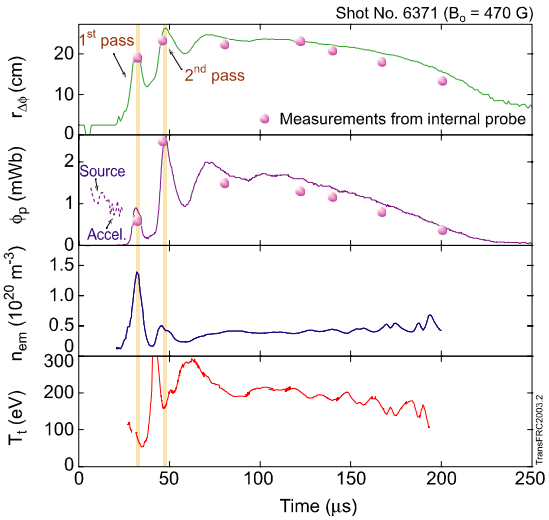

Figure 5-5. Properties of a translated FRC. The separatrix radius (r_s) and the poloidal flux (ϕ_p) were determined from the internal probe inserted 2 cm past the axis. The peak density (n_{em}) and the total

Time histories of various properties of a translated FRC are shown in Fig. 5-5. The peak density n_{em} is related to the average density by dividing by $\langle\beta\rangle = 1 - 0.5x_s^2$ as is appropriate for FRCs. The total temperature was calculated from pressure balance as $T_t = B_e^2/(2\mu_o k n_{em})$. The FRC cools significantly upon expansion from its initial formation conditions, but recovers most of this temperature due to the non-isentropic reflection off the downstream mirror. The dashed line in the poloidal flux trace shows the time history of the peak poloidal flux as measured by flux loops in the formation and accelerator sections. Based on the RR formula there may be some loss of poloidal flux upon entrance into TCS, but the poloidal flux appears to recover to an even higher value after the first reflection. This is a typical behavior. Poloidal flux values measured with the internal probe are also shown at selected times when the FRC was centered over the

probe. These values should be lower than those calculated from the RR formula since the measured excluded flux also includes contributions from open field line plasma. The kinetic *s* values based on these values before and after the first reflection, and in the equilibrium phase (around 100 μs) are 0.5, 1.2, and 0.8, respectively, assuming $T_i = T_e = T_t/2$.

5.3 Internal Field Profiles

Internal field measurements were difficult to make accurately for translated FRCs in TCS due to the tendency of the FRC to not travel down the centerline of the plasma chamber. A technique was thus adopted to utilize the 5-fan (6-12 elements per fan) visible tomography system which, although too crude to measure overall structure, was able to determine when the FRC was centered (right and left) on the probe, and where the center was (up and down). A series of tomographic reproductions is shown in Fig. 5-6 for the shot used to obtain the internal poloidal field data points shown on Fig. 5-5.

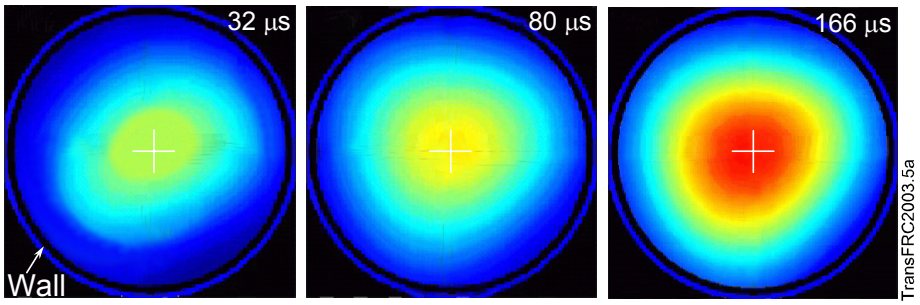

Figure 5-6. Tomographic reconstructions for shot #6371. Data was taken at 32, 80, and 166 μs.

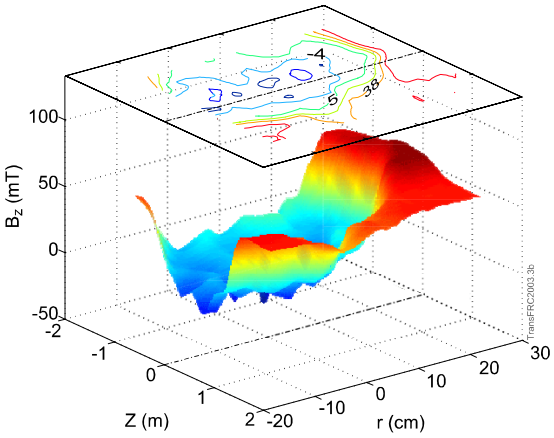

Figure 5-7. $B_z(r,Z)$ the first pass through TCS, with Z = 0 being the FRC center. The data was taken from pulse 6442 with the probe inserted 12 cm past the axis.

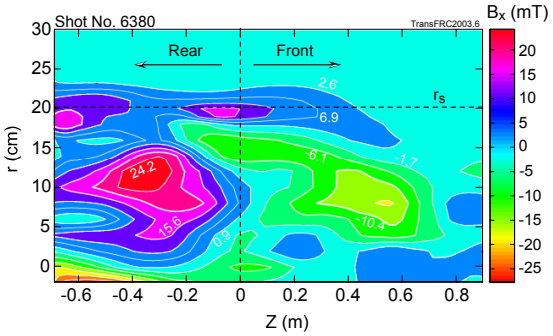

Figure 5-8. $B_x(r,Z)$ profiles on the first pass through TCS.

An FRC only remained centered on the internal probe for its full pass during the first pass. The time histories of the magnetic fields during this pass could be converted into plots versus distance by using the observed transit velocity. Such a plot of $B_z(r,Z)$ is shown in Fig. 5-7. A very shallow reversal of the poloidal field was consistently observed on the first pass. However, strong toroidal fields were observed, as shown, for example, in Fig. 5-8.

Radial profiles of $B_z(r)$ and $B_x(r)$ are shown in Fig. 5-9 at the front, middle, and back of the 'FRC' during its first pass, and near the center of the FRC (whenever tomography showed good right-left centering) during the second pass, and during the equilibrium phase. Deviations are shown for periods corresponding to short intervals within which the FRC was well centered on the probe, and where it was axially centered within ±0.5 m, and over several similar discharges.

Profiles such as those shown in Fig. 5-9 were used to place the ϕ_p points on Fig. 5-5. It can be seen that there is very little poloidal flux on the first pass, even less than would be calculated based on the RR expression. Assuming B_x represents a toroidal field, there also appears to be toroidal flux in opposite directions at the front and rear of the FRC. This has been seen in numerical calculations,[23,24] and was ascribed to the Hall term, $\nabla\times\mathbf{v}_e\times\mathbf{B}$, with an initial growth rate, $\partial B_\theta/\partial t \sim \partial v_\theta/\partial z$, dependent on the axial distribution of the toroidal current. The B_x profiles measured by the probe indicate a B_θ in the ion-drift direction at the front, corresponding to a peaked toroidal current profile toward the middle of the FRC (elliptical shape), with the highest toroidal field at the rear in the electron-drift direction, consistent with the direction of toroidal field seen in other FRC translation experiments.[25] It is possible that the FRC has tilted somewhat, but the first pass profiles (Figs. 5-7 and 5-8) are not consistent with a simply tilted FRC.

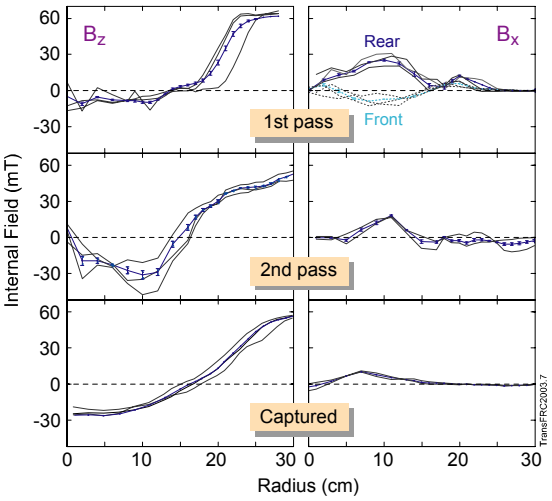

Figure. 5-9. Radial profiles of axial and toroidal fields for first pass, second pass, and equilibrium FRC. Solid lines represent the averaged profiles with standard deviations indicated.

The features of the magnetic fields during the second pass (after the first reflection) are also somewhat bizarre. There appears to be an azimuthal ring of poloidal flux, signifying toroidal currents flowing in opposite directions. Probe insertion past the axis has clearly shown that the B_z profiles are axi-symmetric about the r = 0 point shown on Fig. 5-9. To illustrate this, Fig. 5-10 shows the profile of $B_z(r,t)$ measured by the internal probe inserted 12 cm past the axis for the FRC during the second pass through TCS (after being reflected off the downstream end mirror). Such profiles are sometimes seen during phases of FRC theta-pinch formation when some forward flux is trapped by ringing

preionization, but it is not clear how such a profile would occur due to FRC reflection. Most of the oppositely directed toroidal flux has also been annihilated, with only a reduced amount of net unidirectional flux remaining.

The truly remarkable feature of the entire process is that after the second (upstream) reflection, the plasma appears to be in a normal FRC configuration. The measured poloidal flux agrees with the RR value obtained from diamagnetism, and is substantially higher than that present during the first pass, presumably arising from the conversion of some toroidal flux during the reflection processes.

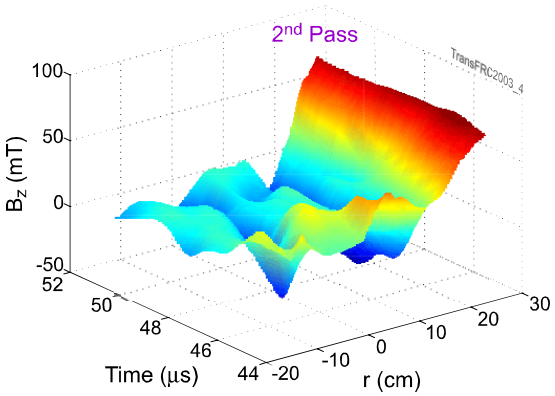

Figure 5-10. $B_z(r,t)$ on the second pass through TCS, with Z = 0 being the FRC center. The data was taken from pulse 6442 with the probe inserted 12 cm past

5.4 Flux lifetime

The flux lifetime, τ_ϕ, of the captured FRCs is strongly dependent on the TCS bias field. Lower bias fields result in increased r_s, improving the lifetime, as τ_ϕ normally scales as r_s^2. However, if the bias field is too low the interaction with the quartz chamber walls leads to large impurity influxes, hence, strong radiative power losses, thus affecting the FRC lifetime. Figure 5-11(a) shows the lifetime of captured FRCs as a function of the bias field, B_o, for the FRCs produced in the LSX/mod source at either high energy (0.45T) or reduced energy (0.3T). It can be seen that the optimum bias field is lower for lower energy translated FRCs. In both cases, the lifetime is significantly reduced at low bias fields. In contrast, FRCs obtained from FIX had a much better lifetime at similar (low) bias fields,[17] probably ascribed to its metal chamber. The lifetime of the translated FRCs is compared with the high density LSX scaling of

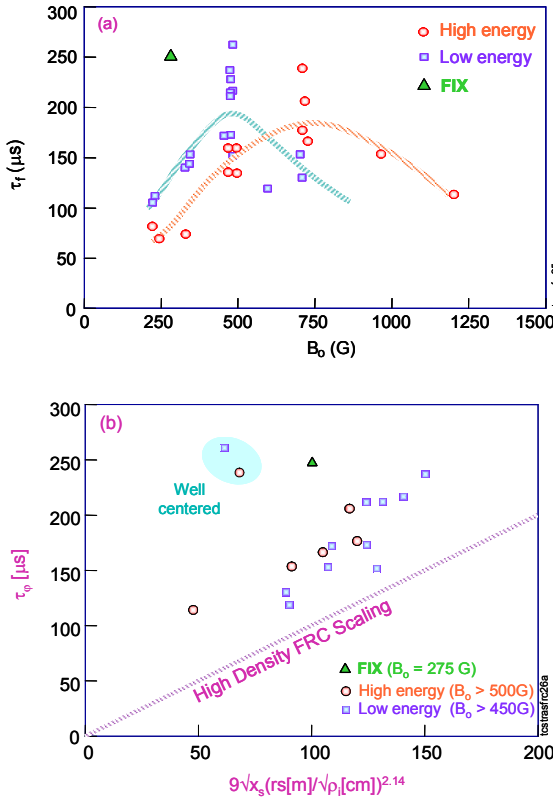

Figure 5-11. Flux lifetime of translated FRCs, τ_ϕ , versus (a) bias fields B_o; (b) predictions from high density conventional FRC scaling. A data point from FIX

$\tau_\phi(ms) = 9x_s^{0.5}\{r_s(m)/\sqrt{\rho_i(cm)}\}^{2.14}$,[16] in Fig. 5-11, except for the cases with low bias fields that are tarnished by impurity influxes. It appears that the flux lifetimes of the optimal low density translated FRCs are better than predicted by the high density FRC scaling. In particular, the very best lifetimes, obtained with the most well centered FRCs, have lifetimes about three times higher than the LSX scaling, very similar to the best results obtained on FIX.

5.5 Impurities

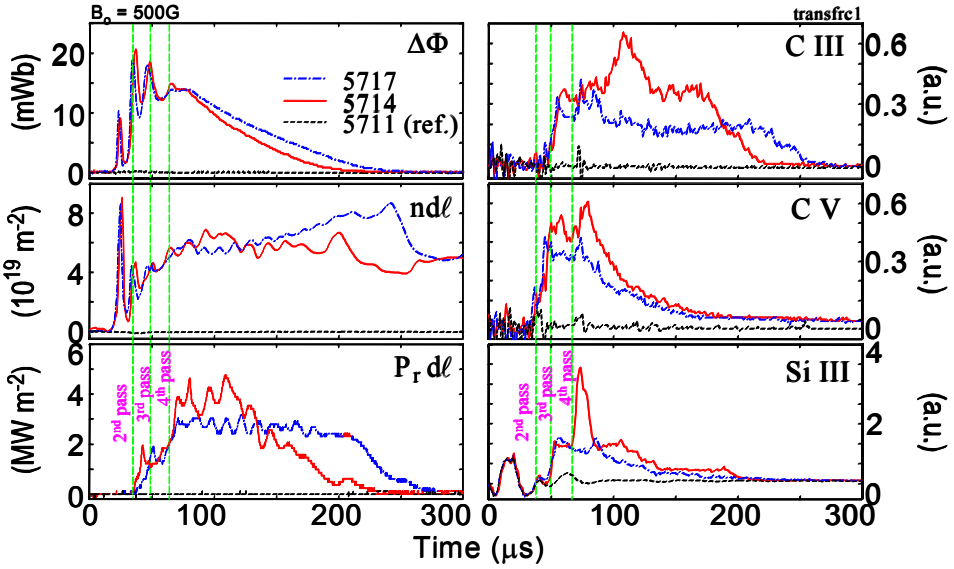

Figure 5-12. Comparison of two translated FRCs, #5714 (off centered) and #5717, together with the reference pulse, 5711, to illustrate the influence of impurity influxes as indicated by various impurity line intensities (CIII, CV and SiIII) on the

As one might expect, the interaction of energetic FRCs with the end cones and the quartz plasma vessel walls results in impurity production, thus affecting FRC performance, especially when the FRC is not well centered. As an example, Fig. 5-12 shows some impurity line emissions, CIII, CV and SiIII, for two discharges. Pulse 5717 is well centered, while pulse 5714 is slightly off-center. In both cases, impurity production at the first impact of the FRC upon the end cone at the far end is effectively eliminated by use of the tantalum shield, in spite of extremely violent interactions. Both SiIII and CIII are observed after FRC impingement on

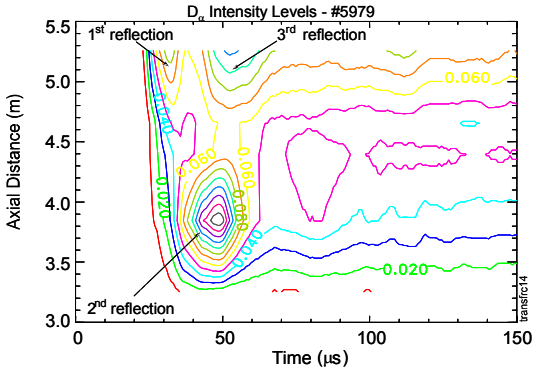

Figure 5-13. Contour of $D_\alpha(Z,t)$, illustrating localized emission near the upstream cone upon the second reflection.

the upstream cone (with only bare stainless steel), probably due to the uncovered quartz tube upstream of the cone. FRC impact also leads to strong deuterium influx at the upstream cone (shown in Fig. 5-13). For the FRC which is not-well centered (#5714), silicon ablation is observed, which leads to stronger radiation and shorter flux lifetime.

We generally operated at half the normal LSX/mod charge voltage (low energy) in order to reduce the dynamics of translation. The resultant FRCs had a lower translation speed of about 250 km/s, thus reducing impurity production rate, and hence radiation losses during the capture process of translated FRCs, as shown, for example, in Fig. 5-14. Note that the total temperature of captured FRCs formed at lower energy was similar to that of FRCs produced by the higher energy source, in spite of initial lower temperatures. This was mainly due to reduced radiation losses. The FRC lifetime was significantly improved for the lower source energy, especially in discharges with low bias fields (~50 mT), hence large separatrix radius, where interactions of the FRCs with the wall were strong.

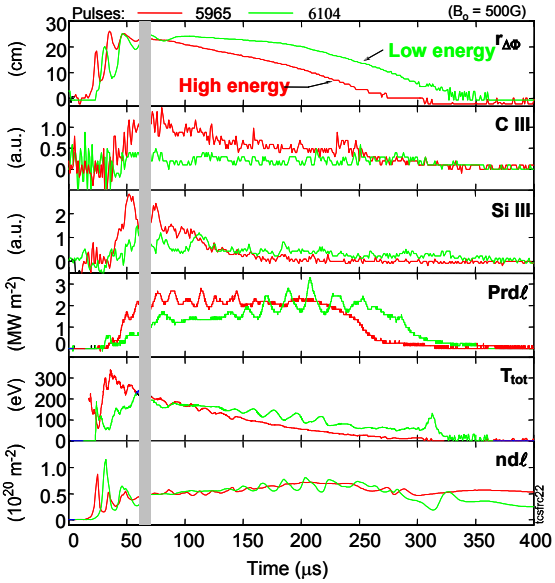

Figure 5-14. Time traces of midplane quantities for two comparable discharges

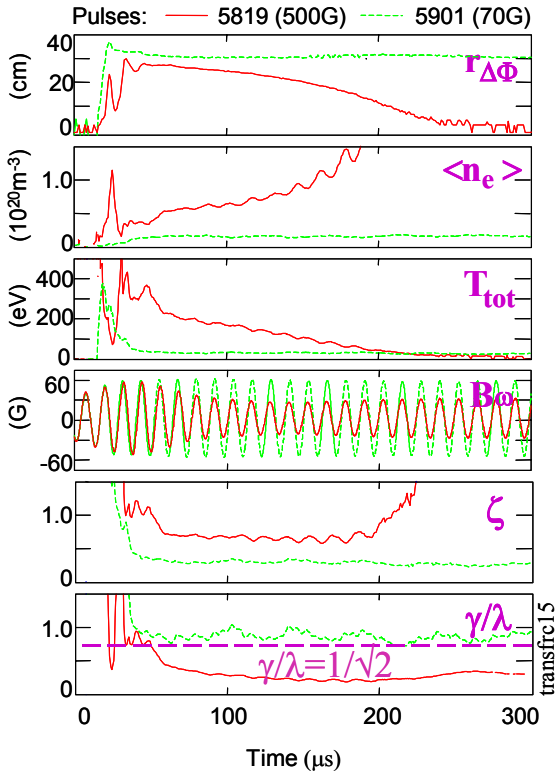

Figure 5-15. Application of RMF to two typical translated FRCs with different confinement fields – 5819 at 500G, 5901 at 70G, with RMF frequency at 0.5×10^6 s^{-1}

5.6 Flux Sustainment by RMF in Translated FRCs

We have conducted some RMF drive experiments on the translated hot FRCs. The optimal translated FRCs, with a confinement field of about 50 mT for example (see pulse 5819, as shown in Fig. 5-15), would be ideal for RMF sustainment. However, strong interactions of the energetic FRCs with the plasma quartz vessel walls led to quartz ablation and strong impurity influxes. The resultant cold and dense edge plasmas caused significant resistive loading of the RMF antennas and dramatically reduced the

RMF field strength B_ω, thus rendering the RMF drive force insufficient to overcome resistive friction.

Even with wall ablation, FRCs could still be sustained at low bias fields (pulse 5901 in Fig. 5-15), but wall interaction during the capture processes greatly lowered the temperature to RMF start-up levels. In spite of insufficient drive at high bias, RMF proved to be effective at stabilizing rotational modes and centering the FRC, thus extending lifetimes. In addition, Doppler spectroscopy showed that the ions were dragged along with the RMF, rotating in the electron diamagnetic direction at the edge. This is opposite to the rotation direction of ions, i.e., ion diamagnetic direction, in the translated FRCs without RMF applied. Rotation data are shown in Fig. 5-16. Note that the ion rotation speed was significantly slowed down near the edge in the discharge without the RMF applied, presumably due to the viscous drag of the FRCs on the wall, as the FRC was not well centered in this case.

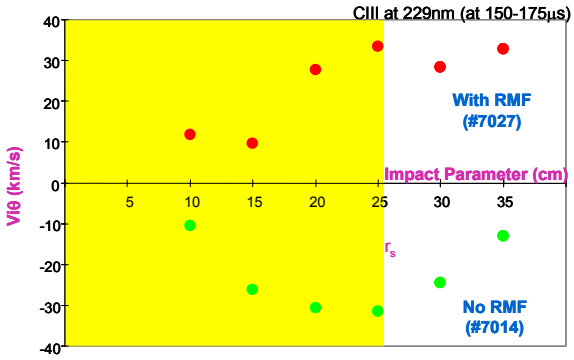

Figure 5-16. Comparison of the rotation rates of C^{++} in the captured FRCs with and without the RMF applied. $B_\omega = 50$ mT

5.7 Summary

RMF flux build-up could not be utilized on the translated and captured FRCs due to an ablative gas layer formed by reflection of the highly energetic plasmoid off quartz surfaces, but extremely interesting results were obtained for the translation and capture process. In particular, the strange occurrence of an increase in FRC excluded flux and radius upon supersonic reflection is seen to be due to a substantial increase in poloidal flux, which is probably related to the loss of net toroidal flux. The details of the reflection and capture process are complex and not fully diagnosed, but the significant fact is that the end result is a normal stable FRC with relatively long lifetime. This is a tribute not only to the robustness of FRCs, at least at low s, but also to the tendency of an FRC to be a preferred state for a magnetized plasma,[26] much as for spheromaks with preserved helicity.

VI. FUTURE PLANS

The program described in this final report has successfully demonstrated the generation and sustainment of FRCs by RMF. The basic physics of the process is also fairly well understood. RMF current drive appears to be a very rugged process, automatically adjusting to the FRC parameters in terms of penetration depth as long as the drive torque can exceed the resistive torque. The process also does not seem to be very sensitive to antenna placement or length. The major need now is to operate at higher temperatures.

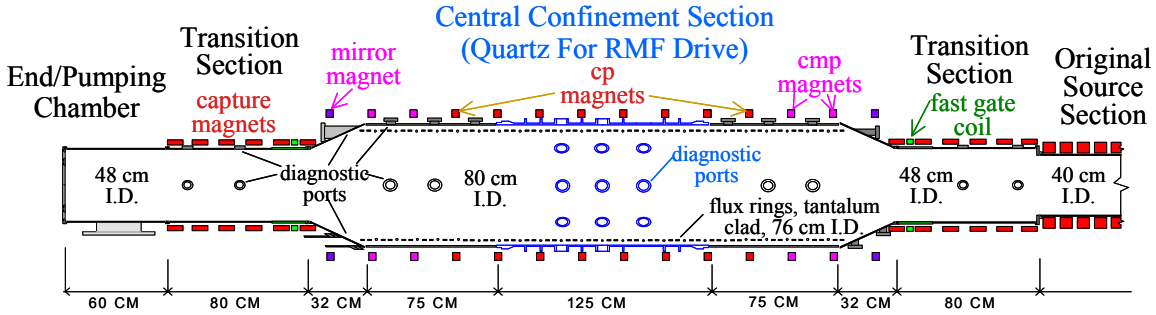

Figure 6-1. Expected plasma conditions in TCS/mod for RMF formation.

It is thought that plasma temperatures are limited by radiation barriers resulting from high impurity content. Since RMF drives flow inward, it is essential that the plasma vessel have clean walls free of impurity monolayers. Major modification are being made to TCS to utilize all metal construction wherever possible, eliminate the use of greased "O"-rings, and allow for baking and wall conditioning. A central insulating section is needed to allow for RMF penetration, and we will utilize a single 80-cm diameter, 1.25-m long quartz section. This will allow RMF antenna lengths of up to 1.25 meters. It is shown in Section 4.11 that about a 1-m antenna length is ideal for the TCS device. The quartz walls will be protected by internal flux rings with an L/R time of about 6 msec. The remainder of the approximately 2.65-m long TCS chamber will be stainless steel. A sketch of the modified facility, as it is now being designed, is shown in Fig. 6-1.

The flux rings will be placed at about a radius of r_c = 37 cm and made from thin aluminum strips, about 0.6 mm thick and 3 cm wide. They will be placed on 6-cm spacings, allowing 3-cm gaps for RMF penetration. The rings will be covered with 5-mill tantalum extending back to the plasma tube wall at r_w = 40 cm to make it difficult for plasma to reach the quartz surface. They will also cover the stainless steel portion of the chamber.

We wish to be able to bake the system to about 200°C. The most difficult part of the design is to seal the quartz tube to the metal sections. This will be done with special bellows sections that are glued onto the quartz. We are investigating various high temperature, high vacuum epoxies. The same technique will be used on a modification of the LSX/mod formation section and the diagnostic ports sketched on Fig. 6-1.

We also wish to be able to use TCS in the FRC translation mode in order to start with higher density, higher temperature, lower resistivity plasmas. It is thus essential to eliminate FRC contact with quartz wall. The old 27-cm diameter quartz acceleration section between LSX/mod and TCS will thus be replaced by a 48-cm diameter stainless steel tube with quasi-steady, multi-turn coils. The conical sections on TCS will also have a much gentler angle then the previous 45°. The overall design will be very similar to the Osaka FIX machine, except that the FRC formation section will be considerably larger to allow for the creation of higher flux initial FRCs.

Table 6.1
Expected plasma conditions in TCS/mod for RMF formation

ω (10^6 s^{-1})	ωr_s^2 ($s^{-1}m^2$)	B_ω (mT)	n_{em} ($10^{20}m^{-3}$)	T_t* (eV)	B_e (mT)	$\eta_\perp$ ($\mu\Omega$-m)	λ	P_{abs} (MW/m)
0.5	0.055	7	0.30	90	33	94	19	3.3
0.7	0.078	5	018	110	28	77	25	1.9
1.0	0.111	5	0.15	185	33	64	33	2.1
1.4	0.157	5	0.125	310	40	51	44	2.4

In the RMF formation mode we can estimate the obtainable conditions from the previous density scaling, plus assuming that the temperature can increase up to a limit set by $\zeta < 1$. Using the scaling of Eq. (2.11), the total temperature is given, in terms of ζ as

$$T_t(\mathrm{eV}) = \left(790\langle\beta\omega r_s^2\rangle\zeta\right)^2 n_{em}(10^{20}\,\mathrm{m}^{-3}) \ . \qquad [6.1]$$

If we use the empirically observed density scaling of Eq. (4.1), $n_{em}(10^{20}m^{-3}) = 0.01B_\omega(\mathrm{mT})/(\omega r_s^2)^{1/2}$, and assume some value of ζ, we can arrive at a possible temperature. These values are shown in Table 6.1 for r_s = 33 cm and various RMF magnitudes and frequencies for a chosen value of $\zeta = 0.67$*. The listed values of $\eta_\perp$, λ, and P_{abs} correspond to the resistivity scaling $\eta_\perp = 570(B_\omega/B_e)^{1.16}$ discussed in Section 4. If the actual resistivities are higher, but the listed densities can still be achieved, the absorbed power will be higher. Since we expect FRCs only slightly longer than 1.0 m, and the available peak RMF power is about 5.0 MW, there is some leeway in that direction.

The FRC flux levels, about 0.1 mWb per mT of B_e, are still fairly low in Table 6.1 compared to what would be desirable if we wished to add neutral beam current drive. The only way to operate at higher flux levels, without going to unavailable values of ω and B_ω, is to operate at higher density, which requires lower values of plasma resistivity. These conditions have been seen in the translated FRCs, which is why this capability is being kept in the program.

V. REFERENCES

1. A.L. Hoffman, et al, "*The Large s Field-Reversed Configuration Experiment* ", Fusion Technology **23**, 185 (1993).
2. A.L. Hoffman, et al, "*Inductive FRC accelerator for tokamak refueling*", Fusion Technology **36**, 109 (1999).
3. M. Tuszewski, "*Field Reversed Configurations*", Nuclear Fusion **28** (1988) 2033.
4. T.R. Jarboe, "*Review of spheromak research*", Plasma Phys. Controlled Fusion **36**, 945 (1994).
5. R.D. Milroy & J.T. Slough, "*Poloidal flux loss and axial dynamics during the formation of a field-reversed configuration*", Phys. Fluids **30**, 3566 (1987).
6. I.R. Jones, & W.N. Hugrass, "*Steady-state solutions for the penetration of a rotating magnetic field into a plasma colum*n", J. Plasma Physics **26**, 441 (1981).
7. S.J. Tobin, et. al., "*RMF oscillator system for current drive in the TCS experiment*", Rev. Sci. Instrum. **72**, 3528 (2001).
8. A.L. Hoffman, "*Rotating magnetic field current drive of FRCs subject to equilibrium constraints*", Nuclear Fusion (2000).
9. R.D. Milroy, "*A magnetohydrodynamic model of rotating magnetic field current drive in a field-reversed configuration*", Phys. Plasmas (2000).
10. A.L. Hoffman, et. al., "*The TCS Rotating Magnetic Field FRC Current- Drive Experiment*", Fusion Science & Technology **41**, 92 (2002).
11. H.Y. Guo, et. al., "*Formation and steady-state maintenance of FRCs using RMF current drive*", Phys. Plasmas **9**, 185 (2002).
12. J.T. Slough & K.E. Miller, "*Flux generation and sustainment of a field-reversed configuration with rotating magnetic field current drive*", Phys. Plasmas **7**, 1945 (2000).
13. F.W. Grover, "Inductance Calculations Working Formulas and Tables", Dover Publications, New York, N.Y., (1962) p. 77.
14. G. Fiksel, et. al.., "*High current plasma electron emitter*", Plasma Sources Sci. Technol. **5**, 78 (1996).
15. S. Xu, et. al., "*Oscillating magnetic field current drive in a spherical plasma device*", Plasma Phys. Controlled Fusion **42**, 807 (2000).
16. A.L. Hoffman, J.T. Slough, "*FRC Lifetime Scaling Based on Measurements from the Large s Experiment (LSX)*", Nuclear Fusion **33**, 23 (1993).
17. S. Okada et. al., "*Confinement Properties of the FIX-FRC Plasma*", presented at US/Japan Workshop on Physics of Fusion Concepts Suited for D-^{3}He Burning, Monterey, CA (September 11-14, 1995).

18. R. Chodura, "*A hybrid fluid-particle model of ion heating in high Mach number shock waves*", Nuclear Fusion **15**, 55 (1975).

19. L.C. Johnson & E. Hinnov, J. Quant. Spectro. Radiat. Trans. **13**, 333 (1972).

20. G. S. Voronav, Atomic Data & Nuclear Tables **65**, (1997).

21. C.F. Barett, Oak Ridge national Laboratory: ORNL-6086 (1990).

22. H. Himura, S. Okada, S. Sugimoto, S. Goto, "*Rethermalization of an FRC in translation experiments*", Phys. Plasmas **2**, 191 (1995).

23. R.D. Milroy & J.U. Brackbill, "*Toroidal magnetic field generation during CT formation in an FRTP and a conical theta pinch*", Phys. Fluids **29**, 1184 (1986).

24. Yu.A. Omelchenko, "*Kinetic simulations of the formation and stability of the FRC*", Phys. Plasmas **7**, 1443 (2000).

25. M. Tuszewski & B.L. Wright, "*Observations of FRCs with spheromaks magnetic field profiles*", Phys. Rev. Lett. **63**, 2236 (1989).

26. L.C. Steinhauer & A. Ishida, "*Relaxation of a two-specie magnetofluid*", Phys. Rev. Lett. **79**, 3423 (1997).

APPENDIX A

A.1 Flux loops

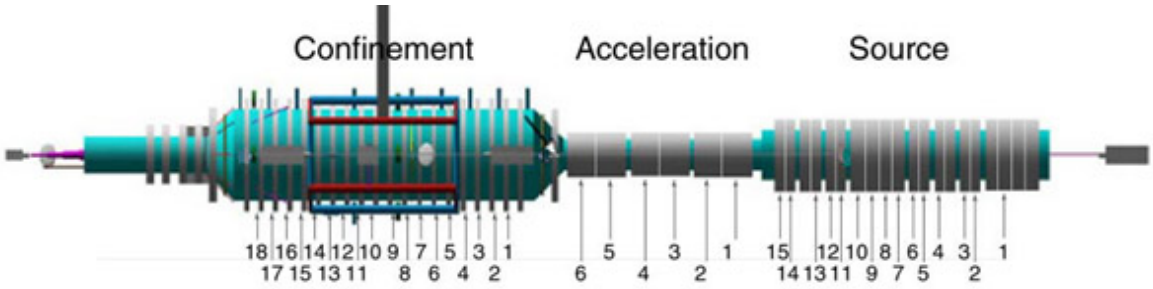

Figure A-1 Flux loop diagnostic

Diamagnetic loop arrays are the principal diagnostic for FRC experiments. The TCS experiment employs 39 diamagnetic loop arrays, 15 in the source, 6 in the accelerator, and 18 in the main TCS chamber, with locations indicated in Fig. A-1. Each array consist of a flux loop to measure the total flux inside the loop, ϕ_ℓ, and a hairpin loop covering approximately 360° to measure the external field B_e. These signals are combined in a bridge circuit, shown in Fig. A-2, to record the excluded flux

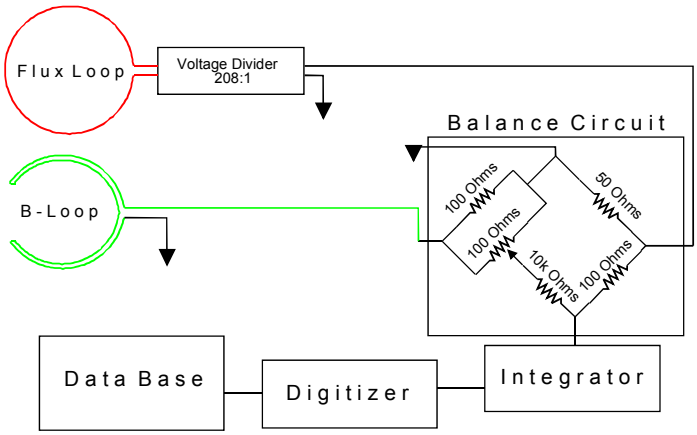

Figure A-2. Diamagnetic bridge arrangement used for

$$\Delta\phi = \pi r_\ell^2 B_e - \phi_\ell. \qquad [A.1]$$

at each location. B_e and ϕ_ℓ are individually recorded only at several locations, B_e at locations 2, 9, and 17, and ϕ_ℓ at locations 2, 5, 9, 15, and 17 in the TCS section. At locations where B_e and ϕ_ℓ are not individually recorded, ϕ_ℓ is assumed to be the same as at locations under the same coil set, and Eq. (A.1) is used to calculate B_e. The excluded flux is then used to calculate the excluded flux radius, defined as

$$r_{\Delta\phi} = \sqrt{\frac{\Delta\phi}{\pi B_e}} = r_\ell \sqrt{\frac{\Delta\phi}{\phi_\ell + \Delta\phi}} \qquad [A.2]$$

which gives the rough size and shape of the FRC. In addition, there are 4 flux loops in the plug region, and each cone has 4 sets of 1 flux loop, measuring the total flux inside the cone, and 2 B_e probes (with ~360º azimuthal extent) that measure the magnetic field parallel to and normal to the cone wall.

The $\Delta\phi(z)$ or $r_{\Delta\phi}(z)$ data is used to make time dependent plots of the axial extent of the FRC using the plot3D routine in MATLAB. The flux data has also been used to generate plots of field-lines outside the FRC separatrix (example in Fig. 4-53). This gives us an idea of where the open field-lines terminate and can be useful in tracking impurity production. These field-line plots are also being used to generate a grid on which the UEDGE and DIVIMP impurity codes can be run.

A.2 Interferometer

A two-color, double pass heterodyne quadrature interferometer was developed for use at 10^{19} – 10^{20} m^{-3} electron densities across 80-cm diameter plasma columns. The system uses CO_2 (10.6μ) and He-Ne (0.63μ) lasers with separate Bragg cell modulators to generate reference beams shifted by 40 MHz. The basic 10.6μ interferometer has a sensitivity to plasma electron density of $\int n_e d\ell = 2\text{x}10^{20}$ m^{-2} per fringe. The He-Ne laser can be used to compensate for vibration. The scene beam traverses a horizontal chord through the midplane of the TCS chamber through 1" ZnSe vacuum windows, is reflected by a hollow corner-cube reflector, and returns through the same windows, displaced axially by ~1.5 cm. A sketch of the system is shown in Fig. A-3. Not shown clearly in the figure is the 3D path the CO_2 reference beam traverses. The Bragg Cell splits the beam vertically, keeping the scene beam parallel to the surface of the optical table, while sending the reference beam diagonally upward. Both beams pass through the same ZnSe beam splitter (used to align the HeNE with the CO_2 beams, and send part of the CO_2 beam into the spectrometer) and use the same first two mirrors. After that, the scene beam is directed into the plasma, while the reference beam is reflected off three mirrors placed on vertical mirror posts ~30 cm above the optical table. The reference beam is then directed downward by the last mirror on the post, combined with the scene beam on the 2nd ZnSe beam splitter, and then focused on the detector.

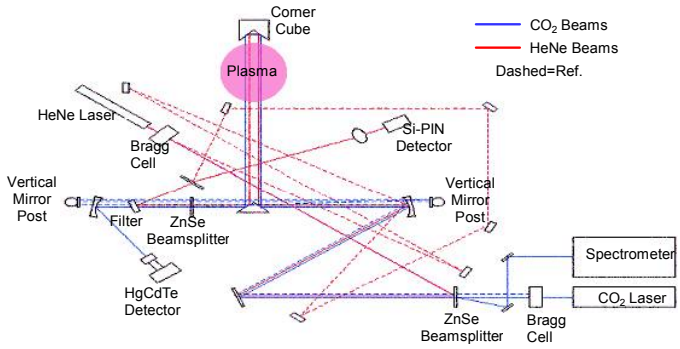

Figure A-3. Dual color, heterodyne quadrature interferometer geometry.

The interferometer and the return mirror for the scene beam are on separate optical tables, which rest on a wooden experimental deck surrounding TCS. Because these two tables aren't rigidly attached, relative motion of the two tables before, during, and after the shot causes large oscillations in the baseline signal. The HeNe interferometer was designed to compensate for vibration between the tables, but not for vibration effects on the interferometer table itself. It was found that at best it could track the phase of the CO_2 interferometer to within about 1/100th of a fringe, or an average density of about $1.3\text{x}10^{18}$ m^{-3} across a 1.5-m double pass length. For average densities of

around $1.3 \times 10^{19} m^{-3}$ this represents a 10% error. An alternate method, one of fitting a high (5^{th}-7^{th}) order polynomial to the signal before and after the shot, reduced this error by a factor of 2-3. An example of measurements for a plasma and a vacuum shot is shown in Fig. A-4. Both shots had the same RMF and coil magnets fired, with the only difference being whether puff gas was introduced. The polynomial corrected vacuum signal shows a low level noise associated with pickup of the RMF, but with that noise removed, the signal remain within $\pm 0.5 \times 10^{18} m^{-2}$ of zero. An upgrade to the system is being considered to stabilize the interferometer further by placing it on concrete pillars attached to the concrete floor, and strengthen some of the individual optical elements on the interferometer table.

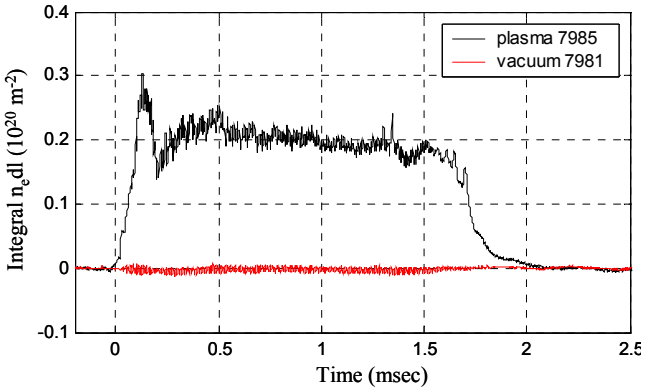

Figure A-4. Comparison of reduced interferometer data from plasma and vacuum

A.3 Tomography

A visible light tomography system was built to determine plasma shape and, to some extent, density profiles. Visible light emitted from the plasma is transmitted through the 40 cm radius quartz TCS vacuum chamber and is collected by a 7.62 cm diameter plastic ball lens. This ball lens is used as a common collection lens for a number (6-12 usually) of 3 mm plastic optical fibers, which are arranged in an arc around the ball lens. This configuration allows the use of large collection optics to increase light collection in a minimum of space, and collects emission from chords in a fan geometry covering impact parameters from -34cm to +34cm. Five of these ball lens 'fans' are arranged near the midplane of the TCS chamber in one axial plane as shown in Fig A-5, providing five separate views of the plasma, which is important in viewing high order instabilities, most notably the n=2 instability.

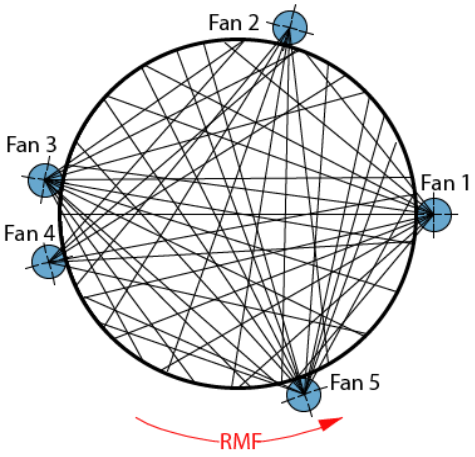

Figure A-5. Tomography fan arrangement at TCS midplane.

Light collected by the ball lens is filtered before entering the fiber optics by a combination of wratten filters that pass visible light in the relatively line free region between the D_α (656nm) and D_β (486nm) Balmer emission lines. The filters have a transmission of greater than 5% between 510nm and 580nm, with a peak of 33% at

535nm. This wavelength range was chosen to maximize the amount of Bremsstralung radiation collected, which is proportional to $\int n_e^2 d\ell$.

The fiber optics terminate in a shielded screen room, and are matched to an array of Si-photodiodes (Burr-Brown OPT210), which have an active area almost equal to the core area of the fiber optic. The photodiodes have an integrated FET-input transimpedance amplifier, and when matched with a 100 kΩ feedback resistor, have a bandwidth of 900 kHz, and a responsivity of 0.1 V/μW. The voltage output of the amplifier is then multiplexed in a ratio of 8:1, and the multiplexed signal is finally digitized at 10 MHz. Details of a single channel of the collection optics and detector electronics are shown in Fig. A-6.

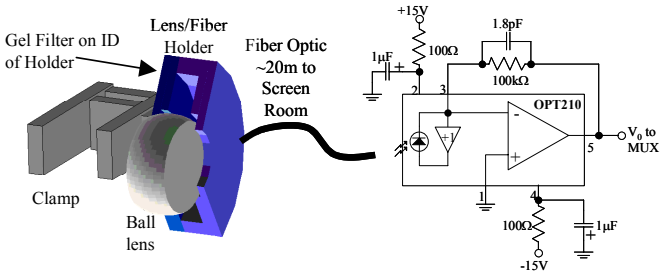

Figure A-6. Tomography collection optics and detector electronics

Chordal data from the tomography system is interpreted using an algorithm developed by Cormack[1,2], and later improved upon by Granetz[3,4]. The method is based on expanding the chordal measurements and the solution function in harmonic constituents, where the azimuthal component is expressed in sines and cosines, and the radial component is expanded in terms of Zernicke polynomials. The code used was developed by M. Anton for the TCV tokamak experiment in Lausanne, Switzerland, and modified for use with the setup on TCS.

The chordal data recorded ($f(p,\phi)$) can be represented as:

$$f(p,\phi) = \int_{L(p,\phi)} g(r,\theta) d\ell \qquad [A.3]$$

where $g(r,\theta)$ is the function that needs to be solved for. Using a horizontal diameter as a reference point, p is the distance of a perpendicular between the viewing chord and the center at r = 0 (impact parameter), and ϕ is the angle the perpendicular makes to the reference line. One can decompose both functions into their harmonic constituents:

$$g(r,\theta) = \sum_{m=0}^{\infty} \left[g_m^c(r) \cos m\theta + g_m^s(r) \sin m\theta \right] \qquad [A.4]$$

1 Cormack, A. M., *Journal of Applied Physics* Vol. 34, No. 9 (1963) 2722.

2 Cormack, A. M., *Journal of Applied Physics* Vol. 35 No. 10 (1964) 2908.

3 Granetz, R.S. and J.F. Camacho, *Nuclear Fusion*, Vol. 25, No.6 (1985) 727.

4 Granetz, R.S. and P. Smeulders, *Nuclear Fusion*, Vol. 28, No. 3 (1988) 457.

$$f(p,\phi) = \sum_{m=0}^{\infty} \left[f_m^c(p)\cos m\phi + f_m^s(p)\sin m\phi \right] . \qquad [A.5]$$

The expanded functions are substituted into Eq. (A.3) and, after some algebra, the following result can be shown, where *T(x)* is a Chebyshev Polynomial of the 1st kind:

$$f_m^{c,s}(p) = 2\int_p^1 \frac{g_m^{c,s}(r) T_m(p/r)\, r\, dr}{\sqrt{r^2 - p^2}} \; ; \quad T_m(x) = \cos(m\cos^{-1} x) \; . \qquad [A.6]$$

In order to be able to perform the computation in Eq. (A.6), Cormack chose to expand the radial solution function ($g_m(r)$) in terms of Zernicke Polynomials ($R_{ml}(r)$), which form a complete set of orthogonal functions:

$$g_m(r) = \sum_{l=0}^{\infty} a_{ml} R_{ml}(r) \quad ;$$
$$R_{ml}(r) = \sum_{s=0}^{l} \frac{(-1)^s (m+2l-s)!}{s!(m+l-s)!(l-s)!} r^{m+2l-2s} \quad . \qquad [A.7]$$

By substituting $g_m(r)$ into Eq. (A.6), one can represent the integral as:

$$f_m(p) = \sum_{l=0}^{\infty} a_{ml} \frac{2}{m+2l+1} \sin\left[(m+2l+1)\cos^{-1} p \right] \quad . \qquad [A.8]$$

Further substituting Eq. (A8) into Eq (A.5)

$$f(p,\phi) = \sum_{m=0}^{m_{\max}^c} \sum_{l=0}^{l_{\max}} a_{ml}^c \frac{2}{m+2l+1} \sin\left[(m+2l+1)\cos^{-1} p \right] \cos m\phi + \sum_{m=0}^{m_{\max}^s} \sum_{l=0}^{l_{\max}} a_{ml}^s \frac{2}{m+2l+1} \sin\left[(m+2l+1)\cos^{-1} p \right] \sin m\phi \quad . \qquad [A.9]$$

Since m_{max} and l_{max}, the radial and angular modes used for the expansion, are finite, Eq. (A.9) is a linear expansion of $f(p,\phi)$ into a finite number of terms. For M chordal measurements, there are M independent linear equations with the same set of coefficients. Calling $a_1 : a_{K/2} = a^c_{11} \ldots a^c_{mmax.lmax}$ and $a_{((K/2)+1)} : a_K = a^s_{11} \ldots a^s_{mmax.lmax}$ the equations can be written in matrix form as:

$$\begin{bmatrix} W_{11} & W_{12} & \cdots & W_{1K} \\ W_{21} & W_{22} & \cdots & W_{2K} \\ \vdots & \vdots & \ddots & \vdots \\ W_{M1} & W_{M2} & \cdots & W_{MK} \end{bmatrix} \begin{bmatrix} a_1 \\ a_2 \\ \vdots \\ a_K \end{bmatrix} = \begin{bmatrix} f_1 \\ f_2 \\ \vdots \\ f_M \end{bmatrix} \quad . \qquad [A.10]$$

The maximum number of expansion harmonics used, given by K = $(1 + m^c_{max} + m^s_{max})(l_{max} + 1)$, can not exceed the number of chordal measurements. Generally $m^c_{max} = m^s_{max}$. The matrix can be inverted, solving for the a_{ml}:

$$\mathbf{a} = \mathbf{W}^{-1}\mathbf{f} \quad . \qquad [A.11]$$

These coefficients are then plugged back into Eq. (A.7) and, carrying out the summations in Eq. (A.4), we arrive at the solution function, $g(r,\theta)$.

To test the validity of this method a phantom input shown in Fig. A-7, based on a rigid rotor density profile, was created. An optional modal variation (eg. n=2) was added and chordal measurements were numerically taken along the lines of site of the actual fan setup on the TCS chamber. These chordal measurements should mimic the measurements recorded by the tomography system. The inversion is then performed, and the results are compared with the original profile.

In Figure A-8, the left figure shows the test input, and the right figure is the output of the inversion. Shown are cases for 3 different modal variations, n=0,1,2 with reconstruction performed allowing for up to 5 radial modes, and 3 azimuthal modes (m_{max} = 4 and l_{max} = 2 so that K = 27) Also, the input profile used a rigid rotor profile with an RR K value of 1.3, and separatrix radius r_s = 40cm.

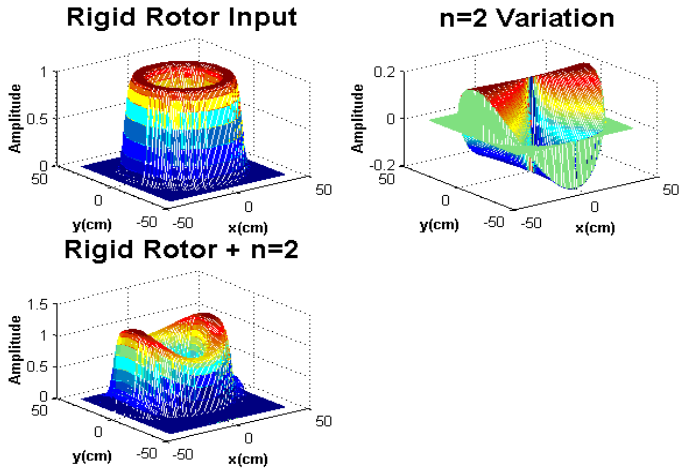

Figure A-7. Phantom input data to be chordally measured and inverted. The upper 2 figures are added together to create a rigid rotor profile with an n=2

Chordal measurements were taken assuming the 46-chord tomography setting that was used for much of the TCS program. The inverted output shows good agreement with the phantom input. Discrepancies are due to limiting the maximum number of modes allowed and the spatial resolution a 46-chord system provides. In determining the number of modes to use, the maximum number of expansion harmonics used, given by $k = \left(1 + m^{c}_{\max} + m^{s}_{\max}\right) \times \left(l_{\max} + 1\right)$, should not exceed the number of chordal measurements.

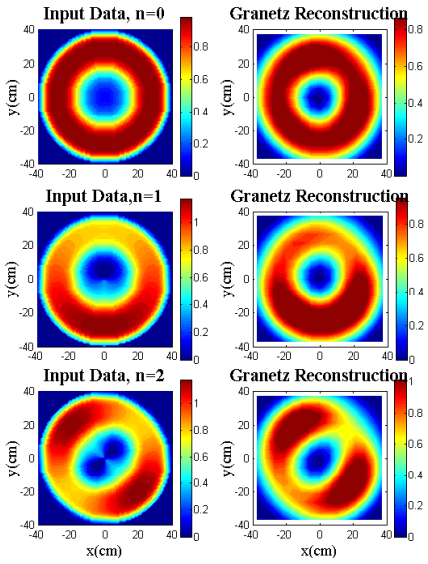

Figure A-8. Comparison of the phantom input profile with the profile after inversion

A.4 Neutral Density

A measurement of plasma neutral density is obtained from viewing absolutely calibrated emission from the D_α Balmer line, and converting the photon flux using the Johnson-Hinnov factor (L. Johnson and E. Hinnov, J. Quant. Spectrosc. Radiat. Transf.

13, 333 (1973)) into ionization rate. Neutrals present a large power loss channel through charge exchange and ionization losses.

TCS uses a lens/fiber system to couple the D_α emission from the plasma to the collection electronics. A number of lens holders are used to hold the fiber optics at a set distance from the lens. These lens holders are attached to a fan that is positioned on the TCS chamber, or alternatively the lens holders can be mounted directly on the TCS machine. Five lens holders are spaced axially along the TCS chamber, and eight are placed in a fan as sketched in Fig. A-9.

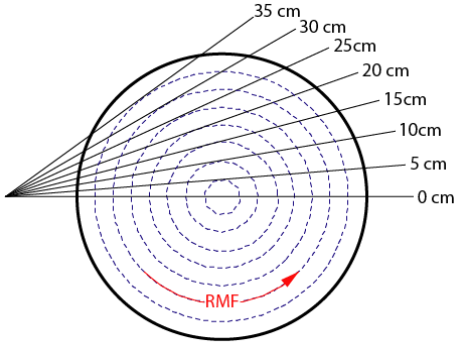

Figure A-9. Viewing chords for D_α

Light is transmitted via 600 μm diameter quartz fiber optics to the screen room, is passed through an interference filter with central frequency of 656nm and FWHM of 10nm and 60% peak transmission, and is detected by photodiodes that are packaged with an on-chip operational amplifier (EG&G HFD 1100). The output signals are amplified a factor of 10, AC-coupled to remove a ~200mV offset, multiplexed 8:1, and then digitized at 10MHz.

Absolute calibration of the system is provided by using a tungsten filament lamp powered with a current controlled power supply, and the use of an absolutely calibrated photodiode system purchased from International Light (SED 033). The calibration is accomplished by imaging the tungsten filament lamp on the calibrated photodiode, while making sure to overfill the photodiode, and then measuring the radiance. The measurement is then repeated by replacing the calibrated diode with the fiber optic, thus transferring the calibration of the diode to the fiber optic system.

A.5 Fast pressure Gauge

A fast response ion gauge was built to measure the neutral pressure in the confinement section. The ion gauge (Granville-Phillips model number 355001-YE) in use on TCS is of the Bayard-Alpert type otherwise known as an inverted triode gauge, as sketched in Fig. A-10. Like all other ionization gauges, it operates by ionizing a fraction of the gas molecules present in the gauge and collecting the resulting ions. These positively charged gas ions produce an electrical current flow on the ion collector. The magnitude of this current is directly proportional to the density of gas molecules. A higher density of gas molecules will cause a larger ionization rate, resulting in a greater ion current on the

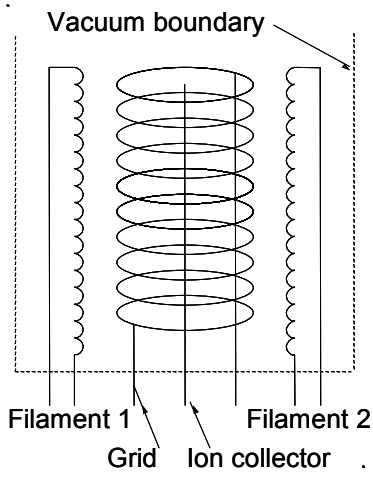

Figure A-10. Bayard-Alpert type ion gauge

collector. The voltage across a resistor in series with the collector is run through an isolation amplifier and then recorded by a digitizer.

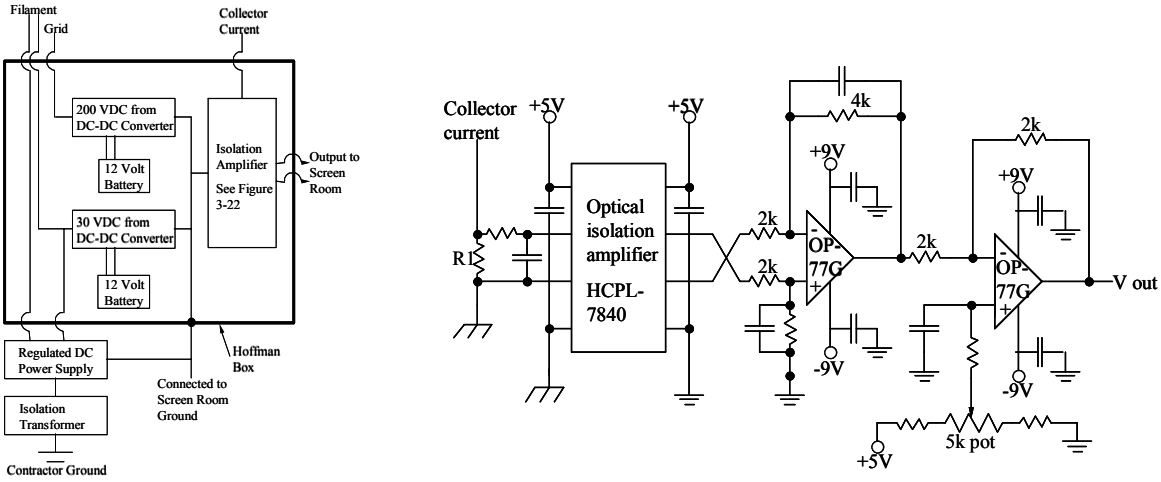

Figure A-11. Pressure gauge wiring diagram and circuit for fast pressure measurement.

The wiring diagram in Fig A-11 shows the power supply used to drive the filament and the DC-DC converters used to bias the filament and grid. A regulated DC power source is used to deliver the 2.7 amps necessary for thermionic emission of electrons from the filament. The regulated DC power supply is connected to an isolation transformer to prevent a ground loop. The filament is also biased to +30 volts with respect to the ion collector. A DC-DC converter is used to produce this bias voltage. The grid must be biased to +200 volts with respect to the ion collector. These bias voltages are necessary to impart enough energy to the electrons so they can ionize any neutrals present in the gauge tube. Separate 5.7 amp-hour 12-volt batteries power each DC-DC converter. Batteries were used to isolate each component and to reduce the noise on the collector.

The circuit used for the pressure measurements is also shown in Fig. A-11. This circuit features an optical isolation amplifier necessary to prevent a ground loop. The circuit has a net gain of 16, a rise time of approximately 5 μsec, and offset control using the 5 kΩ potentiometer. An R1 value of 125 kΩ allows for accurate pressure measurements from 10^{-8} to $5x10^{-3}$ Torr. This range can be shifted towards lower pressures by increasing the value of R1.

The connection between the gauge and the TCS chamber has a very small volume so that its pressure response could be as rapid as 230 μsec. It was hoped that the ion gauge would be

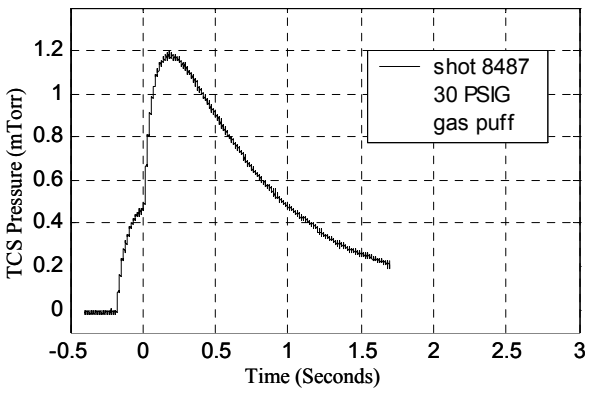

Figure A-12. Pressure measurement in TCS chamber for a double puff at 30 psig

capable of measuring the neutral pressure outside the separatrix during a pulse but the noise on the gauge from the RMF in particular has not allowed this to happen. Although inoperable during a pulse the ion gauge has been a valuable diagnostic used for puff fill valve calibration and post pulse pressure measurements. A typical response for a 30 psig puff is shown in Fig. A-12. The puff valve is opened at –200 milliseconds for 1millisecond and then opens again at –7.5 milliseconds for 3 milliseconds.

A.6 Langmuir Probe

A Langmuir double probe was inserted radially inward at the center of TCS. A picture of the probe tips is shown in Fig. A-13. The probe was connected by a bellows arrangement and could be placed at any radial location. It was originally hoped to operate the probe with a swept voltage so that temperatures could be recorded on a single shot. However, RMF associated noise made the results subject to large uncertainty and so most of the data was taken using various levels of fixed bias on sequential repeatable shots.

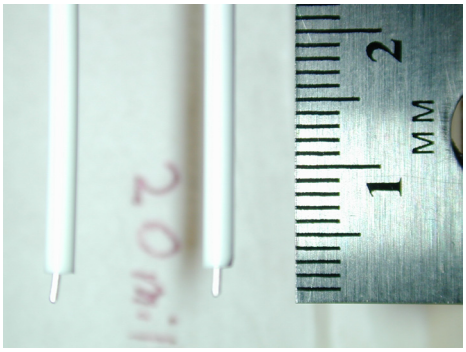

Figure A-13. Photo of Langmuir

Langmuir probes work by measuring macroscopic sheath characteristics. When a surface is exposed to plasma, a sheath region forms around it. The difference in thermal speeds between ions and electrons is the initial driver for a net electron current to the probe surface. If the object is electrically insulated, the surface typically charges negative until it has sufficient potential to balance the electron and ion currents. As the surface charges, it gradually builds up a region around it that has no electrons. This region, the sheath, plus a transition region, effectively shields the surrounding plasma from any large electrostatic effects. This region is very thin, on the order of micrometers. By inserting two conducting surfaces one can modulate the potential and record net currents across the sheaths. Using models of the sheath regions one can then take these macroscopic parameters and determine the electron temperature and density of the unperturbed plasma. A typical signal obtained with a similar (but asymmetric) probe is shown in Fig. A-14. This signal was obtained in a steady plasma from a Cascaded Arc Source (CAS) using a swept probe voltage (80 kHz, ±60 V max.). The CAS is being developed as both a preionizer (to eliminate the need to use LSX/mod) and as a plasma source during RMF sustainment.

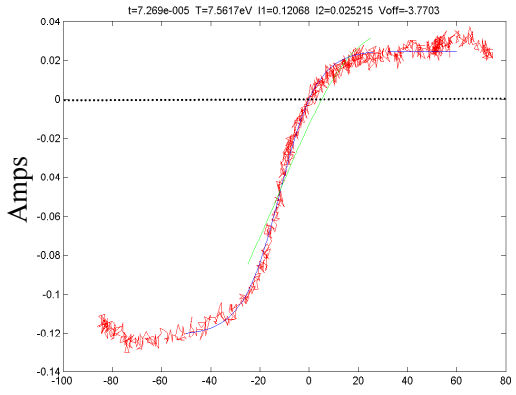

Figure A-14. Double Langmuir probe V-I trace obtained in Cascaded Arc Source.

The trace in Fig. A-14 shows two distinct regions, the two plateaus on the left and right are saturation regions. For a double Langmuir probe this means that one of the tips is in ion saturation. There is a limit to the current density (electron or ion) that can be drawn to a physical surface in plasma. As more ion current is removed from the probe tip the size of the sheath barely changes. The saturation current is purely a function of the ion density, electron temperature, and probe surface area. The region between the two saturation regions is a little more complicated. The electron temperature characterizes this region's shape. As the electron temperature increases, this region broadens (in voltage range). The probe tips are not in electron saturation and only a small portion of the electron thermal velocity distribution is ever sampled.

Even with only a d.c. bias the signals obtained from the double Langmuir probe were extremely noisy (about a 1:1 signal to noise ratio at peak signal) due to contamination from the RMF. Contamination was present even in vacuum shots with only a cable connected to the isolated bias and detection box. Contamination is not isolated to the pure RMF frequency but rather to multiples of that frequency. A picture of the detection box is shown in Fig. A-15a, with a circuit diagram shown in Fig. A-15b. The basic idea of operating in the high noise RMF environment was to limit the loop areas of the input stage and to set up the electronics in such a way that any contamination in later stages would be countered by active electronics. Unfortunately, the requirement for survivability to arcs

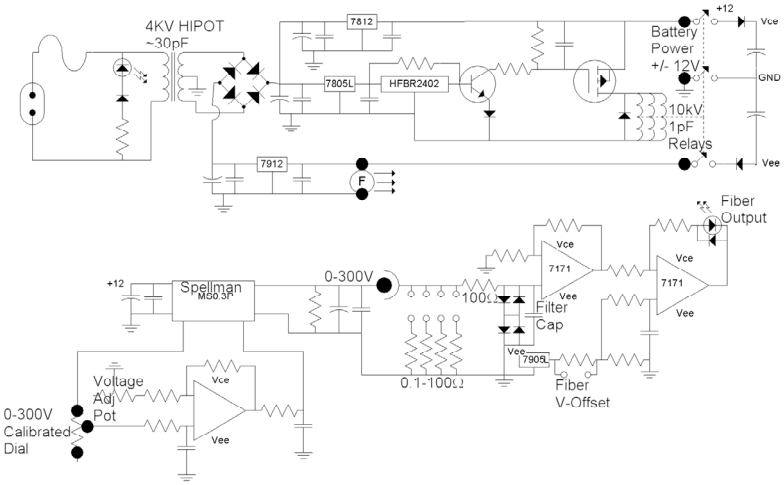

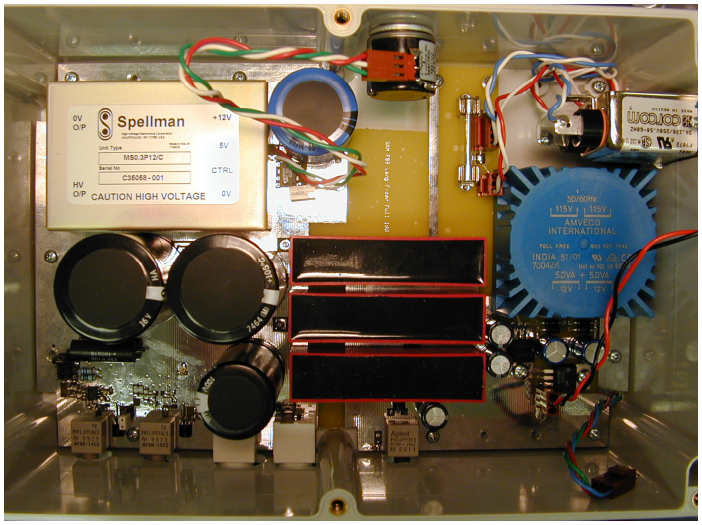

Figure A-15. Langmuir probe bias box picture and circuit

means that some of the components have to be large. The final output stage drives a fiber optic coupled diode that produces light as a function of current. This box can then be electro-statically isolated from system grounds and allowed to float at the probe tip potentials. The addition of an external metal box completes the shielding. It is only with

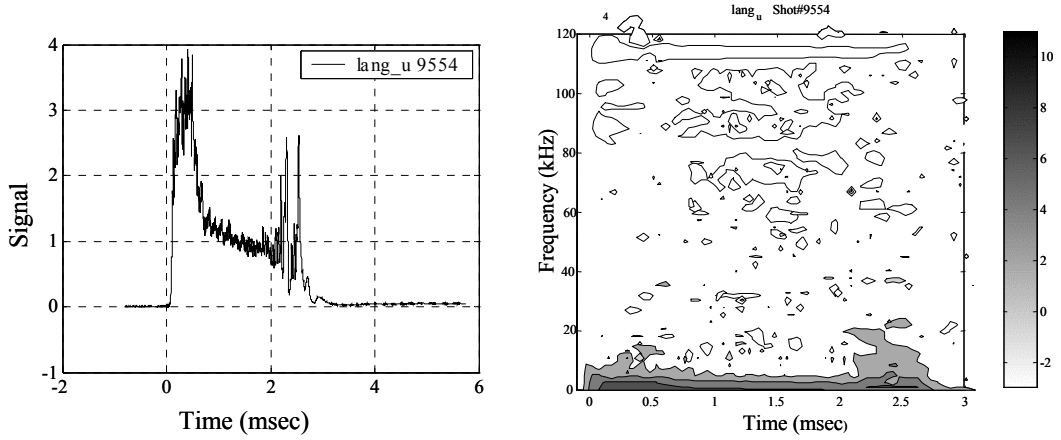

Figure A-16. Recorded Langmuir probe signal for shot #9554 with spectral

the addition of the external BNC cable that RMF noise becomes apparent.

A basic raw signal is shown in Fig A-16a, with a spectral resolution shown in Fig A-16b. This signal was obtained for a probe in ion saturation. The signal magnitude is proportional to $n_i\sqrt{T_e}$. For this figure an electronic filter limits the bandwidth to 100 KHz. The noise is spectrally localized at the RMF frequency and above. As such, a simple low pass filter removes its effects. Some of the real signal may also exist above the RMF frequency, but for purposes of extracting electron temperature this information is useless. Shot to shot conditions are not consistent enough to be able to reliably interpret any high frequency signals as fluctuations in temperature.

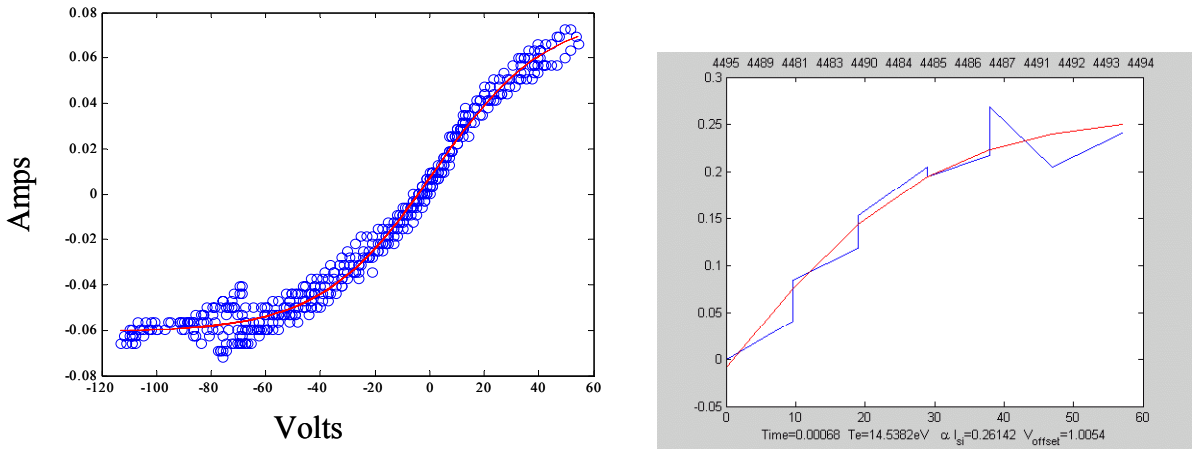

Figure A-17. Basic Langmir probe data for swept and dc biased probe.

A comparison of the data obtained with both a swept probe and the sequentially biased probe is shown in Fig. A-17 for an earlier box design. The basic equation relating

probe voltage, electron temperature, density, and current is $I=I_{si}tanh(V/2T_e)$. Where $I_{si} = 0.5n_eA\sqrt{(2T_e/m_i)}$. A is the surface area of the probe, n_e is the electron plasma density, and m_i the mass of an ion. From the first equation a curve fit can be done between the equation and the raw data to provide the electron temperature and ion saturation current. The red lines in the figures represent the ideal I-V curve derived from the fitted data. The second equation can then be used to find n_e.

A.7 Ion Doppler Rotation

Ion Doppler measurements can be used to measure both ion temperatures and velocities, and have been used on TCS primarily to obtain plasma rotation since the ion temperature has generally been too low to distinguish temperature broadening from the instrument width. The ion emission spectrum is measured using an Intensified Charge-Coupled Device (ICCD) camera (Princeton Instruments PI-MAX 512RB) attached to the exit plane of a 0.5-m f/6.5 Czerny-Turner spectrometer. For non-relativistic motion the measured wavelength shift is simply related to the velocity and viewing angle between the observer and the emitter:

$$\frac{\Delta\lambda}{\lambda_o} = \frac{v}{c}\cos\theta . \qquad [A.12]$$

Since this is an important and sophisticated measurement, the instrument and data reduction technique will be explained in some detail, which is summarized from Max Peter's thesis

A two-dimensional CCD chip provides both spectral and spatial resolution. The system can effectively resolve line radiation down to about a tenth of a pixel on the CCD. For a line at 500 nm this corresponds to 0.0025 nm, equivalent to the Doppler shift of a particle with 1.5-km/s velocity. The system has a reasonable efficiency over the range from 200 to 800 nm. The maximum gain is about 80 digital counts per photoelectron. A 25-μs exposure usually yields a good signal-to-noise ratio. Spatially, the system can collect light from six chords simultaneously.

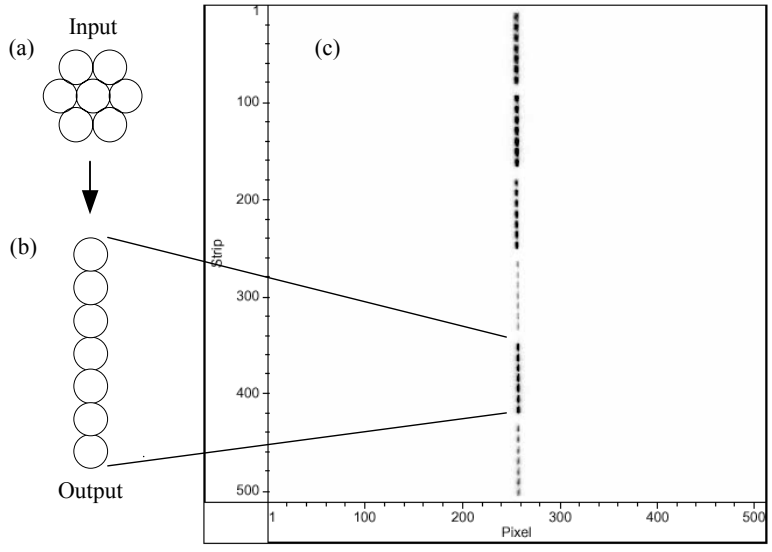

Figure A-18. ICCD Fiber Optic Bundles and Raw Image. (a) Fiber bundle geometry at the light input end. (b) Fiber bundle geometry at the light output end. (c) Raw ICCD image of the C-III line at 229.687 nm in inverted grayscale.

Electromagnetic radiation emitted from the plasma is collected and collimated by 12-mm diameter, 42-mm focal length quartz plano-convex lenses. A

fiber optic bundle is placed at the focal length of each lens. Each fiber bundle consists of seven individual 200-μm diameter UV fibers. At the input end of each fiber bundle, the seven fibers are in a hex-close-packed geometry, as shown in Fig. A-18, to maximize the collecting area. At the output end, the fibers are randomly ordered into a single vertical line. This geometry allows the narrowest entrance slit to the spectrometer possible. The CCD chip is large enough to image all six bundles simultaneously. An example of a raw image of the C III line at 229.687 nm is also shown in Fig. A-18. The horizontal dimension on the CCD is converted to a wavelength while the vertical axis is the imaging axis along the slit height.

The six fiber bundles typically view the plasma near the axial midplane. The fibers have been arranged in a variety of fans, as shown in Fig. A-19. For detailed velocity profiles, the fibers are positioned in a radial array, in 5-cm increments from y = 10 to y = 35 cm impact parameter.

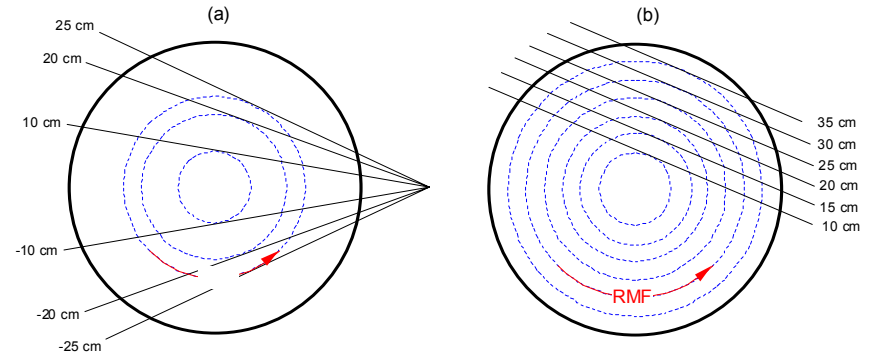

Figure A-19. ICCD Fiber Optic Array Layouts. (a) Symmetric fan used for line-of-sight velocity measurements. (b) Radial fan used

The spectrograph in the ICCD system is an Acton Research SpectraPro 500i Czerny-Turney type spectrograph. It has a focal length f of 500 mm and an aperture ratio of f/6.5. The spectrometer slit is typically 25-μm wide. Toroidal mirrors in the spectrometer provide the necessary horizontal (spectral) accuracy while maintaining sufficient vertical resolution to image six fibers simultaneously. The spectrometer has a stepper-motor controlled turret that holds three different 68 x 68 mm gratings. This allows both high spectral resolution and wide range because different gratings can be used for lines in different wavelength ranges. For Doppler effect studies, two high dispersion gratings are used, both with 1800 g/mm. One is a ruled grating with a blaze wavelength of 500 nm; the other is a holographic grating with a 250-nm blaze wavelength. Both gratings have a nominal dispersion of 0.9 nm/mm, equivalent to 0.022 nm per pixel and an 11.5-nm field of view.

A Princeton Instruments PI-MAX 512RB camera is located at the exit plane of the spectrometer. This camera contains a photocathode, microchannel plate (MCP), tapered fiber bundle, rear phosphor, and CCD chip. Incident photons are converted into electrons by an 18-mm diameter Gen-II photocathode with a relatively constant quantum efficiency of about 10% from ultraviolet wavelengths through the visible spectrum. The MCP is a slightly conducting glass plate with hundreds of thousands of 6-μm pores that can provide a maximum gain of about 560 electrons per incident photoelectron. The intensifier also acts as a very fast shutter. The intensifier is gated by switching the

accelerating voltage between the photocathode and the MCP, as well as by bracketing the voltage across the MCP. Bracketing gives the intensifier a nearly flat on/off ratio of about 10^7:1, even for high-energy incident photons in the UV that can pass through the photocathode and strike the MCP directly. Because of this high on/off ratio, no mechanical shutter is needed. The rear phosphor is type P43 (Gd_2O_2S:Tb) with a decay time (down to 1%) of 3 ms. Light from the rear phosphor is brought to the CCD chip via a 1.27:1 reducing fiber-optic bundle. The CCD is a Thomson 7895 square array with 512 x 512 imaging pixels. The CCD pixel size is 19 μm, but because of the tapered fiber optic coupling, the spectrograph sees an effective pixel size of 24.13 μm. The effective field of view focused onto the CCD chip is then 12.4 x 12.4 mm. The CCD well capacity is 450,000 electrons per pixel. A thermoelectric cooler keeps the CCD at a stable –20° C to reduce the CCD dark current to a nominal value of eight electrons per pixel per second.

The PI-MAX camera is controlled by a Princeton Instruments ST-133A controller. This unit contains an A/D converter for the CCD array output as well as a Programmable Timing Generator (PTG) that gates the intensifier. The PTG has a nominal insertion delay of 25 ns. The ST-133A also controls the intensifier gain and the grating stepper-motor. A 16-bit, 100-kHz digitizer converts the CCD well charge to digital counts, with one count equaling about seven electrons. The data is pre-processed by Roper Scientific Winspec software that arranges the CCD data back into its geometric order and applies basic grating equations to create a wavelength scale. Final processing is performed with MATLAB.

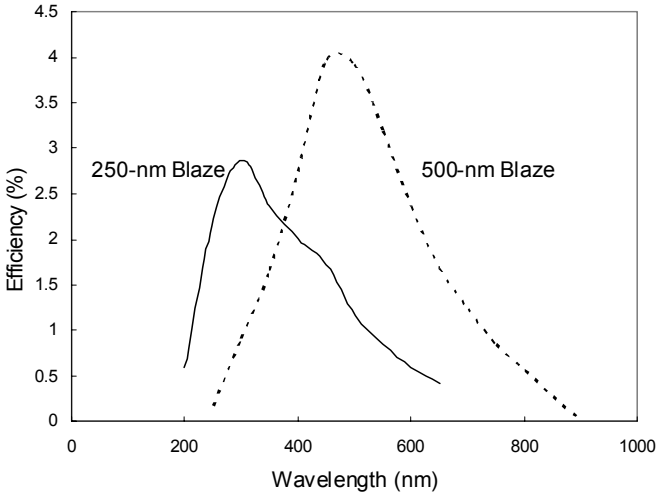

Figure A-20. ICCD Total System Sensitivity.

The ICCD system has not been absolutely calibrated. Based on the manufacturer specifications for the fiber optics, the gratings[i], and the photocathode[ii], the total system sensitivity versus wavelength can be estimated, as shown in Fig. A-20. By using different gratings, the spectrometer has a reasonable efficiency from 200 to 800 nm.

The first step in processing the raw ICCD image is to create a wavelength scale. The wavelength calibration is based on the Czerny-Turney grating equation:

$$\lambda = \frac{1}{kn}\left(\sin\alpha + \sin\beta\right) \qquad [A.13\}$$

where k is the diffraction order, n is the number of grooves per mm for the grating, α is the angle of the incident beam relative to the grating normal, and β is the angle of the exit beam, as shown in Fig. A-21. α and β are related to the inclusion angle γ, which is a

property of the grating, by $\gamma = \beta - \alpha$. The wavelength at the midplane of the CCD chip can then be written solely as a function of inclusion angle and the rotation angle of the grating ψ.

$$\lambda = \frac{2}{kn}\sin\psi\cos\left(\frac{\gamma}{2}\right). \qquad [A.14]$$

To find the wavelength at a location other than the CCD midplane, the focal length f, and the detector angle δ, must be taken into account. Both are determined through a calibration process that involves looking at spectral lines from a known source, such as a mercury lamp, at different locations on the CCD. The focal length is calculated to be within a few mm of the nominal value of 500 mm, while the detector angle has been aligned to within one degree of perpendicular. The equation for the wavelength at any point x on the CCD is then

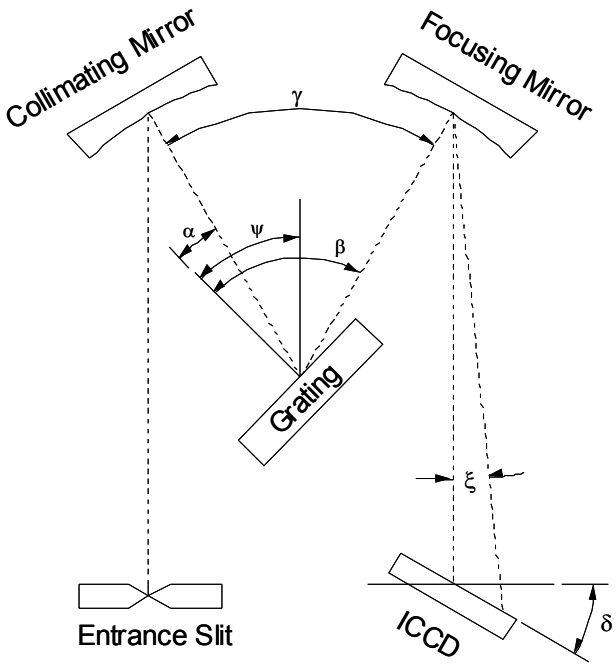

Figure A-21. Grating Geometry

$$\lambda(x) = \frac{1}{kn}\left\{\sin\left(\psi - \frac{\gamma}{2}\right) + \sin\left(\psi + \frac{\gamma}{2} + \xi(x)\right)\right\} \qquad [A.15]$$

where the angle ξ is related to f and δ by the formula

$$\tan\xi = \frac{x\cos\delta}{f + x\sin\delta}. \qquad [A.16]$$

The next step in calibrating the raw image is to correct for the instrument curvature induced by errors in the aspheric mirrors. Line radiation from a stationary calibration source should appear as a perfectly vertical line on the CCD. In reality, the line radiation is bent in varying amounts along the vertical imaging axis, forming a curved image. Since this error is of the same order as the Doppler shift being measured, it must be corrected for. The curvature correction factor is generated as follows. An image of a known calibration line is obtained from a calibration lamp. The peak wavelength of each row is found from a Gaussian fit. A second-order polynomial is then fit through the peaks. If there were no curvature effects in the optics, then this fit would be a perfectly straight vertical line. The curvature varies with wavelength so the process is repeated for different calibration lines. A typical curvature fit is shown in Fig. A-22.

Once the curvature has been removed from the image, the data for each fiber bundle can be averaged in a process called binning. The row numbers for each fiber bundle

image are identified as a region of interest, or ROI. Once the rows for each ROI are determined, the columns are "binned" or summed and averaged, producing a single spectrum for each ROI. There are typically six fiber bundles and thus six ROIs, so the binning process reduces a 512 x 512 image into six individual spectra, each with 512 points on the wavelength axis.

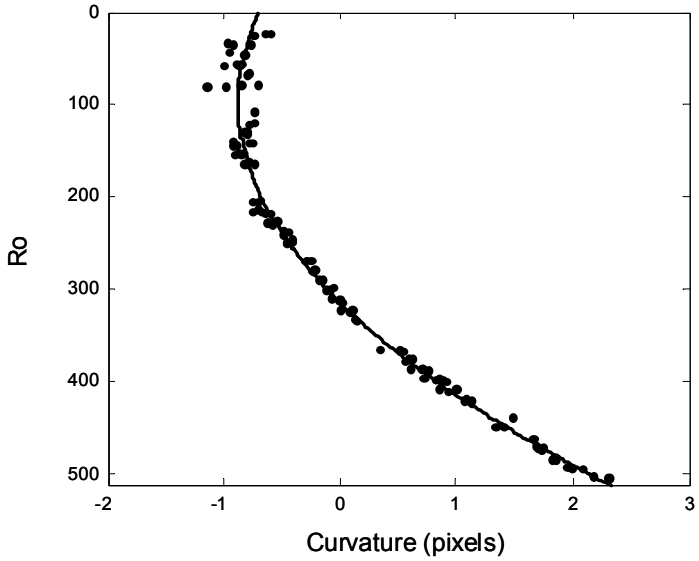

Figure A-22. ICCD Instrument Curvature. Fit shown is for the Hg I line at 404.656 nm viewed with an 1800-g/mm 250-nm blaze grating.

If the curvature correction is applied back to the calibration images, a nearly perfectly vertical image should be produced. A comparison of binned spectra produced with and without the curvature correction is shown in Figure A-23. In the data produced without curvature removal, the spectra are clearly shifted. The lower set of data, with the curvature calibration applied, are not only centered but also are narrower, because the curvature within each ROI has been removed before binning.

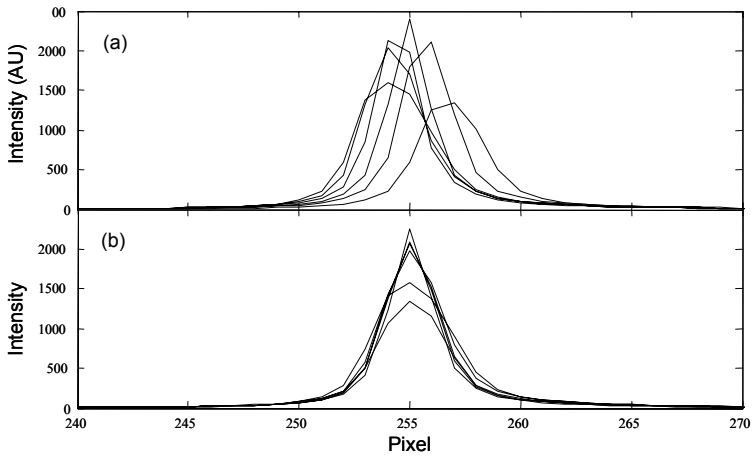

Figure A-23. Binned Calibration Spectra. (a) Hg I line at 404.656 nm binned without the curvature correction. (b) Same line but with the curvature removed before binning.

Even with the instrument curvature removed, line radiation is still broadened due to finite slit width and optical imperfections in the grating and mirrors. The output spectrum for a perfectly narrow delta function input is called the instrument function or point spread function (PSF). An input spectrum F is convolved with the instrument function G, resulting in the observed output spectrum H:

$$H(\lambda) = F(\lambda) * G(\lambda). \qquad [A.17]$$

The process of inferring the input spectrum F from the known instrument function G and the observed spectrum H is deconvolution. Several deconvolution techniques were attempted, and will be described briefly.

The simplest method attempted was analytic deconvolution. Assume that the instrument function G can be modeled by a simple analytic function such as a Gaussian, Lorentzian, or Voigt function. A Gaussian function is of the form

$$G(\lambda) = A_1 \exp\left(-z^2/2\right); \qquad z \equiv \frac{\lambda - A_2}{A_3}, \qquad \text{[A.18]}$$

where A_1 is the peak intensity, A_2 is the central wavelength, and A_3 is the standard deviation. A Lorentzian function is of the form

$$G(\lambda) = \frac{A_1}{\pi} \frac{A_3}{\left(\lambda - A_2\right)^2 + A_3^2}, \qquad \text{[A.19]}$$

where A_1 is the area under the spectrum, A_2 is the central wavelength, and A_3 is the half-width at half-maximum (HWHM). A Voigt function is a combination of the two. Similarly, if the input spectrum F is also assumed to be one of these analytic functions, then the deconvolution can be performed analytically[iii]. Unfortunately, the instrument function is not well-modeled by any of these analytic functions, as shown in Fig. A-24.

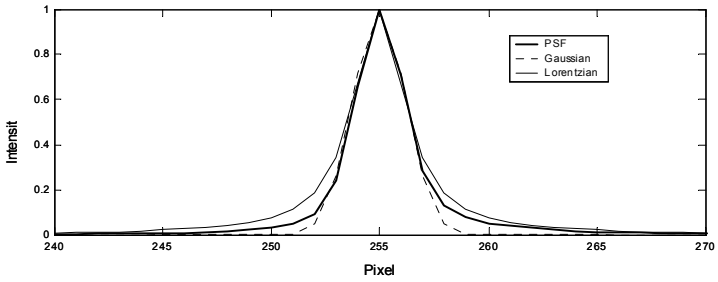

Figure A-24. ICCD Instrument Function. Instrument function for Hg I line at 405 nm compared with Gaussian

The second method attempted was Fourier deconvolution. Taking the Fourier transform Φ of Eq. (A.17) yields $F(\lambda) = F(F)F(G)$. The input spectrum is then found by rearranging and taking the inverse transform $F(F) = F^{-1}\{F(H)/F(G)\}$. This method is sensitive to noise in the spectrum. Even using a Weiner filter[iv] to minimize the effect of high-frequency noise, a satisfactory result could not be obtained with this method. A possible reason is the poor signal-to-noise ratio in the wings of the spectrum, particularly as the exposure time is shortened and single-photon statistics become important.

The final method attempted and finally adopted was to restrict the input spectrum to be a pure Gaussian, given by Eq. (A.18). Different input Gaussians are convolved with the known instrument function and compared with the observed output spectrum. The process is repeated until the coefficients A_1, A_2, and A_3 are found that result in the minimum least-squares error between the calculated output spectrum and the observed spectrum.

The ICCD system makes chord-integrated measurements of the emission spectrum. The line-of-sight spectra must be spatially inverted in order to obtain the local emission

and velocity profiles. The system has only six viewing chords, too few to make a good analytic or spline fit. Instead, the data can be spatially inverted using a matrix method.

Following the notation of Bell[v], assume that plasma is axisymmetric and is divided into j radial zones, as shown in Fig. A-25. Each zone is assumed to have a uniform emission ε_j and rotational frequency ω_j. The path length L_{ij} for sightline i with impact parameter y_i through shell j is given by:

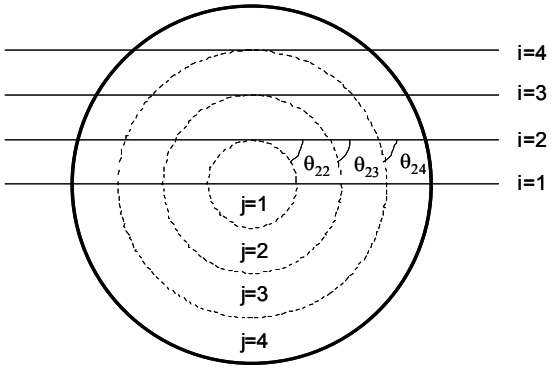

Figure A-25. Abel Inversion Geometry. Only four chords and shells are shown for clarity. The actual experiment has six chords and six shells.

for i < j: $Lij = 2\sqrt{y_{j+1}^2 - y_i^2} - 2\sqrt{y_j^2 - y_i^2}$

for i = j: $Lij = 2\sqrt{y_{j+1}^2 - y_i^2}$

for i > j: $Lij = 0$

The measured brightness B_i along sightline i is related to the emission profile ε_j by $B_i = \sum_j L_{ij}\varepsilon_j$. This can easily be inverted to obtain the emission ε_j from measured B_i: $\varepsilon_j = \sum_i L_{ij}^{-1} B_i$. Similarly, the local rotation frequency ω_j can be found from the apparent velocity u_i of the chord-integrated spectra. As shown in Fig. A-25, θ_{ij} is defined as the angle between chord i and the tangent of shell j. The apparent Doppler shift $v_j \cos\theta_{ij}$ is constant along sightline i through shell j as long as ω_j is uniform. The apparent velocity u_i, found from the Doppler shift of the centroid wavelength of the observed spectrum, is then $B_i u_i = \sum_j M_{ij}\varepsilon_j v_j$ where $M_{ij} \equiv L_{ij}\cos\theta_{ij}$. This can be inverted to obtain the local velocity v_j $\varepsilon_j v_j = \sum_i M_{ij}^{-1} B_i u_i$. The velocity inversion thus depends on the emission inversion; any errors in the emission inversion will propagate into the velocity inversion.

The simple matrix deconvolution scheme presented above is inconsistent with the Fourier deconvolution method. It assumes that the input spectrum for each chord is a pure Gaussian distribution. If the shells viewed by a chord are rotating at varying frequencies, then the actual input spectrum will be a sum of Gaussians, each with a different Doppler shift. The inversion scheme is modified slightly to take this into account, as follows. Instead of solving for all shells simultaneously, the shell properties are solved for individually starting with the outermost shell. The spectrum from shell j=n, where n is the total number of chords and shells, is assumed to be a pure Gaussian and can be Fourier deconvolved, yielding the emission and rotation frequency for this shell. The contribution of the spectrum observed by chord n-1 from shell n can then be estimated by convolving the Gaussian distribution for shell n with the instrument function for chord n-1: $H(\lambda) = F_{i=n-1}(\lambda) * G_{j=n}(\lambda)$. The calculated spectrum is subtracted from the

observed spectrum for chord n-1. The remaining spectrum must have come from shell n-1 and can be deconvolved to solve for ε_{n-1} and ω_{n-1}. This method is then repeated for each successive shell, like peeling the skin off an onion one layer at a time.

[i] Acton Research, "SpectraPro: Gratings", Data Sheet
[ii] C. Earle, "Spectral Improvements Extend Uses of Intensified CCDs", *Laser Focus World* **35** (1999)
[iii] I. H. Hutchinson, Principles of Plasma Diagnostics. Cambridge: Cambridge University Press, 1987.
[iv] W. H. Press, et al, Numerical Recipes in C. Cambridge: Cambridge University Press, 1988.
[v] R. E. Bell, "An Inversion Technique to Obtain Full Poloidal Velocity Profiles in a Tokamak Plasma", *Rev. Sci. Instrum.* **68**, 1273 (1997)

A.8 Power absorption

The antenna circuit can be represented as shown in Fig. A-26, where r_p represents the contribution from plasma loading. For $r_p >> \omega L >> r_L$, the antenna impedance can be written as $Z_L \approx i\omega L + \left(r_L + \frac{(\omega L)^2}{r_p} \right)$. Since the plasma power absorption is reflected in a complex manner, we will simply call this $Z_L \approx i\omega L + (r_L + R_p)$. in complex notation this is simply $Z_L = iZ_o e^{i\phi}$ where $Z_o = (\omega L)^2 + (r_L + R_p)^2$ and $\phi = tan^{-1}((r_L+R_p)/\omega L)$. For a sinusoidal voltage $V_a = V_o e^{i\omega t}$ the antenna current will be $I_a = V_a/Z_L = iI_o e^{i(\omega t-\phi)}$ with $I_o = V_o/Z_o$. The circuit power will then be $P = I_a V_a = 0.5 I_o V_o \{-sin(2\omega t-\phi) + sin\phi\}$, which averages out over a cycle to $0.5 I_o V_o sin\phi$. For small ϕ, $\phi \approx (r_L/\omega L) + (R/\omega L)$. Thus, if we subtract a phase delay between the voltage and the current equal to $r_L/\omega L$, we will only measure the power absorbed due to the plasma resistance. This is done experimentally by integrating $I_a V_a$ over a cycle, and adjusting the cable lengths to the digitizers so that a zero value results for vacuum shots. The currents and voltages are not exactly sinusoidal, so we cannot simply measure the phase difference between them, but the above method works fine for small deviations from sinusoidal inputs.

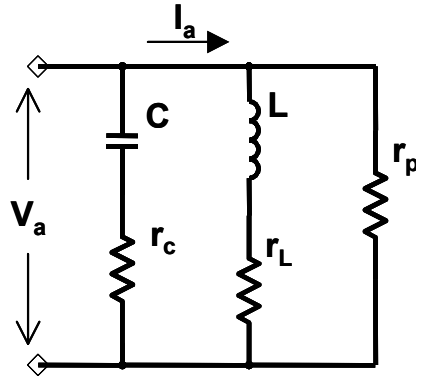

Figure A-26. Antenna tank

The antenna $I_o V_o$ is typically about 50 MW, while the absorbed power may be only 1 MW. Thus

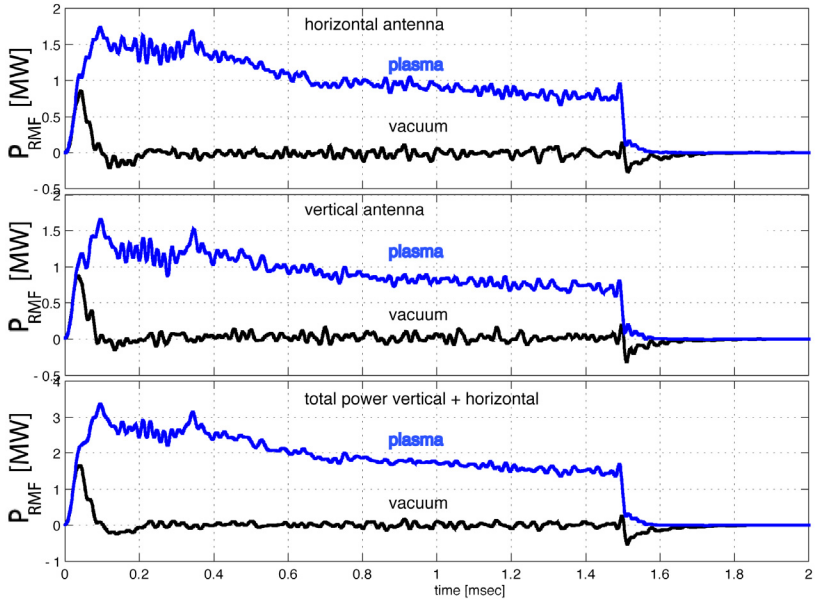

we must measure phase differences of order 0.02 radians, or only 1°. At a typical 150 kHz frequency this is only a time difference of ~20 nsec, and we would like accuracy to of order 1 nsec, or about 1 foot of cable. We have found that we can obtain sufficient accuracy using our standard 10 MHz digitizers (100 nsec between data acquisition) by fitting smooth curves to the antenna voltage and current, and integrating their product. This also required very accurate components for measuring the voltages and currents in the first place, which was accomplished by using an accurate current transformer for I_a, and a moderate resistor with several turns around a current transformer for V_a. Comparisons for the resultant signals with and without plasma are shown in Fig. A-27. The power at the beginning and ends of the vacuum shot are not zero due to the charging and discharging of the tank circuit. The method is thus seen to be very accurate, although the cable delay has to be set differently for each RMF frequency.

A.9 Bolometers

Our bolometers use X-UV silicon photodiodes from International Radiation Detectors Inc. that have highly stable internal quantum efficiencies and flat responses up to 6 keV photon energies. The measured quantum efficiencies are also close to that theoretically predicted by the 3.63 eV required to generate each electron-hole pair in silicon. This yields a high detector sensitivity (0.25 A/W). In addition, the diodes are small, can operate at room temperature, and are inherently fast. The testing and calibration of these bolometers is described in more detail in: *"Wideband silicon bolometers on the LSX field reversed experiment",* R. J. Maqueda, G. A. Wurden, and E. A. Crawford, Rev. Sci. Instrum. 63, p.4717, 1992.

Two bolometers are presently employed at the midplane of the TCS–RMF chamber (z = 4.25 m). They both view across a diameter (zero impact parameter) with one viewing from 4 o'clock (looking upstream) and the other from 8 o'clock. Fine electro-perforated screens (125 lines/inch) located near the diode surfaces can be used as attenuators (none is employed at present). The diodes are operated in current mode with 3.6 V reverse bias to help prevent saturation.

The geometry used in the first bolometer is sketched in Fig. A-28. The volume of plasma viewed is given by $V_a = \pi r_a^2 2r_s$. Actually the volume is somewhat cone shaped but a simple analysis shows this to be the correct volume to use with the given geometry, assuming all the volume is located at distance x. (See Goldenbaum & DeSilva's "Methods of Experimental Physics", chapter 3.) If the plasma is radiating at a rate $p_r(W/m^3)$, then the screen shielding the bolometer will see a value $P_s(W) = Kp_r(W/m^3)V_a$, where $K = \pi r_p^2/4\pi x^2$ is the fraction of the solid angle subtended

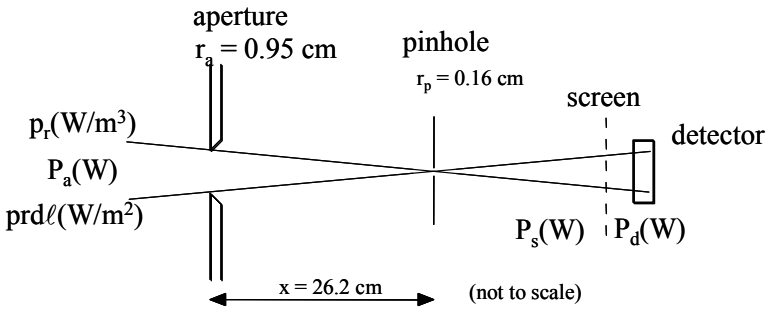

Figure A-28. Housing geometry for bolometer one.

by the pinhole (just like using a lens f number). Therefore, the geometrical relationship between p_r and P_s is

$$p_r(W/m^3) = \frac{1}{2\pi r_s}\left(\frac{2x}{r_a r_p}\right)^2 P_s(W) \ . \qquad [A.20]$$

The bolometer signal is recorded as "bolom" in our database. The screen transmission and the photodiode calibration give us the power P_s but, since we don't immediately know the FRC separatrix radius r_s, the signal "prdl"$(W/m^2) = 2r_s p_r(W/m^2)$ is recorded. p_r is recorded as "bolom_cal" by dividing "prdl" by $2r_s$. The total radiated power $P_{rad}(W)$ is then given by multiplying p_r by the FRC volume $\pi r_s^2 \ell_s$ and recorded as "bolom_mw". It is also seen that $P_{rad} = 0.5 r_s \ell_s$"prdl".

Without the screen $P_d = P_s$ and, with a 2500 Ω resistor in the detector circuit, $P_d(mW) = 1.6$ bolom(V). For bolometer #1 x = 0.262 m, r_a = 0.0095 m, and r_a 0.0016 m. Thus prdl$(W/m^2) = 3.78\text{x}10^8$ $P_d(W) = 0.605\text{x}10^6$ "bolom"(V). The various factors, sen = 0.25, R =2500, x = 0.262, ra = 0.095, rp = 0.0016, scr = 1.0 can be entered in the MDS data base using the IDL program bolom_trans.pro. Sample traces from the two bolometers are shown in Fig. A-29. The oscillations beginning at about 0.5 msec are due to an n = 2 instability, whose direction of rotation (clockwise when viewing upstream) can be determined by the relative phases.

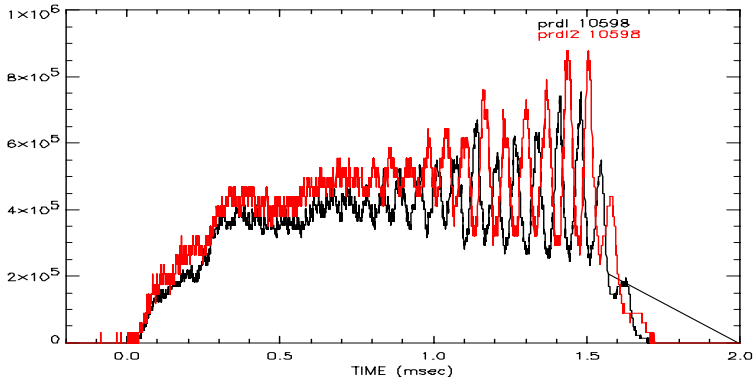

Figure A-29. Sample bolometer traces showing an n=2

A.10 Internal probes

Internal probes were an extremely important diagnostic in understanding the RMF current drive process, and we have conducted an ongoing development program to extending their usefulness to ever more energetic plasmas. On TCS a 42-cm long probe, containing 31 B-dot loops, could be extended radially inward at the midplane. A bellows arrangement was used so that the probe could be withdrawn entirely, or extended 12 cm past the tube axis. The first 11 loops (generally r = 0 to r = 20 cm) were spaced 2-cm apart, with the remaining 20 loops (generally r = 21 to r = 40 cm) were spaced 1-cm apart. All loops are in the same plane. A sketch of the probe is shown in Fig. A-30, where an expanded view of one loop is shown. Each loop is 9-mm long and consists of 30 turns of 37 μm diameter gold plated tungsten wire. The tungsten wire has a 30 times greater tensile strength than copper wire, which was too fragile to allow winding without

breakage. The gold plating allowed soldering to the wire, which enormously simplified connections. Polyimid insulation was used so the insulation could be soldered through.

The 1-mm square winding form was inserted into a 3-mm OD BeO tube. This was difficult since any friction caused the wire to short through the insulation. To solve this problem the wires and form were wrapped in Teflon plumbing tape. Ultra small and thin heat shrink would also work, and will be used for future probes. The inside of the beryllia tube was gold plated to act as an electrostatic shield, which was necessary to avoid noise pickup. This probe worked well for RMF formed FRCs, but was cracked by translated FRCs. Interlocking ~5-cm long, 6-mm OD pieces of boron nitride (BN) tube were then placed over the BeO tube. Although its surface was blackened, this material stood up to the thermal stresses induced by the high energy FRCs without cracking, probably due to a better ductility.

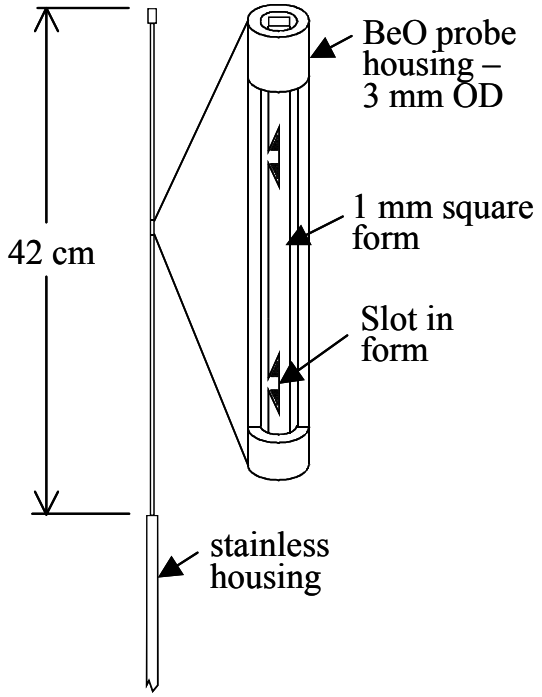

Figure A-30. Internal probe design.

The most important considerations for an internal probe are its ability to survive inside the plasma, and its influence on the plasma. There are three important relationships to consider. Assuming sonic flow for deuterium, the incident power is

$$P_{inc} = 3.6\times10^{-15} n T_e^{3/2}(eV)\ W/m^2 \qquad [A.21]$$

If the probe material has a melting temperature of T_{melt}, a thermal conductivity of K, a density of ρ, and a specific heat of c_p, and can be considered semi-infinite for the timescale involved, the time it takes for the surface to reach melting temperature is

$$\tau_{melt} = 0.25\pi T_{melt}^2 K\rho c_p / P_{inc}^2 \ \text{sec} . \qquad [A.22]$$

If the probe has a surface area of A_p and a mass of m_p, and is exposed to the plasma for t_{exp}, its overall temperature change after equilibration will be

$$\Delta T = P_{inc} t_{exp} A/m_p c_p \ °K \qquad [A.23]$$

This is not a problem for our short duration plasmas.

Equation (A.21) provides a measure of the power the plasma will lose to the probe. Minimizing the probe area will minimize the probes impact on the plasma. The probe should be made sufficiently small so that the power lost to the probe is small compared to the plasma's characteristic energy loss rate. Equation (A.22) determines whether the probe surface will melt. Most likely, once the probe's surface melts (or boils), either the probe or the plasma will be destroyed. The probe material which will survive the longest has the largest material figure of merit, $T_{melt}^2 K\rho c_p$. Various materials and their

corresponding figures of merit are shown in Table A.1. The material figure of merit expresses the ability of the material to both hold heat without damage, and to rapidly transport heat away from the surface.

Table A.1
A Comparison of Material Properties

	T_{melt} (°K)	ρ (10^3 kg/m^3)	K (W/m°K)	c (J/kg°K)	$T_{melt}^2 K\rho c$ (10^{15})
Tungsten	3700	19.0	180	130	6.09
Molybdenum	2900	14.0	150	250	4.42
Aluminum	1000	2.8	240	900	0.60
Inconel	1700	8.2	30	200	0.14
Berylium Oxide, BeO	2800	3.0	260	1000	6.12
Boron Nitride, BN	3300	2.2	180	710	3.06
Aluminum Oxide, Al_2O_3	2300	2.6	26	800	0.29
Quartz, SiO_2	1900	2.6	2	740	0.01

The initial 3 mm diameter by 42 cm long beryllia jacketed probe used in the RMF formed and sustained TCS plasmas had no noticeable impact on any of the measured plasma parameters, a result consistent with Eqs. (A.21) and (A.22). Typical plasmas had temperatures of $T_e \sim T_i \sim 25$ eV, densities of 2×10^{19} m^{-3}, and durations of 2 msec. Under these conditions, Eq. (A.21) predicts a power loss to the probe of about 70 kW, a number small compared to the plasma's few megawatt energy loss rate. Equations (A.22) and (A.23) predict a surface melting time of many seconds and a total temperature change of 20 degrees, both far from any region of potential harm.

As mentioned earlier, the BeO probe jacket material cracked both crosswise and lengthwise along the sides facing the incoming FRC for high energy translated FRCs. Thermal stress and possible stress from the surface melting and then shrinking as it rehardened are suspected. It is worth noting that the only material to fail in the TRAP plasmas was a small diamond window, and that it failed in a similar manner to the beryllia, by cracking. Diamond has a figure of merit 10 times greater then that of beryllia, largely due to a high thermal conductivity. In both of these materials, it is believed that failure was caused by the stress induced from the plasma heat load penetrating a significant distance into the material. In the TRAP experiment, the beryllia did not fail, but the plasma was only on the probe for 10 μsec, compared to the 250 μsec in TCS. Thus material ductility is another consideration in probe construction.

For the translated FRCs a comparison between the observed and predicted probe behavior is difficult to make since the relevant plasma parameters are both poorly known, and widely variable during the translation process. The conversion of internal energy to directed translational energy, and then back into internal energy further complicated the picture. The plasmas started in the formation section with densities of 6×10^{20} m^{-3} and temperatures of $T_e \sim T_i \sim 200$ eV for the low formation energy plasmas, and $T_e \sim T_i \sim 450$ eV for the high formation energy plasmas. In this range, the probe surface would have started to melt in 70 μsec for the low formation energy plasmas, and 7 μsec for the high formation energy plasmas. Corresponding energy deposition rates would have been 6

and 21 GW-m^{-2}. These numbers are consistent with the observed significantly greater impact of the probe on the high formation energy plasmas then on the low formation energy plasmas.

After capture, the plasmas had densities of 5×10^{19} m^{-3} and temperatures of $T_e \sim T_i \sim$ 100 eV, both well within the safety limits of the probe for the duration of the FRC. The very high directed energy of the plasma on first pass, a few times the plasma's internal energy, was particular hard on the probe. Only the side of the probe facing the incoming plasma was blackened. It is suspected that the initial interaction between the probe and the translating plasmas was largely responsible for any subsequent degradation in performance. Possibly as the plasma was translated supersonically over the probe, it swept/sputtered/ablated material from the probe surface into the bulk of the plasma.

Certainly, Eqs. (A.21), (A.22), and (A.23) do not contain all the relevant physics that one must consider when building an internal probe, or selecting a suitable probe material, but they do provide a good starting point. Another relevant consideration has to do with the impact impurities released from the probe will have on the plasma. Depending on the plasma conditions, low Z impurities (B,N) might be much less harmful then higher Z impurities (O,Si,Al), but very high Z impurities (W,Mo), given their mass, may not have time to migrate very far from the probe, and thus may not be too harmful.

Taking Eqs. (A.21) and (A.22) at face value, an internal probe made with a boron nitride jacket should be useful up to temperatures of $T_e \sim T_i \sim 260$ eV and densities of 1×10^{20} m^{-3} for the duration of a millisecond. Rather then the probe surface melting, a greater limiting factor could well be the energy drain from the plasma to the probe. For these plasma conditions with the existing internal probe, the drain would be about 10 MW, a value far too large given the energy input rate of a few megawatts. Since this number is directly tied to the surface area of the probe, it would be essential to limit the size of any internal probe. It is worth noting that for large incident powers, on the order of tens of gigawatts per square meter, the measured incident power to the probe has consistently fallen below that predicted by Eq. (A.21). If this held true at lower incident powers, then an internal probe might have a useful range substantially greater then that predicted by the equations.

Since the B-dot loop areas are very small, the magnetic fields relatively low, and the RMF environment very harsh, a large development effort was required to measure the small signals. The end result was a separately shielded box inside the screen room that contained high speed and high gain gated differential integrators. These integrators had a time constant of 20 μsec and could accurately integrate a sub microsecond square wave ranging in amplitude from the millivolt to volt range. On the long time scale, the integrators had a pot to zero their drift. Typical signals were recorded for 0.25 seconds with a 100 nsec sampling rate during the time of interest, and a much slower sampling for the rest of the time. The long sample time allowed the slow bias field waveforms to be recorded, as well as the slope of the integrators drift. The gain of the integrators was pushing stability and noise pickup limits, and it would be difficult to design integrators with a significantly higher gain. In particular, the integrator drift was starting to become

non-linear at about the digital count level. In order to remove this drift from the real signal, its waveform must be known. The desire for high gain integrators arises from the need to make the probe, and hence the windings, as small as possible.

All of the loops in the probe were oriented in approximately the same direction. This was done to maximize the radial resolution, but it came at the cost of no ability to properly separate the axial and azimuthal magnetic fields. Instead the field components were separated using the knowledge that the majority of the azimuthal field, the RMF, occurred in a narrow well defined frequency range that could be isolated using an FFT. This technique was not without its own problems and limitations, and it is described below. Subsequent probes will likely be built with double or triple probe windings, at the cost of some radial resolution. However, since our ability to make ever smaller probes has improved, the drop in radial resolution will not be as great as it would have been when this probe was built.

The probe calibration procedure began by producing a uniform known magnetic field in a strip line calibration unit. The copper used in the strip line was sufficiently thick that it maintained a constant flux for the duration of the current pulse, and the appropriate formula relating the field to the current was used. The current was measured with three different Pearson probes to eliminate potential errors in any one probe, or its termination resistor. With a knowledge of the applied magnetic field, the entire probe system, including all electronics as standardly connected to the digitizers, was calibrated simultaneously. Calibration shots were taken at 10 degree increments as the probe was rotated through 180 degrees. Three shots were taken at each angle, with the probe's angle reset between each shot. A sinusoid was then fit to the data collected for each channel to determine it magnitude of response (sinusoids peak), and relative angle (sinusoids zero crossing). The probe was then inserted into the machine where another angular scan was done to determine the absolute angle of the entire probe with respect to the applied axial field. After this, a final adjustment of a few percent was made to the amplitude calibration numbers based on a knowledge of the actual vacuum axial field profile, i.e. that it had to vary smoothly with radius. The profile was found by fitting a curve with the expected radial dependence to the data. Each data point was then adjusted to lie on the curve, based on a many shot average to help reduce digital count errors.

The entire probe is calibrated to within a few percent. The largest systematic error likely arises from relating B to I in the strip line calibration unit since the formula used was only good to first order, a few percent. The largest random error is a few Gauss, and is due to digital counts on 8 bit digitizers. Noise pickup of RMF 'parallel' to the probe, i.e. the vertical phase of the RMF to which the probe should have no sensitivity, is at the digital count level. The probe's frequency response rate is limited to the 10 Mbit digitizer sample rate. The excluded flux diagnostic, calibrated to within a few percent, provided a nice confirmation of the internal probe's calibration. The vacuum axial field profile measured by the probe was integrated to obtain the total flux through the magnets. This number was within a few percent of the flux measured by the excluded flux diagnostic. Figure (A-31) shows the radial profile of the vacuum axial magnetic field, and the radial profile of the RMF. The RMF falls off so dramatically near the plasma

tube wall because the internal probe passes vertically through the center of the antenna, at the point farthest from any conductor.

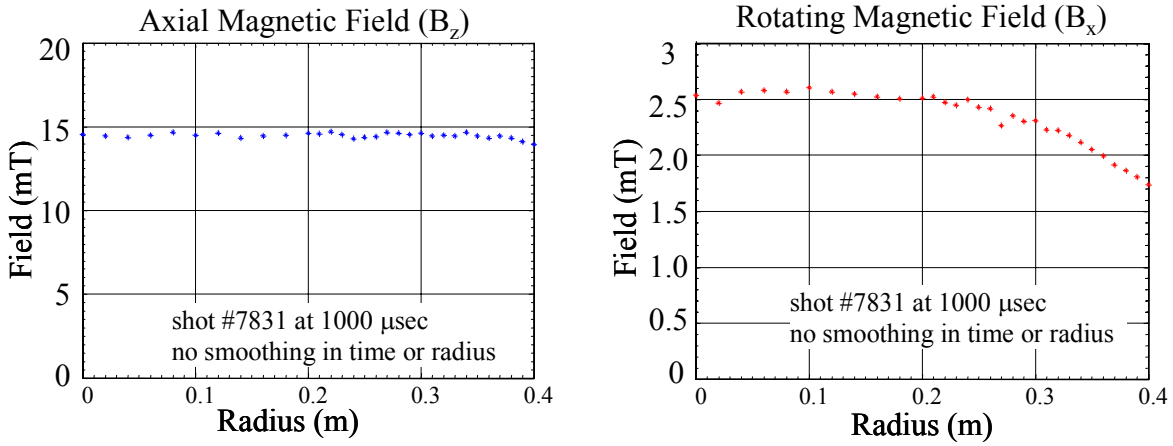

Figure A-31. Radial profiles of the vacuum axial and RMF fields

Regarding location, on any given shot, the angular position of the probe is known to within about two degrees. The location of any loop to any other loop is known to within about a quarter millimeter. The entire probe assembly can be moved radially in and out of the vacuum chamber. The location of each loop with respect to the plane normal to the probe that contains the line that defines the axis of symmetry of the machine is known to within one millimeter. However, the entire probe can be deflected slightly side to side, and this means that the distance of each probe to the actual axis of symmetry is only known to within about a centimeter. The actual axis of symmetry is itself somewhat ill defined since the axis of symmetry of the quartz vacuum vessel is about half a centimeter higher then the axis of symmetry of the axial field magnets, and presumably, the RMF antenna. It is worth mentioning that what really matters is a knowledge of the location of each loop with respect to the axis of symmetry of the FRC. Based on observations of the FRC's motion, and a corresponding lack in knowledge of its exact location, the above errors in probe location are inconsequential. In processing the probe data, it is typically assumed that the RMF formed FRC is both centered and that it has cylindrical symmetry.

On a typical shot, the calibration of the probe data begins by removing the integrator drift with a slanted base line correction, using the data acquired long before and after the shot. Once this is done, the period of slow sampling before and after the time of interest is removed since it complicates further data analysis. Next, the axial magnetic field, B_z, is separated from the RMF, B_x. B_x is used instead of B_{RMF}, or B_θ, since the probe only measures the horizontal component, and it is only with the assumption of cylindrical symmetry that B_x can be considered B_{RMF} or B_θ. The internal probe usually sits at a 45 degree angle to both B_z and B_x. The components are separated using an FFT. Typically, all frequencies within 10 kHz of the RMF frequency are ***defined*** to be B_x, and all other components are ***defined*** to be B_z. This is generally useful and accurately reflects the component data, though there are certainly exceptions.

Features missed would include such things as rotating RMF structures, as seen in some simulations, as well as steady toroidal fields. If, due to drag, the penetrated RMF starts to twist up and slow down, once its frequency drops outside of the filter band it is no longer attributed to B_x, but rather B_z. Similarly, slow toroidal fields would be attributed to B_z, and not B_x. The reverse problem happens with the translated plasmas, where as the plasma rapidly passes the probe, dynamics in B_z occur at frequencies similar to the RMF, and are thus attributed to B_x by the filtering. Fortunately, since the probe can be rotated, it is possible to measure only B_z or B_x to see what is actually happening. However, then one must rely on shot to shot reproducibility to compare the two field components, since when one is measured, the other is not. It is through independent measurements of B_z and B_x in this manner, and their comparison with the simultaneous measurement of B_z and B_x that the general validity and usefulness of the FFT separation technique was established, even though there are cases when it fails.

Once the two field components were separated, the amplitude and angular calibration numbers were applied, and the data was written back to the data base. The data was stored as Bz01 to Bz31, Bx01 to Bx31, and Bxe01 to Bxe31. The Bxe signals were simply the envelope of B_x, and are particularly useful when comparing the RMF amplitude between shots, and as a function of radius.

A.11 Spectroscopy

Three monochrometers were employed to look at line radiation from C-III at 2290 A° (Acton), O-III at 3265A° (VUV), and Si-III at 4553 A° (JASH). All monochrometers viewed the plasma column horizontally across a diameter near the center of TCS. A direct lens system was used for the Acton and VUV monochrometers, while fiber optic coupling was used for the JASH monochrometer. Quartz fibers are being purchased so that all monochrometers can employ fiber optic coupling, of the same design as used for the Doppler broadening methods.

The line radiation was not absolutely calibrated, but could be used to estimate which impurities were most important for which operating conditions, and at what time the impurities began to appear. Useful comparisons could be made to the total radiated power measured by the bolometers.